HIGH-BANDWIDTH HIGH-PRECISION ROBUST X-RAY MICROSCOPY - A CONTROL SYSTEMS APPROACH

BY

SHEIKH TAMJID MASHRAFI

DISSERTATION

Submitted in partial fulfillment of the requirements
for the degree of Doctor of Philosophy in Mechanical Engineering
in the Graduate College of the
University of Illinois at Urbana-Champaign, 2019

Urbana, Illinois

Doctoral Committee:

Professor Srinivasa M Salapaka, Chair & Director of Research
Dr Curt Preissner, Argonne National Laboratory, Director of Research
Professor Naira Hovakimyan
Professor Petros Voulgaris
Adjunct Professor Hae-Won Park

ABSTRACT

In this thesis, a systematic framework for designing control for high-precision positioning stages of Velociprobe X-ray microscope at Advanced Photon Source (APS) at Argonne National Laboratory (ANL) is presented. In particular, our focus is on maintaining a precise position of the optics scanning stages in the XY lateral plane relative to the sample stages, which will ensure that the optics stages scans the focused X-ray spot on the sample along a predefined trajectory. We would also want to maintain a precise relative distance between the optics and sample in Z direction (direction of the X-ray beam) to make sure the X-ray spot size remains constant during a scan. Both precise positioning in lateral XY plane and constant relative displacement in beam direction would influence X-ray image spatial resolution and imaging bandwidth. Our framework facilitates control designs that achieve simultaneously specifications on tracking bandwidth and positioning resolution while guaranteeing robustness of the closed loop device to unmodeled uncertainties. To develop this framework, we used modern control techniques for modeling, quantifying design objectives and system-specific challenges, and designing the control laws. The control designs were implemented on a 3 degree of freedom piezo-actuated parallel kinematics stages dedicated for precision scanning of X-ray optics. Experimental results demonstrate significant improvements in positioning performance with H_∞ optimal controllers; for instance, improvements by over 134%, 149% and 132% in tracking bandwidths along X, Y, and Z stages, respectively, were demonstrated when compared to proportional-integral-derivative (PID) controller designs. Even with these high-bandwidth control designs, the positioning resolution of the order $1-2$ nanometers were achieved, which is approximately the same as the PID controllers. Two different X-ray imaging technique, namely step scan and flyscan, were successfully carried out with the controllers. In the step scan technique, the optics stages tracked a typical raster scan pattern and successfully scanned the X-ray spot covering a $1\,\mu\,m \times 1\,\mu\,m$ area on the sample in 2.1 minutes, with NI control hardware and H_∞ control design. This resulted in a 8 fold improvement in the imaging bandwidth compared to previously existing methods. In step scan technique, the X-ray spot is first positioned at point on the sample and corresponding diffraction pattern is recorded by the detector, then the X-ray spot is moved to

new position in next step and imaging is continued. In contrast, we enabled the flyscan, where the optics stage continuously tracked a custom square snake scan pattern to scan the focused X-ray spot over a $1\,\mu m \times 1\,\mu m$ area of the sample in 0.01 secs while simultaneously recording the diffraction patterns at the area detector. Flyscan of $1\,\mu m \times 1\,\mu m$ area was done over 10^4 times faster than step scan with our control design and over 10^5 times faster than previous step scan performance at the APS beamline.

In X-ray microscopy it is imperative that the relative position between the optics stage, that carries the X-ray focusing optics, and the sample stage follow a certain trajectory while either the optics or sample stage is being scanned. The state-of-the-art in X-ray microscopy at APS (as explained above) features an H_∞ control architecture applied to only the optics stage or both the optics and sample stage, achieving the objectives of large tracking bandwidth, good positioning resolution, rejection of environmental disturbance, attenuation of measurement noise, good X-ray diffraction image resolution and increased imaging bandwidth. However the sensors and the fixtures that hold the sensors drift with time due to changing air temperature at the APS beamline. The drift of the sensor affects the lateral position of the zone plate focusing optics in the XY plane during scanning relative to the sample stage and also the relative position between the optics and sample along Z direction. This results into imaging artifacts, image ambiguity and reduced image spatial resolution. Here, we identified this limiting factor and countered it by measuring the drift in real time and incorporated that in the optimal control architecture. We have shown that the effects of drift in the closed loop are practically removed. If our proposed method is adopted and applied to the X-ray microscope at APS beamline, it would significantly improve X-ray image spatial resolution and reduce imaging artifacts. We provide estimates of this improvements in this thesis.

To my parents and my wife

ACKNOWLEDGMENTS

I would like to thank my advisor, Dr. Srinivasa M. Salapaka for his patience, continuous guidance and encouragement throughout the years at UIUC. I would also like to thank my coadvisor Dr. Curt Preissner of Advanced Photon Source (APS) at Argonne National Laboratory (ANL) for his constructive advice and mentoring during my work at ANL.

I would also like to express my gratitude to my research colleagues at APS Christian Roehrig, Junjing Deng, Zhonghou Cai, Barry Lai, Stefan Vogt, Jorg Maser, David Vine, Shane Sullivan, Michael Wojcik, Paul Rossi, Michael Fries, Fabricio Marin, Matthew Kasa, Evan Maxey, and Max Wyman. I am very thankful to Christian Roehrig, principal electrical engineer at APS, for his help with the electronics and instrumentation at APS beamline. I would specially thank Junjing Deng, beamline scientist at APS, for his time and help at APS beamline and for all the X-ray images provided in this thesis. I would also like to thank Loretta Cokeley for all the help in administration work at APS.

I would like to express my thanks to my research colleagues at UIUC Mayank Baranwal, Ram Sai Gorugantu, Pratik Parekh, Amber Srivastava, Alireza Askarian, and Sreenath Sundar.

I would like to mention couple of my peers at UIUC Marcel Schuck, Christopher Valicka, Yue Sun, and Yijing Zhang and thank them for the time well spent.

Thanks to my parents, my elder sibling and my wife for their love and support.

Argonne National Laboratory's work was supported by the U.S. Department of Energy, Office of Science, Office of Basic Energy Sciences, under contract $DE\text{-}AC02\text{-}06CH11357$ and DOE STTR grant $DE\text{-}SC0004283$. This project is funded by DOE ANL $4J\text{-}30401\text{-}0007A$ and NSF CMMI grant 14-63239.

TABLE OF CONTENTS

LIST OF FIGURES vii

LIST OF TABLES xiv

LIST OF ABBREVIATIONS xv

CHAPTER 1 INTRODUCTION 1

CHAPTER 2 X-RAY MICROSCOPY AT A SYNCHROTRON 5
2.1 X-ray Imaging at Advanced Photon Source 5
2.2 Challenges of X-ray Imaging - Controls Perspective 8
2.3 Ptychography X-ray Imaging and Limitations 9
2.4 Impact of the Sensor Drift on X-ray Microscopy 13
2.5 Requirements of Different Scanning Techniques 13

CHAPTER 3 FAST AND ROBUST OPTIMAL CONTROL FOR VELOCIPROBE X-RAY MICROSCOPE 15
3.1 Velociprobe X-ray Microscope 16
3.2 Control Design for Velociprobe 34
3.3 X-ray Imaging with Velociprobe 60
3.4 Impact on X-ray Microscopy 67

CHAPTER 4 COUNTERING SENSOR DRIFT IN X-RAY MICROSCOPE 68
4.1 Drift Rejection Through Measurement 72
4.2 Control Design for Drift Rejection 79
4.3 Results for Drift Rejection 84
4.4 Impact on X-ray Microscopy 93

CHAPTER 5 DISCUSSION AND FUTURE DIRECTIONS 94

APPENDIX A APPENDIX FOR CHAPTER 2 96

APPENDIX B APPENDIX FOR CHAPTER 3 97

APPENDIX C APPENDIX FOR CHAPTER 4 102

REFERENCES 103

LIST OF FIGURES

2.1 (a) Advanced Photon Source (APS) at Argonne National Laboratory (ANL) is a synchrotron light source with a 7 GeV 1.1 km circumference electron storage ring. (b) The typical polygonal electron storage ring at a third generation light source. 5
2.2 Lorentz force applied on an electron beam, (a) bending magnet, and (b) undulator type insertion device. 6
2.3 Schematic diagram of Scanning Transmission X-ray Microscopy (STXM) technique for X-ray imaging at a synchrotron light source such as APS. The work presented in this thesis focuses on high-bandwidth high-precision positioning of the optics stages, which holds the zone pate focusing optics. Relative positioning of the optics and sample stages will also be studied. . . 7
2.4 Plot of brightness vs photon energy for different light sources operating under Department of Energy (DOE) in USA (Courtesy APS). 9
2.5 Ptychographic Coherent Diffractive Imaging (PCDI). 10

3.1 (a) Schematic of the Velociprobe X-ray microscope. The coarse stages are made of large granite blocks which are given motion utilizing state-of-the-art air bearing. The fine positioning zone plate XYZ stages, attached to the top granite gantry in an inverted orientation, is used to do high precision scanning of the focused X-ray spot to cover a target area on the sample. (b) The installed instrument at APS Sector 2 beamline. 16
3.2 Velociprobe fine scanning optics stage assembly on a table, before the final assembly in an inverted orientation under the granite gantry shown in Figure 3.1. In details, 1 = reference frame, 2 = PI parallel kinematics XYZ nanopositioning stages, 3 = sensor head sample Y axis, 4 = sensor head sample X axis, 5 = sensor head optics X axis, 6 = sensor head sample Z axis, 7 = sensor head optics Z axis, 8 = zone plate optics kinematic holder, 9 = sensor head optics Y axis, 10 = order sorting aperture, and 11 and 12 = Aluminum alloy fixtures that hold the sensors. 17
3.3 Velociprobe closed-loop system layout for the optics scanning stages. The sample stages are not shown here. 18
3.4 Band-limited uniform white noise with 5 nm amplitude is given as input to the X-stage. The resulting stage displacement is measured and used for fitting a model. 20

3.5 9 different non-parametric transfer function estimates calculated by Welch's method for (a) XX-stage identification, (b) YY-stage identification, and (c) ZZ-stage identification. Here, XX-stage means a model between X-stage input signal and X-stage output signal. 21
3.6 Averaged non-parametric transfer function from 9 different transfer function estimates for (a) XX-stage, (b) YY-stage, and (c) ZZ-stage. 22
3.7 Comparison between the averaged transfer function estimate calculation of the experimental FRF of XX-stage and the frequency response of the 15^{th} order fitted model G_{xx}. 23
3.8 Comparison between the averaged transfer function estimate calculation of the experimental FRF of YY-stage and the frequency response of the 13^{th} order fitted model G_{yy}. 24
3.9 Comparison between the averaged transfer function estimate calculation of the experimental FRF of ZZ-stage and the frequency response of the 33^{rd} order fitted model G_{zz}. 25
3.10 Comparison between the transfer function estimate calculation of the experimental FRF of YY-stage, the frequency response of the fitted 13^{th} order model, and frequency response of the reduced fitted 12^{th} order model. . 27
3.11 Comparison between the transfer function estimate calculation of the experimental FRF of ZZ-stage, the frequency response of the fitted 33^{rd} order model, and frequency response of the reduced fitted 28^{th} order model. 27
3.12 (a) Open loop step response of fitted model G_{xx}, and (b) Open loop tracking of sine wave with amplitude 1000 nm and frequency 100 Hz by the fitted model G_{xx}. 31
3.13 (a) Open loop step response of reduced model rG_{yy}, and (b) open loop tracking of sine wave with amplitude 1000 nm and frequency 100 Hz by the reduced model rG_{yy}. 32
3.14 (a) Open loop step response of reduced model rG_{zz}, and (b) Open loop tracking of sine wave with amplitude 1000 nm and frequency 100 Hz by the reduced model rG_{zz}. 32
3.15 Noise histogram of Velociprobe optics stage displacement in open loop, (a) X-stage with 3σ positioning resolution of 33 nm, (b) Y-stage with $3\,\sigma$ positioning resolution of 12 nm, and (c) Z-stage with $3\,\sigma$ positioning resolution of 29 nm. 33
3.16 Transfer function block diagram of PID controller in feedback loop. 34
3.17 A block diagram showing the step-by-step process of designing and implementing a controller. 35
3.18 A Biquad structure showing one second order section that can represent a second order transfer function. 36
3.19 Bode plot of a $149\,Hz$ $-3\,dB$ bandwidth PID controller for XX-stage. 37
3.20 Comparing the design and experimental closed loop transfer function for the scanning X stage. (a) Bode plot of $S_{xx,sim}$ and $S_{xx,exp}$, and (b) Bode plot of $T_{xx,sim}$ and $T_{xx,exp}$. 38

3.21 Comparing the design and experimental closed loop transfer function for the scanning Y stage. (a) Bode plot of $S_{yy,sim}$ and $S_{yy,exp}$, and (b) Bode plot of $T_{yy,sim}$ and $T_{yy,exp}$. 39
3.22 Comparing the design and experimental closed loop transfer function for the scanning Z stage. (a) Bode plot of $S_{zz,sim}$ and $S_{zz,exp}$, and (b) Bode plot of $T_{zz,sim}$ and $T_{zz,exp}$. 39
3.23 X-Stage sine wave reference tracking for 149 Hz -3 dB bandwidth PID controller, (a) 1000 nm amplitude 100 Hz sine wave reference tracking, and (c) 1000 nm amplitude 200 Hz sine wave reference tracking. (b) and (d) are the corresponding tracking error. 41
3.24 For Velociprobe X-Ray microscope XY-plane is the scanning plane, which is vertical to the incoming X-ray beam along Z-axis. Two different sine wave reference with same amplitude of 1000 nm and frequency 100 Hz and 200 Hz, respectively, were given to the Y-stage for tracking performance verification of a 134 Hz -3 dB bandwidth PID controller. Here, (a) 1000 nm amplitude 100 Hz sine wave reference tracking, and (c) 1000 nm amplitude 200 Hz sine wave reference tracking. (b) and (d) are the corresponding tracking error. The tracking error is much larger in case of 200 Hz frequency reference since it is beyond the -3 dB bandwidth of the PID controller for Y-stage. 200 Hz reference frequency was chosen to compare tracking performance with robust optimal controller, which is shown in later sections 42
3.25 Comparing noise histogram of Velociprobe optics stage displacement in open loop and closed loop with PID controller; (a) X-stage closed loop 3σ positioning resolution with PID is 1.9 nm compared to 33 nm open loop resolution, (b) Y-stage closed loop 3σ positioning resolution with PID is 1.5 nm compared to 12 nm open loop resolution, and (c) Z-stage closed loop 3σ positioning resolution with PID is 2.0 nm compared to 29 nm open loop resolution. 43
3.26 Closed loop transfer function block diagrams for the $S\backslash T\backslash KS$ mixed sensitivity minimization problem. (a) Closed loop system with the identified plant model G, reference r, controller output u, measurement noise n, design weights W_s, W_t, W_u, and regulated outputs $z = [z_s\ z_t\ z_u]^T$, (b) Generalized plant framework with the transfer function going from exogenous inputs $w = [r\ d\ n]^T$ to regulated outputs z to be minimized to achieve the optimum control law K. The error signal $v = r - y_m$ available to the controller is utilized to give the proper controller output u. Here, $y_m = y + n$ is the measured displacement of the stages. 44
3.27 The weighting transfer functions W_{sx}, W_{tx}, and W_{ux} for the Velociprobe optics scanning X-stage corresponding to the H_∞ controller with -3 dB bandwidth 200 Hz and -40 dB bandwidth of 2.6 Hz. 49
3.28 Bode diagram of the identified stage model G_{xx}, controller K_{xx}, sensitivity transfer function S_{xx} and complementary sensitivity transfer function T_{xx} are shown here. 50

3.29 The weighting transfer functions W_{sy}, W_{ty}, and W_{uy} for the Velociprobe optics scanning X-stage corresponding to the H_∞ controller with -3 dB bandwidth 200 Hz and -40 dB bandwidth of 2.6 Hz. 51
3.30 Bode diagram of the identified stage model G_{yy}, controller K_{yy}, sensitivity transfer function S_{yy} and complementary sensitivity transfer function T_{yy} are shown here. 51
3.31 The weighting transfer functions W_{sz}, W_{tz}, and W_{uz} for the Velociprobe optics scanning X-stage corresponding to the H_∞ controller with -3 dB bandwidth 200 Hz and -40 dB bandwidth of 2.7 Hz. 52
3.32 Bode diagram of the identified stage model G_{zz}, controller K_{zz}, sensitivity transfer function S_{zz} and complementary sensitivity transfer function T_{zz} are shown here. 53
3.33 Comparing the design and experimental closed loop transfer function, (a) Bode plot of $S_{xx,sim}$ and $S_{xx,exp}$, and (b) Bode plot of $T_{xx,sim}$ and $T_{xx,exp}$ . . . 54
3.34 Comparing the design and experimental closed loop transfer function, (a) Bode plot of $S_{yy,sim}$ and $S_{yy,exp}$, and (b) Bode plot of $T_{yy,sim}$ and $T_{yy,exp}$ . . . 55
3.35 Comparing the design and experimental closed loop transfer function, (a) Bode plot of $S_{zz,sim}$ and $S_{zz,exp}$, and (b) Bode plot of $T_{zz,sim}$ and $T_{zz,exp}$ . . . 55
3.36 X-Stage sine wave reference tracking for 200 Hz -3 dB bandwidth H-infinity controller, (a) 1000 nm amplitude 100 Hz sine wave reference tracking, and (c) 1000 nm amplitude 200 Hz sine wave reference tracking. (b) and (d) are the corresponding tracking error. 56
3.37 Y-Stage sine wave reference tracking for 200 Hz -3 dB bandwidth H-infinity controller, (a) 1000 nm amplitude 100 Hz sine wave reference tracking, and (c) 1000 nm amplitude 200 Hz sine wave reference tracking. (b) and (d) are the corresponding tracking error. 57
3.38 X-stage closed-loop noise histogram with a 200 Hz bandwidth H-infinity controller giving a resolution of approx 1.9 nm. Whereas the open loop resolution is approx 33 nm. 58
3.39 Y-stage closed-loop noise histogram with a 200 Hz bandwidth H-infinity controller giving a resolution of approx 1.4 nm. Whereas the open loop resolution is approx 12 nm. 59
3.40 Z-stage closed-loop noise histogram with a 113 Hz bandwidth H-infinity controller giving a resolution of approx 1.9 nm. Whereas the open loop resolution is approx 29 nm. 59
3.41 Step scan image of a Siemens Star pattern by (a) and (b) zone plate only and open loop mode, (c) and (d) zone plate only and closed loop mode with the H_∞ controllers in diagonal, and (e) and (f) differential mode and closed loop mode with the H_∞ controllers in diagonal. (b), (d), and (f) are the phase change of the X-ray recovered using the Extended Ptychographic Iterative Engine (ePIE). 61
3.42 Flyscan X-ray image of a Siemens Star in Zone Plate Only Mode in closed loop. The detector trigger frequency is 500 Hz. (a) and (b) PID controller, and (c) and (d) H_∞ controller. 63

3.43 Flyscan X-ray image of a Siemens Star in Zone Plate Only Mode in closed loop. The detector trigger frequency is 1 kHz. (a) and (b) PID controller, and (c) and (d) H_∞ controller. 64
3.44 Flyscan X-ray image of a Siemens Star in Zone Plate Only Mode in closed loop. The detector trigger frequency is 2 kHz. (a) and (b) PID controller, and (c) and (d) H_∞ controller. 65
3.45 Flyscan X-ray image of a Siemens Star in Zone Plate Only Mode in closed loop. The detector trigger frequency is 3 kHz. (a) and (b) PID controller, and (c) and (d) H_∞ controller. 66

4.1 Velociprobe fine scanning optics stage assembly on a table, before the final assembly in an inverted orientation under the granite gantry shown in Figure 3.1. In details, 1 = reference frame, 2 = PI parallel kinematics XYZ nanopositioning stages, 3 = sensor head sample Y axis, 4 = sensor head sample X axis, 5 = sensor head optics X axis, 6 = sensor head sample Z axis, 7 = sensor head optics Z axis, 8 = zone plate optics kinematic holder, 9 = sensor head optics Y axis, 10 = order sorting aperture, and 11 and 12 = Aluminum alloy fixtures that hold the sensors. The Attocube Laser interferometric sensor heads are strategically positioned so as to measure the XYZ optics and sample stage displacement. The zone plate optics holder is attached kinematically on the cross-shaped Aluminum alloy fixture, which is in turn bolted on to the PI stage. For displacement measurement of the optics stage, mirrors (not shown here) are glued on the zone plate holder, so that the laser coming out of the standard Attocube focusing sensor heads can reflect back to the sensor heads. 69
4.2 Temperature log of over 24 hour recorded at Sector-2 experimental hutch at the APS beamline. (a) The air temperature in the experimental hutch, and (b) the sample stage temperature measured at the base. 70
4.3 Schematic diagram showing the effect of thermal drift of the sensor fixtures on the measurement of X-ray microscope scanning stage displacement. 71
4.4 Schematic diagram showing the additional laser interferometer sensor introduced on the reference base to measure the sensor drift. 72
4.5 Experimental setup at APS used to prove the method of countering thermal drift of sensor in real time through measurement. Here, 1 = reference frame, 2 = Attocube IDS 3010 laser interferometric sensor, 3 = environmental compensation unit (ECU) for Attocube IDS 3010, 4 = PI piezo actuator, 5 = Aluminum alloy bar A, 6 = mirrors for reflecting Lasers sourcing from sensor heads, 7 = Sensor Head A, 8 = Sensor Head B, 9 = Aluminum alloy bar B, 10 = ultra thin flexible heat sheet, and 11 = Aluminum alloy post. 73
4.6 Schematic showing the closed-loop system layout for the thermal drift rejection experiment. 74
4.7 Band-limited uniform white noise (green) with 1500 nm amplitude is given as input to the PI actuator. The resulting actuator displacement (blue) is measured and used for system identification. 75

4.8 Comparison between the experimental plant frequency response (blue) and the transfer function estimate calculation (green). 76
4.9 Comparison between the transfer function estimate calculation of the experimental FRF of the actuator and frequency response of the fitted 23^{rd} order model. 77
4.10 Comparison between the transfer function estimate calculation of the experimental FRF of the actuator, frequency response of the fitted 23^{rd} order model G_1 and reduced 18^{th} order model rG_1. 78
4.11 Comparison of the open loop step response (in simulation) of fitted plant model (23^{rd} order) and reduced plant model (18^{th} order). 78
4.12 Open loop tracking (in simulation) of Sine wave with 1000 nm amplitude and 50 Hz frequency by the fitted plant model and reduced plant model. . . 79
4.13 Transfer function block diagram of the negative feedback control architecture for the sensor drift rejection scheme. Here, G_1 is experimentally identified actuator model, K_1 is the designed controller, y_1 is the actuator displacement, d_1 is the actuator thermal drift, n_1 and n_{d1} are the measurement noise for the actuator position and sensor thermal drift. 79
4.14 (a) Transfer function block diagram of the H_∞ mixed-sensitivity minimization problem, which incorporates the measured sensor thermal drift d_1 in the optimal control architecture. Here, W_s, W_u, and W_t are the design weights and $z = [z_s\ z_u\ z_t]^T$ are the regulated outputs. (b) Generalized control format of the optimal control problem, where P is the generalized plant, $w = [r - d_1\ n_1\ n_{d_1}]^T$ are the exogenous inputs. 80
4.15 Bode diagram of the design weights W_s, W_t, and W_u for a particular H_∞ controller design. 81
4.16 (a) Bode diagram of the actuator model G_1 and the designed H_∞ controller K_1. (b) Bode diagram of the closed-loop transfer functions S_1 and T_1. 82
4.17 Comparing the design and experimental closed loop transfer function, (a) Bode plot of $S_{1,sim}$ and $S_{1,exp}$, and (b) Bode plot of $T_{1,sim}$ and $T_{1,exp}$ 83
4.18 In this tracking experiment the open loop system has no knowledge (a) Open loop tracking for a sinusoidal reference trajectory with 1000 nm amplitude and 8 Hz frequency, (b) Magnified plot of the open loop tracking, (c) open loop tracking error $e_1 = r_1 - y_1$, (d) magnified plot of the open loop tracking error, and (e) drift d_1 observed during the open loop tracking experiment. 85
4.19 (a) Open loop tracking for a sinusoidal reference trajectory with 1000 nm amplitude and 8 Hz frequency, (b) Magnified plot of the open loop tracking, (c) open loop tracking error $e_1 = r_1 - y_1 - d_1$, (d) magnified plot of the open loop tracking error, and (e) drift d_1 observed during the open loop tracking experiment. 87

4.20 (a) Closed-loop tracking for a sinusoidal reference trajectory with 1000 nm amplitude and 8 Hz frequency with no knowledge of the thermal drift of the sensor, (b) Magnified plot of the same closed-loop tracking shows perfect tracking with very small tracking error, (c) closed loop tracking error, (d) magnified plot of the closed loop tracking error, and (e) Drift observed observed during the closed loop tracking experiment. 88
4.21 (a) Closed-loop tracking for a sinusoidal reference trajectory with 1000 nm amplitude and 8 Hz frequency with the measured thermal drift being part of the feedback signal $y_1 + d_1$, (b) Magnified plot of the closed-loop tracking, (c) closed loop tracking error, (d) magnified plot of the closed loop tracking error, and (e) Drift observed observed during the closed loop tracking experiment. 89
4.22 Noise histogram of experimental actuator displacement in open loop with the 3σ positioning resolution is 35.6 nm. The open loop displacement is y_1 and has no knowledge of drift signal. 91
4.23 Noise histogram of experimental actuator displacement y_1 in closed loop with the H-infinity controller with bandwidth 70 Hz. The 3σ positioning resolution is 18.7 nm. The drift signal is not fed back to the controller in this case. The feedback to the H_∞ controller in this case is y_1 91
4.24 Noise histogram of experimental actuator displacement with measured sensor drift added to it (i.e. $y_1 + d_1$) in closed loop with the H-infinity controller with bandwidth 70 Hz. The 3σ positioning resolution is 3.8 nm. The feedback to the H_∞ controller in this case is $y_1 + d_1$ 92

LIST OF TABLES

3.1 Poles and Zeros of Velociprobe Optics XX-stage model G_{xx} 28
3.2 Poles and Zeros of Velociprobe Optics YY-stage Reduced model rG_{yy} 29
3.3 Poles and Zeros of Velociprobe optics scanning ZZ-stage reduced model rG_{zz} 30

LIST OF ABBREVIATIONS

APS	Advanced Photon Source
ANL	Argonne National Laboratory
PSD	Power Spectral Density
DOF	Degree Of Freedom
DTFT	Discrete-Time Fourier Transform
FPGA	Field Programmable Gate Array
LHP	Left Half Plane
NI	National Instruments
PI	Physik Instrumente
PSD	Power Spectral Density
RHP	Right Half Plane
RIO	Reconfigurable Input/Output
SPM	Scanning Probe Microscopy
STXM	Scanning Transmission X-ray Microscopy
FRF	Frequency Response Function
ECU	Environmental Compensation Unit

CHAPTER 1

INTRODUCTION

X-ray microscopy is having a dramatic impact on fields as diverse as biological and life science, geo/soil science, environmental science, polymer science, physics and chemistry. The high spatial resolution (30 nm or better) and the high penetration of samples ($10 - 100\,\mu m$) enable users to perform measurements not accessible with either electron or scanning probe microscopes ([6], [8], [9], [18], [25], [28], [32]). The X-ray microscope is a well-established tool at the third-generation synchrotron facilities such as, but not limited to, the Advanced Photon Source (APS) at Argonne National Laboratory (ANL), National Synchrotron Light Source II ($NSLS-II$) at Brookhaven National Laboratory (BNL), European Synchrotron Radiation Facility (ESRF) in France, Super Photon Ring-8 GeV (SPring-8) in Japan, and Positron-Electron Tandem Ring Accelerator III (PETRA-III) in Germany.

Third-generation synchrotron light sources are particle accelerator systems in which an electron beam is passed through special magnet arrays called insertion devices, to produce intense and partially-coherent beams of X-rays. Recent developments in accelerator technology are enabling improved electron beam qualities, with a dramatic 100 times improvement in the brightness of the resulting X-ray beam ([11]). The improved brilliance and higher coherent fraction of X-rays from these new accelerators have the potential to improve the performance of X-ray microscopes by allowing for a finer focus, shorter experiment times, and higher efficiency. X-ray optics are also continuing to improve and it is reasonable to expect the advent of optics capable of focusing below 10 nm ([20]). For scientific users to take full advantage of the combined improvements in the X-ray beam and optics, a commensurate improvement in the instrumentation engineering of the X-ray microscope is needed. An especially significant performance enhancement can be achieved by making substantial changes to the control approach for the X-ray optics fine scanning stages. The motion control of the optics scanning stages will result in better closed loop tracking bandwidth and high positioning resolution, which in turn will improve the spatial resolution of the X-ray image and imaging bandwidth. In this work, we present a new control architecture for fine positioning of X-ray microscope optics scanning stages that offers significant improvements over the state of the art in tracking bandwidth, positioning resolution, disturbance rejection,

and noise attenuation.

Scanning transmission X-ray microscopy (STXM) is a high spatial resolution imaging technique, where X-ray beam is focused to a small spot (20 nm or less) on the sample and the intensity of the transmitted X-rays is recorded. An image is obtained by scanning the X-ray spot on the sample in a plane orthogonal to X-rays. The microscope resolution is determined both by the X-ray beam focusing ability of the zone plate optics and the stability of the optics stage stack and the sample stage stack. Any relative motion between the optics and the sample, resulting from the motion of the respective stage stacks, manifests as a larger focused X-ray spot on the sample and subsequent reduced spatial resolution of the X-ray image. Also the optics XY scanning stages should track the reference trajectory (raster scan pattern) with minimal tracking error, and with good positioning resolution, which will improve the X-ray image spatial resolution. In this article, our controller design concentrates on a STXM scanning system which is part of novel in-house designed X-ray microscope known as Velociprobe, which provides motion on the order of 1 nm to optics stages, and therefore has a significant contribution to the X-ray image quality. The positioning systems that provide coarse motion to the optical stages to bring the beam to the region of interest on the sample are not essential to the work described in this thesis. The work here focuses on improving the performance of fine-positioning (nm scale) stages that determine the relative position between the optics (on optics stage assembly) and the sample (on sample stage assembly), which mainly determines the resolution and bandwidth of X-ray imaging; especially in imaging techniques such as step scan and flyscan. It should be remarked that other X-ray microscopy techniques such as ptychography ([7], [21], [22], [26]) and scanning X-ray fluorescence microscopy [42] can also take advantage of better positioning resolution.

Typically X-ray microscope high-resolution positioning systems comprise piezo-actuated, high-stiffness flexure stages stacked in series or piezo actuated parallel kinematics stages. The main challenges in designing control laws for such systems arise from the limitations imposed by structural dynamics, modeling uncertainties (including environmental disturbances, parameter variations, and piezo nonlinearities), and noisy measurements, the combined effects of which severely limit the positioning performance. Moreover, X-ray microscopy applications demand high specifications on performance: nanometer-scale positioning resolution, closed loop bandwidths that are close to the positioning stage resonant frequencies, millimeter-scale travel range, and repeatability, all in the presence of unmodeled uncertainties.

State-of-the-art X-ray microscopes fine-motion stages typically use proportional, proportional-integral, or proportional-integral-derivative (P, PI, PID) control, PID augmented with var-

ious types of filters, and some feed-forward control methods ([6], [10]). These model-independent architectures, while easily available as commercial motion control hardware, have limited ability to address limitations of mechanics, actuators, and motion controller; in many cases these architectures are ill suited to low-damped systems such as the flexure stages ([32]). Our approach is a means to directly address these limitations in a way not previously used in the context of X-ray microscope. While some authors have brought the small form-factor concept of scanning probe microscopy (SPM) to the realm of the X-ray microscope [15], no one has applied the tools of modern control design for fine-motion control to the X-ray microscope application as has been done in SPM applications. Only work done with modern control design was our previous work [12] on the Early User Instrument (EUI) X-ray microscope at APS, where significant improvement in tracking bandwidth and positioning resolution was achieved using the H_∞ optimal control architecture.

In the framework presented, the control design is obtained by solving an optimization problem which incorporates multiple performance specifications. The specifications include high tracking bandwidth, high positioning resolution, robust tracking of reference signals, which in turn require disturbance rejection and noise attenuation objectives, and bounded control effort for feasible implementation. The approach determines if a given set of specifications are feasible, and when they are, it yields an optimal control law. It also allows a designer to make tradeoffs between positioning resolution, tracking bandwidth and robustness. These tools open the possibility of optimizing the performance of an X-ray microscope for specific applications and desired specifications by managing the tradeoff between the positioning resolution and the reference tracking bandwidth while simultaneously limiting the influence of unmodeled uncertainties such as environmental noise, for instance optimizing high tracking bandwidth for step scanning and fly-scanning or high positioning resolution for fluorescence microscopy.

For high spatial resolution x-ray imaging the relative motion of the optics scanning stage and sample stage needs to follow a predefined trajectory with small tracking error, high tracking bandwidth, good positioning resolution while being robustly stable to unmodeled uncertainties. The control architecture presented up to now is based on an assumption that the high-precision displacement sensors used for measuring the fine scanning stage displacements are stationary with respect to the global reference frame. But due to the cyclic temperature change in the experimental hutch at APS the Aluminum alloy sensor fixtures drift thermally by couple hundred nanometers. This results into positioning error of the scanning stages since the sensor interprets itself drifting as a motion of the target stages. Running a controller does not improve anything since the controller has no knowledge of the

drift and compensates for the sensor drift by treating it as stage motion. In this thesis, we are proposing a method of countering this sensor drift through measurement and optimal control architecture.

This article is organized as follows. Chapter 2 describes the X-ray imaging details at Synchrotron light source, Ptychographic X-ray imaging technique, and the objectives, challenges and limitations of X-ray imaging. Chapter 3 the Velociprobe X-ray microscope, system identification for optics scanning stages, control design methodology, results comparison between open loop and closed loop, X-ray microscopy techniques, comparing X-ray image generated at the APS. Chapter 4 details the source of sensor drift in X-ray microscope, how to counter sensor drift through optimal control architecture and discussion on the experimental results. In Chapter 5 we discuss the work presented in this thesis and future directions. Chapter 2 would be easy read and tutorial like for X-ray scientists. Chapter 3 and Chapter 4 would be tutorial like for control engineers.

CHAPTER 2

X-RAY MICROSCOPY AT A SYNCHROTRON

The work presented in this thesis covers the application of fast and robust optimal control to X-ray microscopy field, specifically to improve the performance of X-ray microscopes in terms of image spatial resolution and imaging bandwidth. To put the control design work in the context of X-ray microscopy for the readers different relevant aspects and theories will be presented here. Section 2.1 will introduce the APS synchrotron light source, how X-rays are produced at APS, and where our works comes into focus within the X-ray microscopy process. Section 2.2 details the challenges and limitations in X-ray imaging and how it may be addressed. In section 2.3, a particular X-ray imaging technique, ptychography, and the its limitations will be explained. Section 2.4 puts forward the idea of sensor drift and how it affect X-ray imaging in terms of imaging quality and imaging bandwidth. Section 2.5 will explain the state-of-the-art in scanning techniques used to do X-ray imaging.

2.1 X-ray Imaging at Advanced Photon Source

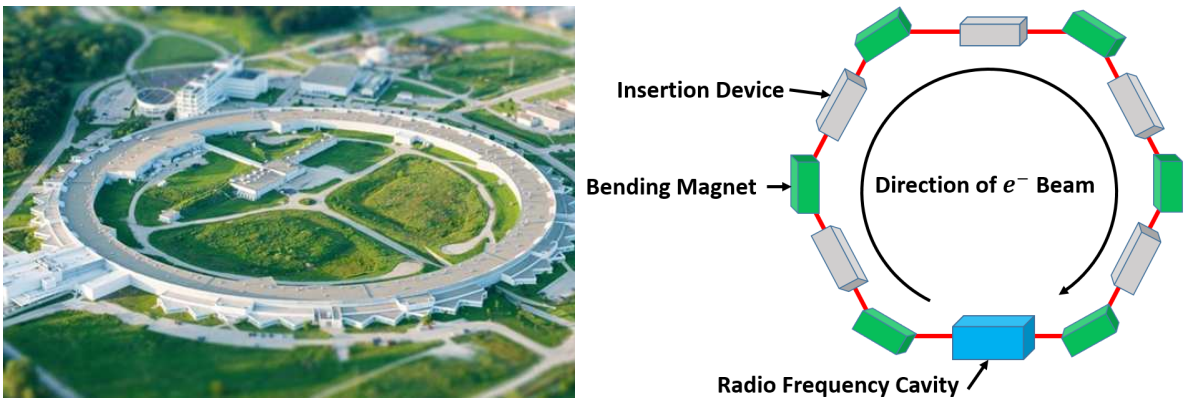

(a) (b)

Figure 2.1: (a) Advanced Photon Source (APS) at Argonne National Laboratory (ANL) is a synchrotron light source with a 7 GeV 1.1 km circumference electron storage ring. (b) The typical polygonal electron storage ring at a third generation light source.

APS at ANL is a third generation synchrotron light source, producing ultra-bright, high-energy X-ray beams for research (Figure 2.1a). A 7 GeV energy electron beam is maintained in the 1.1 km circumference electron storage ring at APS. This electron storage ring is actually a very large polygon (Figure 2.1b), consisting of straight sections (accommodating insertion devices such as wigglers and undulators, radio-frequency cavities and so on) and corner sections (accommodating the bending magnets). The bending magnets introduce magnetic field perpendicular to the electron beam, which in turn results in Lorentz force on the electron beam perpendicular to the direction of both the electron beam and the magnetic field (Figure 2.2a). This Lorentz force makes the electrons turn around a suitable circular arc at each corner of the polygonal storage ring. The Lorentz force acting on the electron beam at the bending magnets also accelerates the electrons along the circular path resulting in electromagnetic radiation (including X-rays).

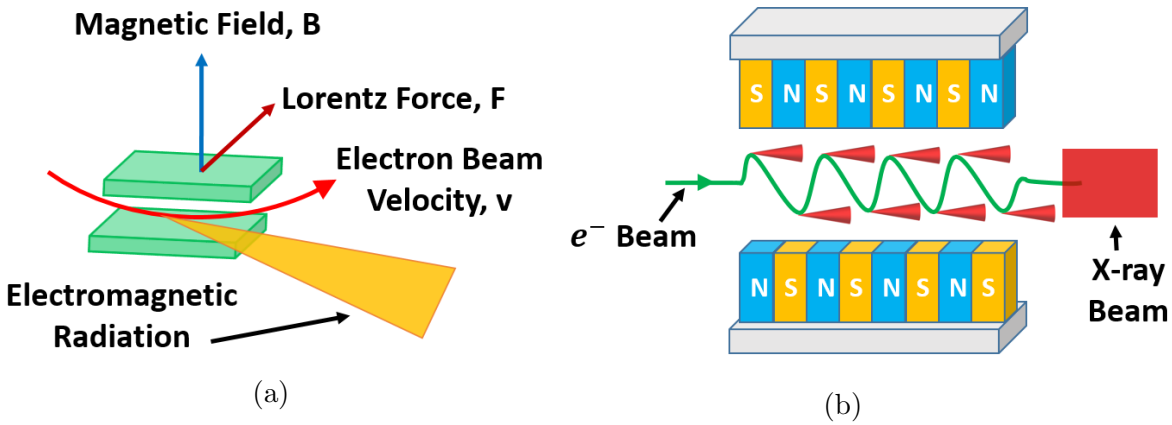

Figure 2.2: Lorentz force applied on an electron beam, (a) bending magnet, and (b) undulator type insertion device.

APS, being a third generation synchrotron light source, can accommodate insertion devices in the straight sections of the storage ring. These insertion devices follow the same principle as the bending magnets to agitate electron beam to produce X-ray beams. The insertion devices used at APS are known as undulators (Figure 2.2b), which are made up of a series of alternatively polarized electromagnets. These alternatively polarized electromagnets accelerates the electrons in the electron beam in inward and outward directions alternatively around $30 - 40$ times to produce electromagnetic radiation at each of acceleration instances or at each undulations. These electromagnetic radiations goes through a constructive or destructive interference downstream of the undulator (depending on the setup of the undulator magnets) to produce a wide-band electromagnetic radiation including X-rays. The electron beam loses energy every time it goes through a bending magnets and

insertion devices. The radio frequency (RF) cavities are used to replenish the energy lost from the storage ring electron beam by accelerating the electrons in the cavity. Also an electron injector unit is used to inject packet of electrons, having the energy same as that of the storage ring electrons, into the storage ring at a certain predefined interval.

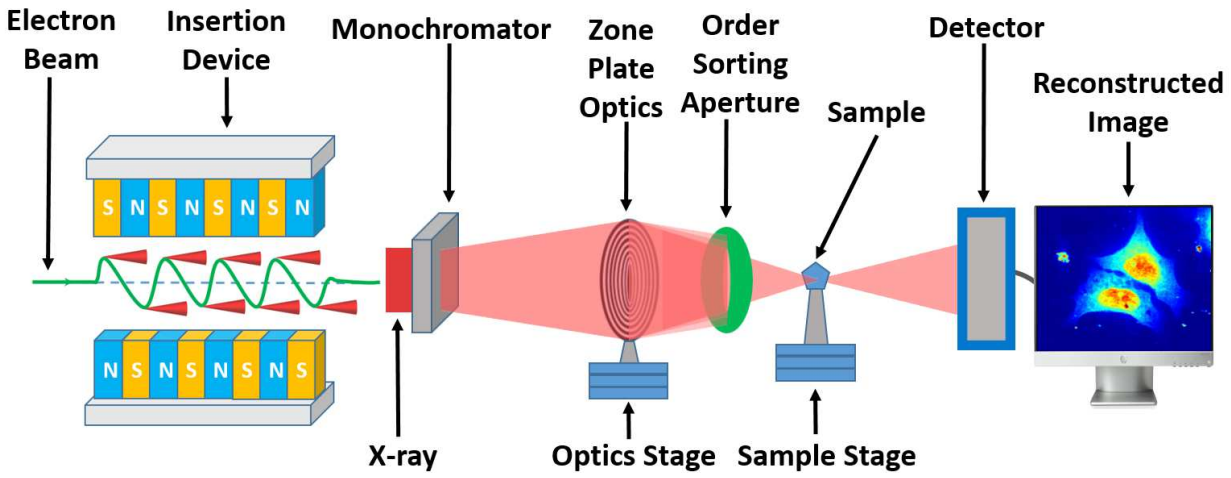

Figure 2.3: Schematic diagram of Scanning Transmission X-ray Microscopy (STXM) technique for X-ray imaging at a synchrotron light source such as APS. The work presented in this thesis focuses on high-bandwidth high-precision positioning of the optics stages, which holds the zone pate focusing optics. Relative positioning of the optics and sample stages will also be studied.

The X-ray microscope that was used to showcase the benefits of the fast and robust optimal control was specifically designed to operate with a specific imaging technique. This conventional imaging technique known as Scanning Transmission X-ray Microscopy (STXM) will be explained here. The schematic in Figure 2.3 gives an overall picture of STXM technique. An undulator type insertion device (as explained earlier) is used to produce wide-band electromagnetic radiation containing mainly hard X-rays or soft X-rays. The type of X-rays produced (of course with some background radiation) depends on the tunable electromagnet spacing of the undulator. Hard X-rays have higher energy ($10 - 100$ keV), shorter wavelength ($0.1 - 0.01$ nm) and more penetration capability, which is useful for imaging thick and dense samples. On the other hand, soft X-rays have less energy ($0.1 - 10$ keV), larger wavelength ($10 - 0.1$ nm) and has less penetration capability suitable for imaging soft, less dense and biological samples. This wide-band electromagnetic radiation is not ideal for most X-ray imaging experiments. To remove the electromagnetic radiation with unwanted wavelengths and background radiation a single crystal monochromator is used to produce a beam of radiation with narrow wavelength distribution (Figure 2.3). This narrow-band

X-ray beam exiting the monochromator is then focused as a spot on the sample with zone plate focusing optics. The zone plate optics, which is placed on the optics fine positioning stages, is scanned to track the focused X-ray spot along a predetermined trajectory to cover the region-of-interest on the sample. The incident X-rays penetrates and interacts with the sample at the atomic level. Some of the X-rays are absorbed while the remaining X-rays are transmitted through the sample. During the transmission of the X-rays through a sample diffraction and change in phase takes place. The detector downstream of the sample records the intensity of the transmitted X-rays, but has no knowledge of the phase. The X-ray intensity is recorded at predefined displacement interval of the optics stage for step scan and recorded continuously in case of flyscan. The phase change information is retrieved by solving the "phase problem" (Appendix A), which is a phase retrieval algorithm that utilizes the diffraction pattern recorded at the detector and the knowledge of the probe (the wavefront characteristics of the incident X-ray beam) in an iterative manner. In this process we get two images that gives a comprehensive information of the sample; first image is the intensity measured directly at the detector which gives a measure of X-ray absorption by the sample and second image gives a measure of phase change of transmitting X-ray as it passes through the sample and interacts with it. From the absorption image and phase change image we can study the internal structure and function of the sample.

2.2 Challenges of X-ray Imaging - Controls Perspective

Proper operation of the STXM technique depends on high precision scanning of the optics stage, relative stability of the sample in terms of the optics, thermal stability of the whole microscope structure under diverse conditions ranging from room temperature to cryogenics, and highly sensitive and fast detection of diffracted X-rays exiting the sample. Any disturbance or vibration sourcing from the optics stage during scanning operation will affect the X-ray image significantly. The positioning resolution and tracking bandwidth of the optics scanning stages determines the achievable X-ray imaging resolution and imaging bandwidth. Designing a controller which gives the flexibility of achieving multitude of closed loop objectives such as large tracking bandwidth, good positioning resolution, robustness to unmodeled system dynamics, good disturbance rejection and adequate noise attenuation is crucial for overall performance of the X-ray microscope.

The APS Upgrade (APS-U) project that started on 2011 is capable of providing 100 times increase in X-ray flux compared to the current APS. (Figure 2.4) shows the plot of brightness vs photon energy comparison for different light sources that are operating under the US DOE.

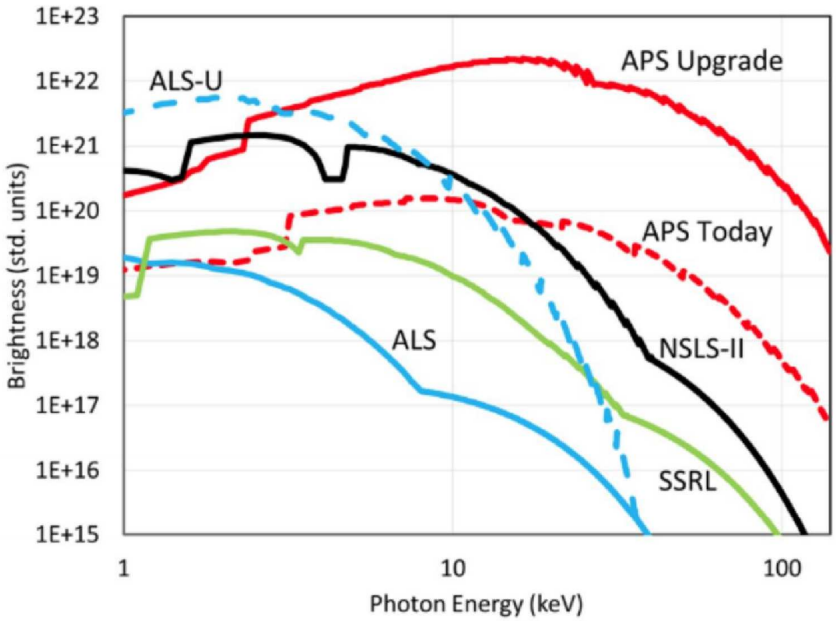

Figure 2.4: Plot of brightness vs photon energy for different light sources operating under Department of Energy (DOE) in USA (Courtesy APS).

The standard unit of brightness (or brilliance) is $photons/s/mm^2/(mrad)^2/(0.1\%BW)$. Brightness incorporates the number of photons per second in an unit cross-sectional area of the beam, with the photons having unit angular divergence (gives a measure of how fast the photons in the beam spread) and the photons that are within a bandwidth of 0.1% around the central frequency. The brighter the beam of X-rays the more compact focused spot can be achieved resulting into more detailed data collection in shorter time. The bright and high energy X-rays of APS-U enables X-ray imaging of fast events such as biological processes in living organisms in real-time with more details. To complement APS-U fast and robust scanning of the X-ray microscope optics stage in real-time with nm to sub-nm positioning resolution and large operating bandwidth is necessary. Other challenges and limitations will be explained in the particular scenarios of the next three sections.

2.3 Ptychography X-ray Imaging and Limitations

One of the prevalent X-ray imaging routine used for doing STXM in synchrotron light sources is Ptychography. For the better application of robust optimal control in X-ray microscopy field we need to understand the challenges involved with ptychography and then address them methodically. Ptychography is a Coherent Diffractive Imaging (CDI, Appendix A) technique where the consecutive X-ray spots focused on the sample is overlapped by $30\% - 70\%$ and

the corresponding diffraction patterns are recorded at the detector downstream. These diffraction pattern are used to solve the "phase problem" to recover the phase information of the sample. The overlapping of illuminated area gives high redundancy in the recorded data which strongly facilitates the sample reconstruction process. Let us consider a rectangular sample (Figure 2.5) with a region of interest being the blue square area at the upper left corner. In ptychography imaging technique first the circular probe (focused X-ray spot) is positioned on to location 1 and the corresponding diffraction pattern is recorded. Then the probe is moved through positions 2, 3, and 4, all the while recording the corresponding diffraction patterns. The probe in one location overlaps with the adjacent probe locations both in horizontal and vertical directions in the scanning plane. These four diffraction data resulting from overlapping probe locations are then used to retrieve the phase information of the sample.

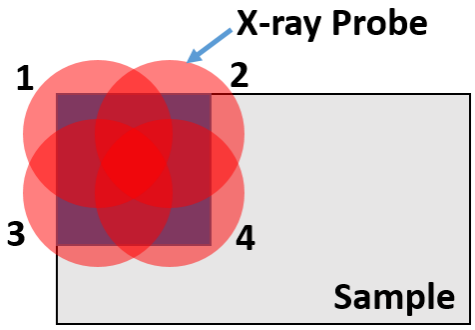

Figure 2.5: Ptychographic Coherent Diffractive Imaging (PCDI).

2.3.1 Limitations of Ptychography

Ptychographic CDI have following limitations that effect the quality of the images and the overall imaging procedure.

- Ptychographic scanning of a target region of a sample can take several hours to weeks depending on the size of the region of interest on the sample, the percentage of overlap chosen between consecutive probe position, size of the probe (size of the X-ray spot) and the particular optics scanning stages and sample stages.
- X-ray ptychography is very sensitive to drift between the illumination probe and the object. In other words, if the sample stage drifts relative to the optics stage then the recorded diffraction patterns will be offset and the reconstructed image will be different

from the sample. This affects image spatial resolution, image stitching issues, image ambiguity resulting from the phase retrieval algorithm and so on.

- Global errors such as rotation and scaling during X-ray tomography.

2.3.2 Addressing Drift - A Key Limitation of Ptychography

Since drift between the probe (focused X-ray spot) and the sample has a significant impact on the ptychography X-ray imaging technique, different methods are present in the literature that tried to address this drift. In one method, linear and non-linear drift models are used to correct for drift [16]. In these techniques the drift models are applied during post-processing, after collecting all the diffraction patterns corresponding to a particular scan. These drift models are an approximation and the process of reconstruction of the whole image becomes more time and resource consuming. A second method, uses a position correction term and incorporates it in the ptychographic iterative engine (PIE) (Appendix A), which is a phase retrieval algorithm, to counter drift. This is known as the position correcting PIE (pcPIE) method [19]. This is also done during the post-processing of the recorded diffraction patterns. In a third method, multiple diffraction pattern corresponding to the same probe position on the sample is collected and then the diffraction patterns that are closely cross-correlated are averaged. The final image of the whole sample is based on the reconstruction algorithm using the averaged diffraction patterns for each probe locations on the sample [24].

The details of the last method (Vine et al.) of countering drift will be addressed here to fully understand the benefits and limitations. In a ptychographic X-ray imaging of the sample shown in Figure 2.5 with four overlapping probe position we choose the probe overlap to be between $40\% - 60\%$. The probe will be stepped through locations 1, 2, 3, and 4 at a certain interval. The area of interest is the blue square region on the top left corner of the rectangular sample. In the first step, the X-ray probe is moved to location-1 and held fixed at that location for time $T_0 = 30$ seconds to let the X-ray microscope settle down and stabilize. Every time the probe is moved to a new position, T_0 is the overhead needed before any more measurements can be made. Then $n = 500$ exposures are taken at the location-1 with each exposure having a duration of $T_e = 1$ second. Here, exposure means, X-ray would pass through the location-1 probe cross-section and one diffraction pattern would be recorded for 1 second with the area detector during this exposure. After collecting the diffraction pattern corresponding to one exposure the detector cannot collect data for a short period of time $T_d = 2.3$ msec (in case of Pilatus detector). In this process total 500 exposures are taken at location-1. Here, T_0 = total overhead time chosen to let the

microscope settle down, T_e = exposure time, T_d = detector dead time, and n = number of exposures. Total time required for collecting diffraction data for location-1 T_1 and total time of the $4-$ probe location experiment shown in Figure 2.5 T are given as follows,

$T_1 = T_0 + 500(T_e + T_d) = 30 + 500(1 + 2.3e - 3) = 531.15\,\mathrm{s}$

$T = 4\,T_1 = 2124.6\,s = 0.59\,\mathrm{hour}$

At each location, the images are summed to improve the signal-to-noise (SNR) ratio. But this is not always a suitable thing to do due to sample drift (relative drift between the optics stage and sample stage). To overcome the limitation of sample drift only a subset of the measured 500 images are used. This subset contains sufficiently well correlated images. A minimum correlation coefficient can be chosen as 0.97 and the cross-correlation of all the images with one arbitrarily chosen image is calculated, and the largest contiguous block lying above 0.97 is selected. Typically, only $30 - 100$ among 500 images are suitable. Then phase retrieval algorithm is performed for this four locations with the summed up images. The resolution of the reconstructed image is limited by the SNR ratio of the measured diffraction patterns.

We can make some observations based on the above mentioned case,

- Typically, the experiments require much more than 4 probe locations. In case of scanning $1\,\mu m \times 1\,\mu m$ area with a 100 nm diameter probe, 50 nm horizontal step size, 50 nm vertical step size there would be 20×21 or 420 probe locations. In the case of 500 exposures with 1 sec exposure, the the total time required is almost 62 hours. Just to improve the SNR the experiment time required has increased by a huge margin.

  $T = 420(T_0 + n(T_e + T_d)) = 420(30 + 500(1 + 2.3e - 3)) \approx 62\,\mathrm{hours}$

- If the drift could be countered in real-time in a direct manner better image spatial resolution can be achieved from ptychography.

- If the drift could be countered in real-time and only one exposure at a location was required then it would save a lot of beamtime at APS. If we consider the same example, then instead of 62 hours, we would require only 3.6 hours to complete the experiment, which is 17 times faster.

  $T = 420(T_0 + n(T_e + T_d)) = 420(30 + 1(1 + 2.3e - 3)) \approx 3.6\,\mathrm{hours}$

- The overhead time $T_0 = 30$ secs is large and is slowing the whole scanning process down. If the overhead time T_0, required for stabilizing the probe at one position, could be reduced with the help of advanced control algorithm, better positioning system and better control hardware to 150 msec (in addition to only one exposure time),

then the total scan time would be 0.13 hour, which compared to 62 hours would be approximately 476 times faster.

$T = 420(T_0 + n(T_e + T_d)) = 420(150e-3 + 1(1 + 2.3e-3) \approx 0.13\,\text{hours}$

- The longer the duration of a ptychography experiment more relative drift between the optics stage and sample stage will occur resulting into erroneous diffraction data and eventually wrong reconstructed images. So, reducing the imaging time is important. Even a small error in the probe positions have a large effect on the reconstruction of the sample.

- APS-U will provide with brighter and higher energy X-rays with higher flux. This will require shorter exposure times to achieve same amount of information. Also this high dose of X-ray requires shorter exposure time to assure the structural integrity of the sample does not degrade during the experiment.

2.4 Impact of the Sensor Drift on X-ray Microscopy

To reconstruct high spatial resolution X-ray image of a sample the zone-plate focusing optics needs to be scanned with high-precision stages in closed-loop with controllers featuring large positioning bandwidth and high positioning resolution. These controllers acting on the optics stage in real-time directly reduces the open loop drift of the scanning stages, rejects any incoming environmental disturbances and attenuates measurement noise of the sensor. Above architecture works out perfectly when the assumption that the sensor is fixed with respect to the global reference frame. In reality, the sensor fixtures would move due to thermal expansion or contraction of the sensor fixtures. Thermal expansion or contraction happens due to the periodic temperature change in the experimental hutch at APS beamline.

2.5 Requirements of Different Scanning Techniques

The two main scanning techniques used in X-ray imaging are the step scan and the fly-scan. In step scan technique, to do a raster scan to cover a $1\,\mu m \times 1\,\mu m$ area on the sample, the optics stage is first given a command to move to position 1 on the first row of the raster. Then it is verified through measurement that the stage has indeed moved to the desired position 1, resulting in some time delay. At this point, the diffraction data starts getting recorded by the area photon detector for a predefined time ensuring the correct dose of photons. After

the data is recorded the detector requires a short gap during which it cannot record any more data. After this, the command to move to position 2 (one step right in the same row of the raster) is given. So, clearly the step scan requires significantly longer time due to different overheads involved. In addition, the step movement involves high frequency components like a square wave. This introduces a closed-loop tracking bandwidth requirement that can only be met by controllers with large -3 dB tracking bandwidth [1]. The controllers designed to give high 3σ positioning resolution have low -3 dB tracking bandwidth, and hence are not suitable for step scan technique. The X-ray images achieved in [1] are with large -3 dB tracking bandwidth controllers running on the optics scanning stages during a typical step scan routine. Fly-scan technique in short, requires the optics stages to be moved continuously all the while collecting the X-ray diffraction data at a predefined interval. Fly-scan would reduce the time to scan particular area by a huge margin. Depending on the type of reference trajectory high resolution controllers (suitable for low frequency component trajectory like spiral, circular) or high bandwidth controllers (suitable for high frequency component or high angle turn trajectories) would be chosen for a particular flyscan experiment.

CHAPTER 3

FAST AND ROBUST OPTIMAL CONTROL FOR VELOCIPROBE X-RAY MICROSCOPE

A team of engineers, physicists and scientists from APS and UIUC have taken up a challenge of designing and commissioning an X-ray microscope (the Velociprobe) that will provide an ultra-stable platform for X-ray imaging, will be capable of accommodating the APS-U X-rays with 100 times more flux, and produce ultra-high spatial resolution $2D$ and tomography X-ray images with large imaging bandwidth. Curt Preissner, principal mechanical engineer at APS, spearheaded the design of the Velociprobe X-ray microscope and its components. The resident scientists, physicists and engineers at APS are responsible for taking the Velociprobe Laboratory Directed Research and Development (LDRD) project forward through microscope design, X-ray imaging, beamline systems and operations, and numerous other efforts. For the Velociprobe X-ray microscope to produce ultra-high quality X-ray images, one additional key component was high-bandwidth high-precision robust control, which is the where the expertise in controls in Scanning Probe Microscopy (SPM) from UIUC comes into the picture.

The goal of the Velociprobe X-ray microscope, as a LDRD project, was to scan $1\,\mu m \times 1\,\mu m$ area on the sample in less than 10 seconds and achieve X-ray diffraction images with around 10 nm spatial resolution. Here, scanning encompasses the time to move the focused X-ray spot on the sample along a predefined trajectory while diffraction patterns are being recorded at the area detector downstream.

The pre-Velociprobe era state-of-the-art at APS, with other X-ray microscopes was approximately 17 minutes to scan a $1\,\mu m \times 1\,\mu m$ area on the sample through step scan technique. The fine scanning optics stages was used to scan in open loop and with PID controllers. Although no detailed and methodical study about controls exits in the literature.

In this chapter, we will detail the achievements with Velociprobe X-ray microscope at APS from control design standpoint. Particularly the performance of the high-precision optics scanning stages utilizing the fast and robust optimal control will be studied. In Section 3.1 details about the Velociprobe X-ray microscope are provided; divided into device

description, system setup, system identification, and model verification. Section 3.2 explains the control design for the Velociprobe fine scanning optics stages. We will study the PID control algorithm (predominantly used in the industry) and robust H_∞ control design (well proven in the SPM field) and compare the results and showcase the achievements. Section 3.3 will show the end product of the Velociprobe X-ray microscope, the X-ray images. We will summarize the impact of the work done in this chapter on X-ray microscopy in the last Section 3.4.

3.1 Velociprobe X-ray Microscope

In this section, details of the Velociprobe X-ray microscope are explained in terms of design choices, limitations and the challenges on X-ray imaging for such a microscope.

3.1.1 Device Description

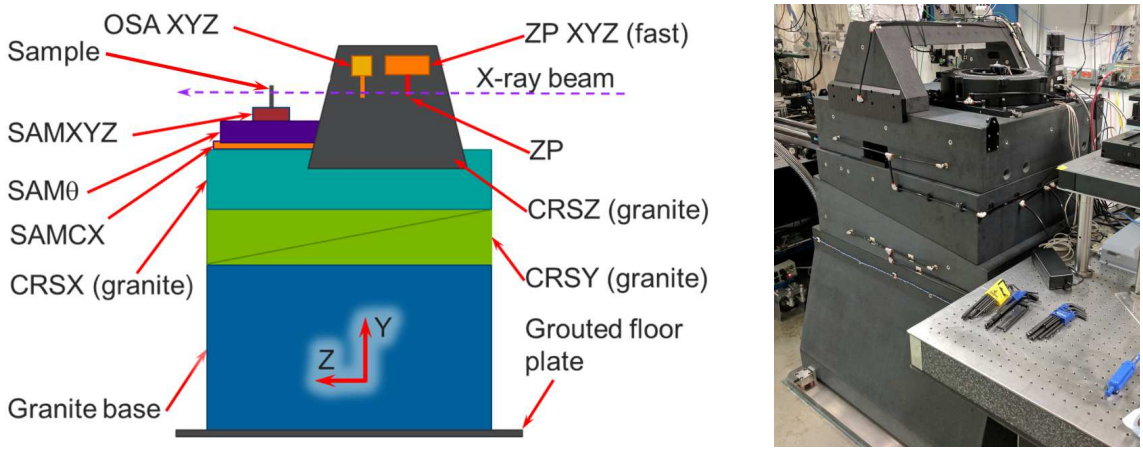

(a) (b)

Figure 3.1: (a) Schematic of the Velociprobe X-ray microscope. The coarse stages are made of large granite blocks which are given motion utilizing state-of-the-art air bearing. The fine positioning zone plate XYZ stages, attached to the top granite gantry in an inverted orientation, is used to do high precision scanning of the focused X-ray spot to cover a target area on the sample. (b) The installed instrument at APS Sector 2 beamline.

The Velociprobe (Figure 3.1) is a next-generation X-ray microscope which is built at APS (ANL) to enable ultra-high resolution X-ray imaging in a ultra-stable microscope platform and to complement the APS-U. It consists of a novel in-house coarse positioning stage, a

state-of-the-art commercially available optics scanning nanopositioning stages ($ZP\,XYZ$), sample coarse positioning stages ($SAM\,XYZ$), and sample rotation stages ($SAM\,\theta$). The coarse positioning stages are made of granite, which provides coarse motion utilizing state-of-the-art air bearing on granite. During X-ray imaging the coarse positioning granite stages remain static and the air bearing that is supporting the granite blocks are turned off. This makes the granite base, coarse positioning Y stages ($CRSY$), coarse positioning X stages ($CRSX$), and coarse Z positioning granite gantry ($CRSZ$) on top, act as one granite block. This results into good isolation from the environmental disturbance and provides with a ultra-stable platform for X-ray science. The zone plate optics scanning stage assembly ($ZP\,XYZ$) is attached to the top gantry in an inverted manner to satisfy the working distance constraint between the zone plate optics and the sample. The coarse rotation stage ($SAM\,\theta$) provides rotation to the sample during scanning required for X-ray tomography experiments.

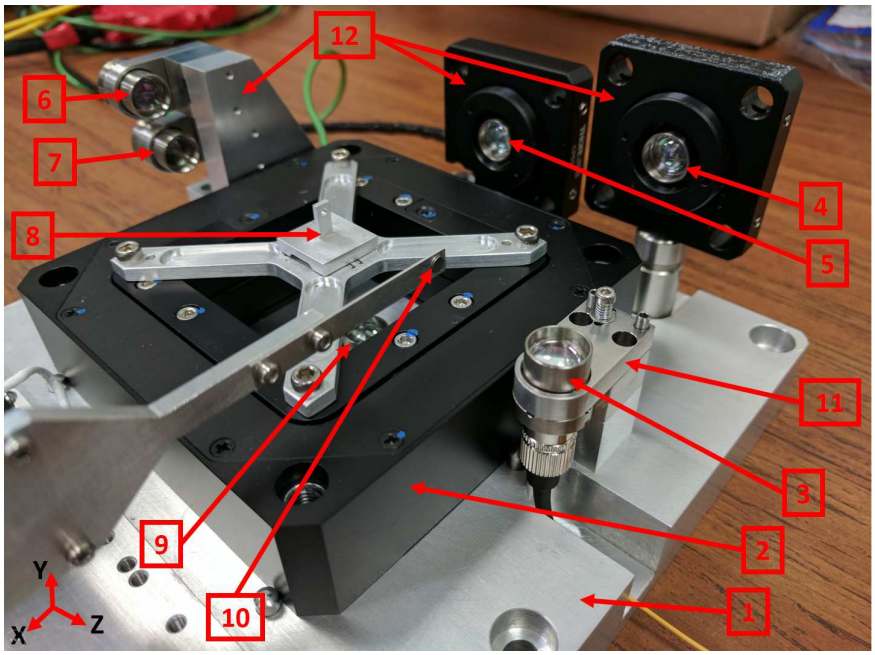

Figure 3.2: Velociprobe fine scanning optics stage assembly on a table, before the final assembly in an inverted orientation under the granite gantry shown in Figure 3.1. In details, 1 = reference frame, 2 = PI parallel kinematics XYZ nanopositioning stages, 3 = sensor head sample Y axis, 4 = sensor head sample X axis, 5 = sensor head optics X axis, 6 = sensor head sample Z axis, 7 = sensor head optics Z axis, 8 = zone plate optics kinematic holder, 9 = sensor head optics Y axis, 10 = order sorting aperture, and 11 and 12 = Aluminum alloy fixtures that hold the sensors.

Figure 3.2 shows the fine positioning optics stage assembly ($ZP\,XYZ$) of the Velociprobe X-ray microscope on a table setup, before being assembled on to the Velociprobe granite stages (shown in Figure 3.1) at the APS beamline. The main component of the optics stage

assembly is the Physik Instrumente (PI) 3DOF XYZ nanopositioning stage, which carries the zone plate focusing optics attached to the zone plate holder, is bolted to the Aluminum alloy reference frame. The displacement of the XYZ nanopositioning optics stages are measured by high-precision Attocube Laser interferometric sensors. Mirrors (not shown in the figure) are glued on the zone plate holder, so that the laser coming out of the standard Attocube focusing sensor heads can reflect back to the sensor heads. The displacement of the sample coarse positioning stages SAM XYZ (Figure 3.1) are also measured with separate 3 channels of the same Attocube interferometric sensors. All the interferometric sensor heads, that are being used for optics and sample stage displacement measurement, are attached to the reference frame with suitable sensor fixtures. The sensors fixtures used to hold the sensor heads are made with Aluminum alloys.

3.1.2 System Setup

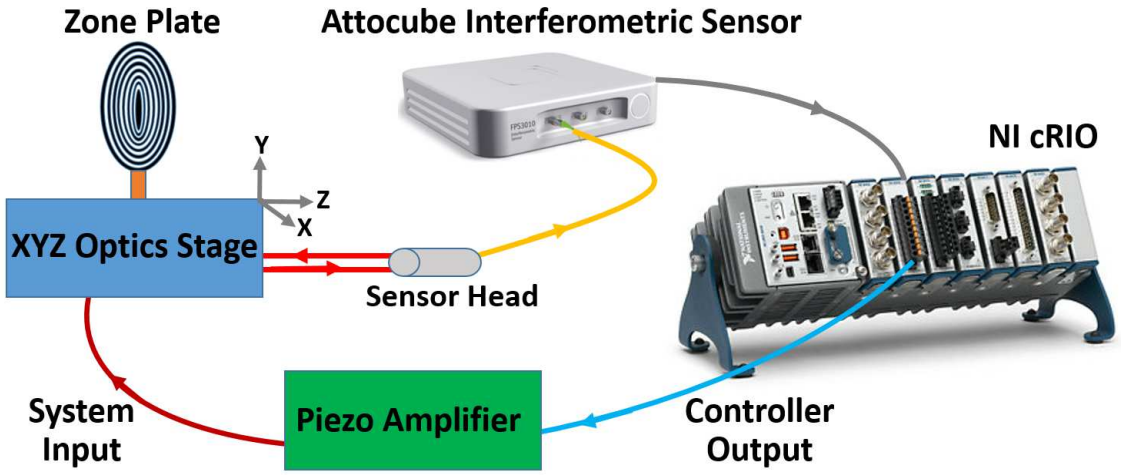

Figure 3.3: Velociprobe closed-loop system layout for the optics scanning stages. The sample stages are not shown here.

The Velociprobe X-ray microscope optics fine scanning stage closed-loop control system is comprised of PI XYZ fine scanning stages, National Instruments (NI) control hardware, and Attocube Laser interferometric displacement sensors (Figure 3.3). The NI control hardware includes NI cRIO-9039 real-time controller with Kintex-7 325T FPGA built into the chassis, NI-9402 digital input-output (DIO) modules, and NI-9263 analog voltage output modules. The zone plate optics XYZ stage displacement are measured by high resolution Attocube Laser interferometric sensors. Total three sets of quadrature signals representing the position information along each stage axes are generated by the Attocube sensor box. These are

then read through the NI-9402 DIO modules directly into the Kintex-7 FPGA in the NI cRIO chassis. The reference trajectory generation, processing stage displacement information sourcing from the Attocube sensors, running discrete feedback controller algorithm based on tracking error are done in the FPGA at 25 kHz sampling rate. The controller output voltage is provided by the NI-9263 analog output module. This voltage signal is amplified through a predefined scaling factor in the PI amplifier designed to work with the PI XYZ optics scanning stages. The amplified voltage signal goes to the piezo actuators of the PI XYZ stages and actuates the stages to move to commanded position in the three-dimensional Euclidean space. This is the closed-loop system for the optics scanning stages. The direct control of sample coarse positioning XYZ stages is not a part of this work and hence will not be explained here. The sample stages are only moved using Delta-Tau PMAC system for aligning the sample and optics with the X-ray beam before the scanning operation.

3.1.3 System Identification

The PI parallel kinematics fine positioning XYZ stages are too complex to model using the first principles (physical modeling). So we used frequency-response based identification to model the stage dynamics, where at each operating point, a transfer function was fit to the input-output experimental data. More specifically, the response (as determined from Attocube sensor measurement) of each stage to an input of band-limited white noise ($0 - 12$ kHz, 5 nm amplitude) was acquired, and a frequency response function (FRF) was estimated from the input-output time-domain data. The frequency components of the input band-limited white noise signal included our frequency range of interest ($0-1$ kHz) plus additional bandwidth beyond the operational frequency range of the device, such that any out-of-range dynamics that contribute to in-range response could be revealed. We chose band-limited uniform white noise so as not to excite the PI XYZ stages with any higher frequency components. High frequency content given as an input to the stages can excite non-linearities and high frequency modes of the system and potentially damage it. Also the excitation energy in the band of interest ($0 - 1$ kHz in this case) gets reduced in case of a full spectrum white noise signal. The amplitude of the white noise is chosen to be a small value so as not to over excite the stages at their respective natural frequencies. The stages are excited for over 6 minutes at 25 kHz rate while simultaneously collecting the stage input-output data during each identification experiment. A transfer function estimate calculation was performed on the experimental time-domain input-output data by Welch's method ([35] and Appendix B) to generate a non-parametric model. To obtain a parametric transfer function model a curve fitting was done on the non-parametric model. Verification of the obtained

model is performed to make sure that it represents the actual dynamics of the PI XYZ stages properly.

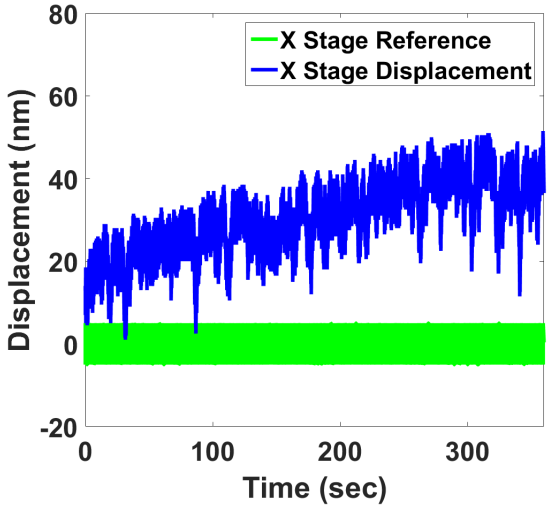

Figure 3.4: Band-limited uniform white noise with 5 nm amplitude is given as input to the X-stage. The resulting stage displacement is measured and used for fitting a model.

To assess nonlinear behavior of the PI XYZ stages we studied the differences in the frequency responses estimated at various operating points (DC offsets). Note that for an ideal linear system, the frequency response data would be independent of the operating point. Accordingly, frequency response functions were obtained for multiple X-stage DC offsets (-6000, 0, and 6000 nm), Y-stage DC offsets (-2000, 0, and 2000 nm) and Z-stage DC offsets (-6000, 0, and 6000 nm), respectively, for a total of 9 measurements for each stage. The resulting 9 transfer function estimate calculations or experimental Frequency Response Functions (FRFs) for XX-stage (fit between X-stage input signal and X-stage output signal) for the 9 different operating points are shown in the Figure 3.5a. Small variations mainly in the high frequencies are observed for the XX-stage. Figure 3.5b and Figure 3.5c shows similar sets of 9 transfer function estimate calculations for YY-stage and ZZ-stage, respectively, with variations observed in high frequency region. From these plots, we conclude that the X , Y and Z stage dynamics could be well approximated by linear models, with the variations being viewed as a perturbations of the nominal linear models. The linear control design methodology will account for the perturbed linear models by incorporating feedback laws with high gains from low frequencies up to bandwidth, making the system insensitive to variations in the plant in these frequencies.

After estimating the FRFs at each operating point, the average of all of the 9 FRFs were calculated for each of the XX, YY, and ZZ stages. Figure 3.6a shows the averaged non-parametric transfer function for XX-stage calculated from 9 different FRFs shown previously.

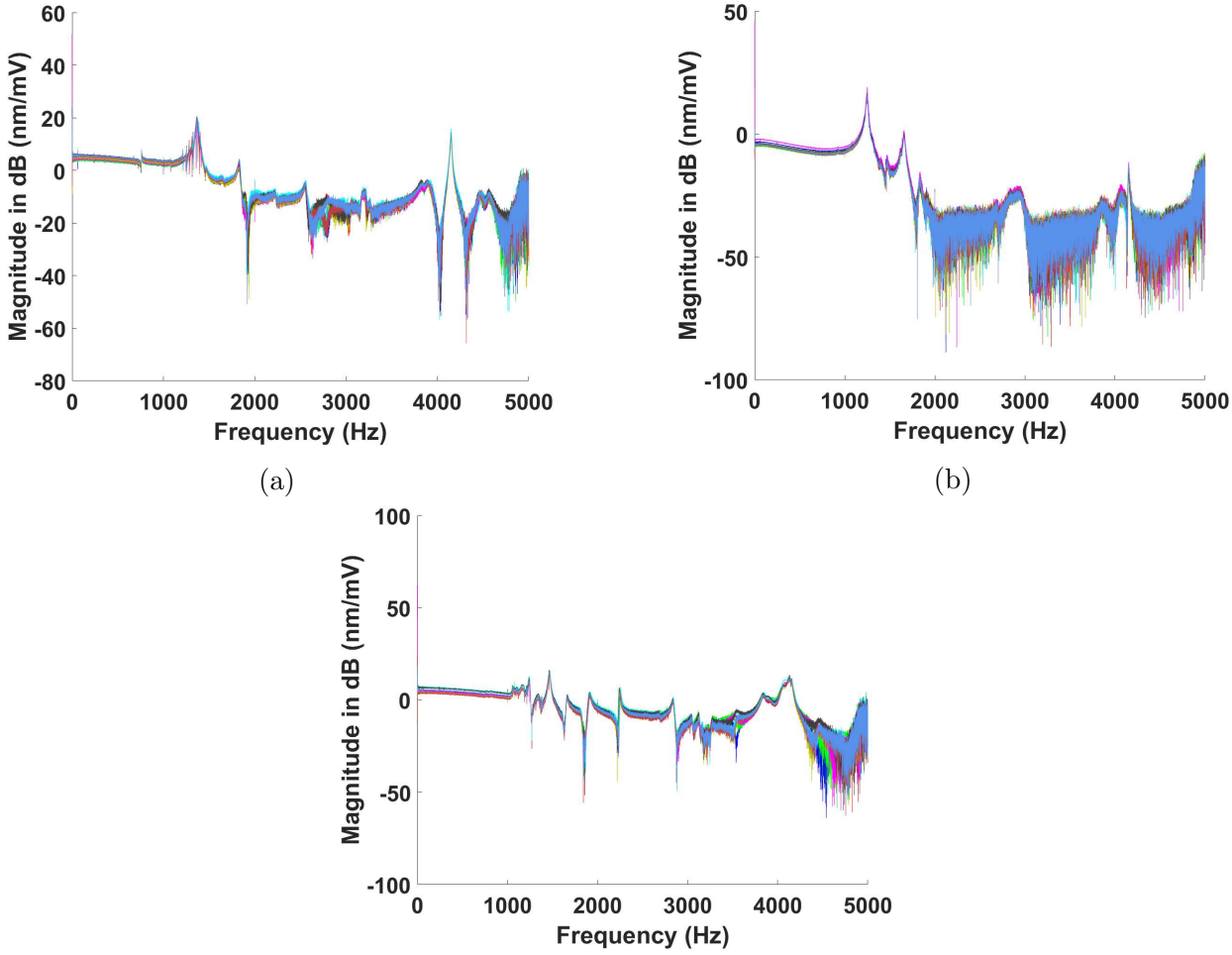

Figure 3.5: 9 different non-parametric transfer function estimates calculated by Welch's method for (a) XX-stage identification, (b) YY-stage identification, and (c) ZZ-stage identification. Here, XX-stage means a model between X-stage input signal and X-stage output signal.

The similar averaged transfer functions for YY-stage and ZZ-stage are shown in Figure 3.6b and Figure 3.6c, respectively. The averaged transfer function estimate calculations are noisy only in very high frequencies, which is beneficial from point of view fitting a parametric model to this calculation.

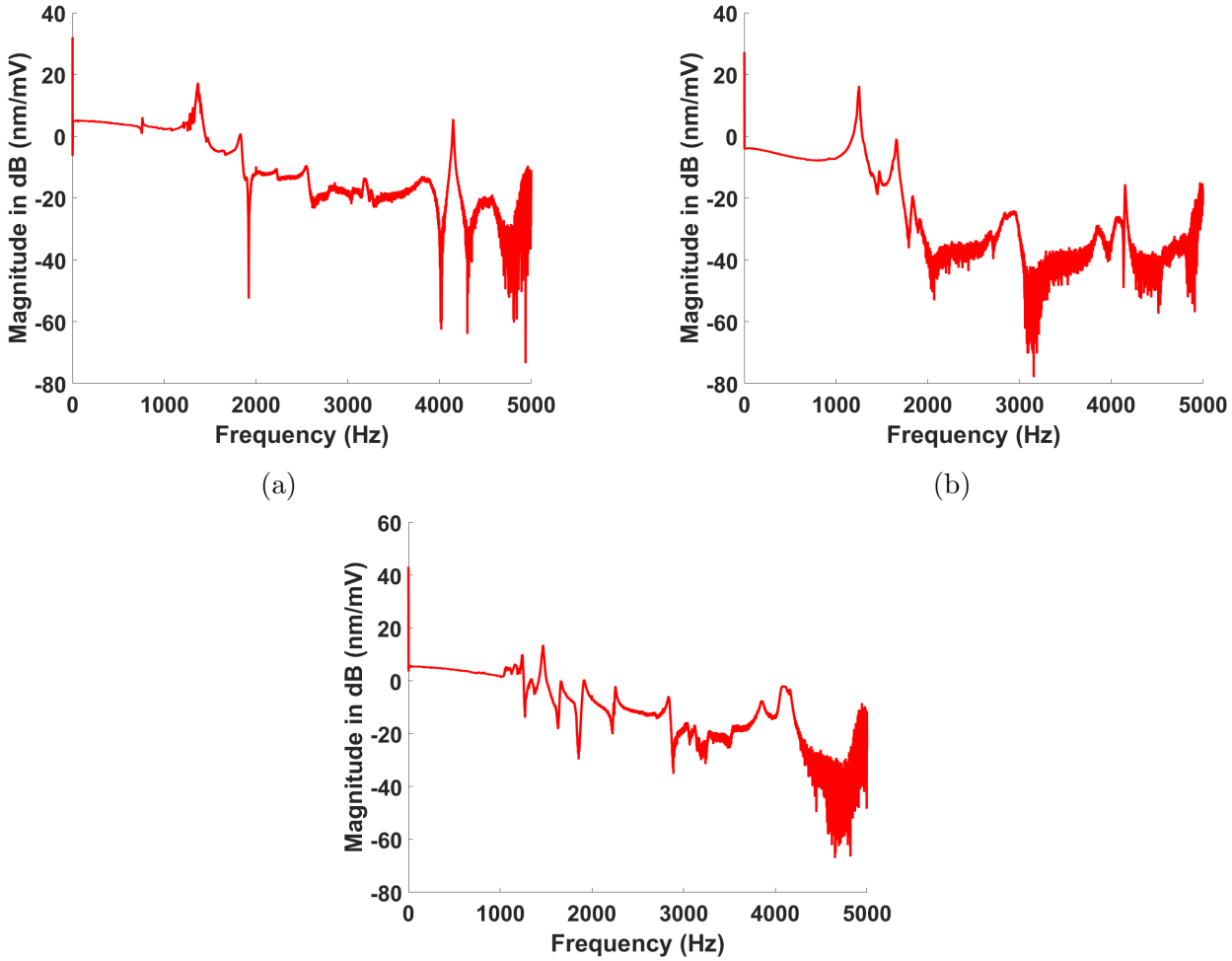

Figure 3.6: Averaged non-parametric transfer function from 9 different transfer function estimates for (a) XX-stage, (b) YY-stage, and (c) ZZ-stage.

3.1.4 Model Fitting

The averaged transfer function estimate calculations (non-parametric models) of the experimental frequency response of XX, YY, and ZZ stages of the Velociprobe optics scanner was shown in the previous section. A parametric model is fitted to each of the three non-parametric models using a curve-fitting process. The parameters of these fitted models are

used to generate transfer function models G_{xx}, G_{yy}, and G_{zz} of the XX, YY, and ZZ stages, respectively.

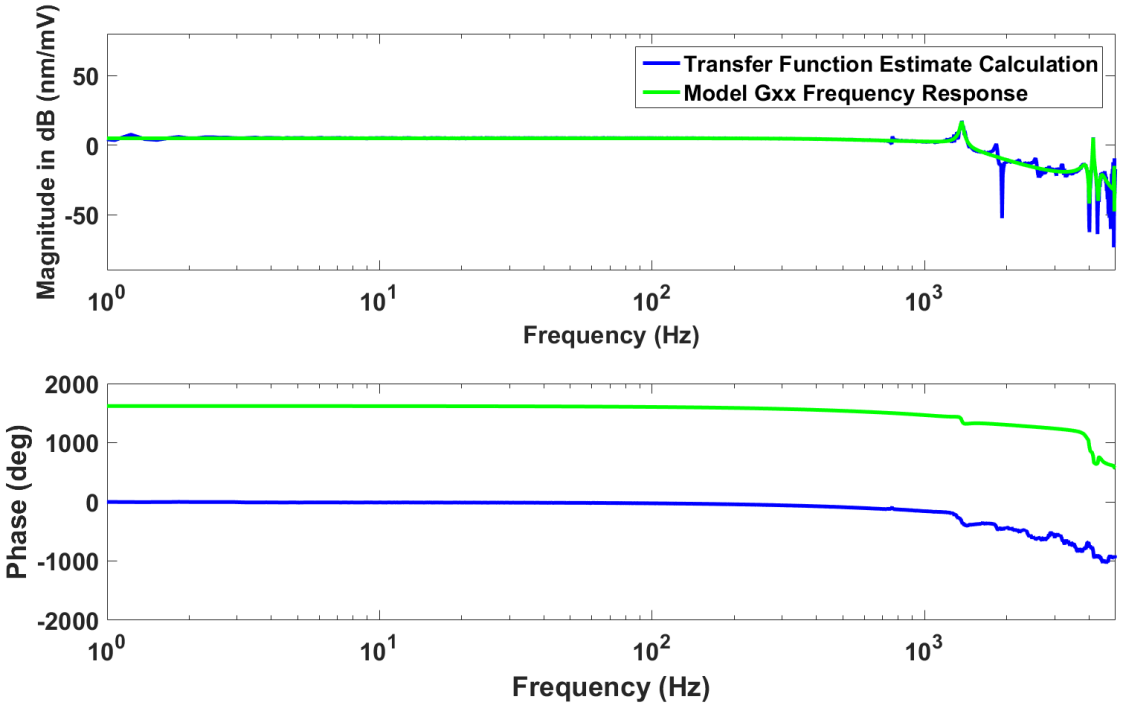

Figure 3.7: Comparison between the averaged transfer function estimate calculation of the experimental FRF of XX-stage and the frequency response of the 15^{th} order fitted model G_{xx}.

Figure 3.7 shows the comparison between the transfer function estimate calculation for XX-stage experimental FRF and the FRF of the 15^{th} order fitted model G_{xx}. The model G_{xx} captures the dynamics of the experimental transfer function estimate as the significant peaks. The first resonant peak (or the open loop bandwidth) of the XX-stage model G_{xx} is at 1.3 kHz. Some insignificant peaks in the higher frequency region are not captured by the model. We are interested in the XX-stage model behavior to closely approximate experimental FRF in the frequency range 0 to 1.5 kHz (for control implementation), and to have a general similar trend in the higher frequencies. The stages will not be operated over the open loop bandwidth during scanning. The transfer function of the 15^{th} order model G_{xx} of the optics scanning XX-stage is given in Equation 3.1.

$$G_{xx} = \frac{num\ G_{xx}}{den\ G_{xx}} \tag{3.1}$$

$$\begin{aligned} num\ G_{xx} &= -1.643e07(s+4972)(s^2+1395s+7.638e7)(s^2-3.783e4s+4.916e8) \\ &\quad (s^2-65.23s+6.362e8)(s^2+151.5s+7.38e8)(s^2-3.146s+9.712e8) \\ &\quad (s^2-1.318e4s+1.046e9) \\ den\ G_{xx} &= (s+3.658e4)(s^2+6751s+1.466e7)(s^2+6092s+6.811e7) \\ &\quad (s^2+183.5s+7.373e7)(s^2+1116s+6.035e8)(s^2+71.89s+6.796e8) \\ &\quad (s^2+1259s+7.751e8)(s^2+2.247s+9.706e8) \end{aligned}$$

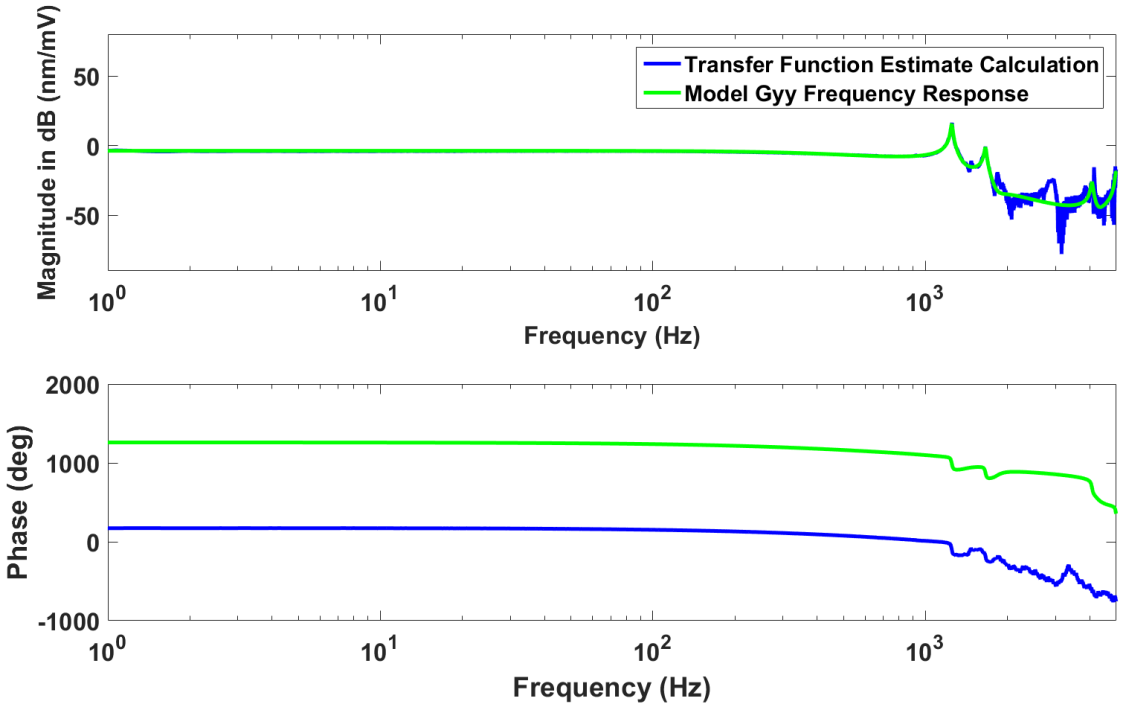

Figure 3.8: Comparison between the averaged transfer function estimate calculation of the experimental FRF of YY-stage and the frequency response of the 13^{th} order fitted model G_{yy}.

Similarly, Figure 3.8 shows the comparison between the averaged transfer function estimate calculation for YY-stage experimental FRF and the FRF of the 13^{th} order fitted model G_{yy}. The model G_{yy} captures the dynamics of the averaged experimental FRF quiet well, with the first resonant peak of the YY-stage model G_{yy} being at 1.2 kHz. Some high frequency peaks are not fitted by the model. We are interested in the YY-stage model behavior to closely approximate experimental FRF in the frequency range 0 to 1.5 kHz (for control

implementation), and to have a general similar trend in the higher frequencies. The stages will not be operated over the open loop bandwidth during scanning. The transfer function of the 13^{th} order model G_{yy} is given in Appendix B.

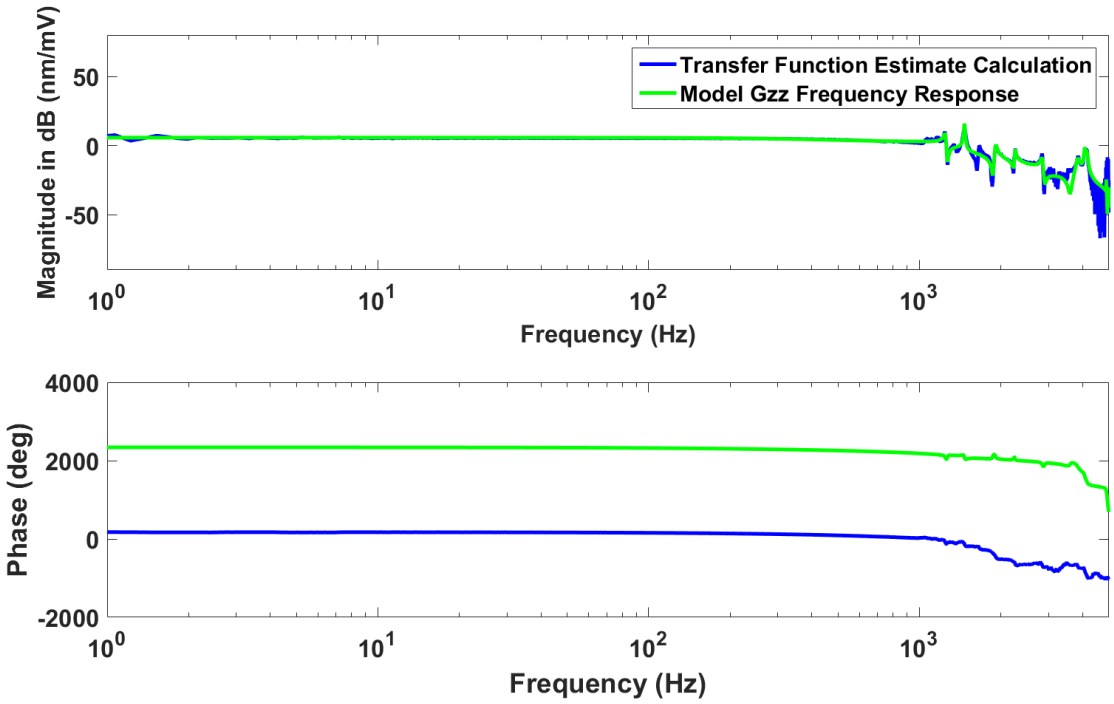

Figure 3.9: Comparison between the averaged transfer function estimate calculation of the experimental FRF of ZZ-stage and the frequency response of the 33^{rd} order fitted model G_{zz}.

In case of ZZ-stage the comparison between the transfer function estimate calculation for experimental FRF and the FRF of the 33^{rd} order fitted model G_{zz} is shown in the Figure 3.9. The model G_{zz} captures the dynamics of the experimental transfer function estimate quiet well. The first resonant peak of the model G_{zz} is 1.2 kHz. Similar to before we are interested in the ZZ-stage model behavior to closely approximate experimental FRF in the frequency range 0 to 1.5 kHz. We will not perform any high bandwidth motion along the Z-direction. The transfer function of the 33^{rd} order model G_{zz} is given in Appendix B.

3.1.5 Balanced Realization and Model Reduction

A state space realization that has its controllability and observability grammians equal and diagonal, is called a balanced realization [38]. It can be assumed that the optics fine scanning XX stage plant G_{xx} has a state space realization of (A, B, C, D). This state-space realization is called a minimal realization if (C, A) is observable and (A, B) is controllable. Minimal realization is the lowest order realization possible for a given system. The A matrix of the minimal realization is Hurwitz. To obtain a balance realization of a system, it is usual practice to start with the minimal realization of the system and apply a certain state transformation. When the system is balanced the controllability and the observability ellipsoids are exactly aligned. Thus the states which are most controllable are also most observable. Balance realization usually comes as a precursor step of model reduction.

In the model reduction step the states that are most controllable and most observable are preserved, while the least observable and controllable states are eliminated. Through balance realization the Hankel singular values are oriented from large to small, with the interpretation that the states corresponding to large Hankel singular values are strongly controllable and observable. So, by balanced truncation technique the states with small Hankel singular values are truncated. While following this process of model reduction it is important to keep the system input-output properties approximately same.

In particular, XX-stage model G_{xx} was not reduced below 15^{th} order. The YY-stage 13^{th} order model G_{yy} was reduced through balanced truncation to 12^{th} order reduced model rG_{yy}, with the transfer function given in Appendix B. Figure 3.10 shows the comparison between the transfer function estimate of the experimental FRF for YY-stage, the frequency response of the 13^{th} order model G_{yy} and the frequency response of the reduced YY-stage model rG_{yy}. The reduced order model matches the frequency response in magnitude and phase quiet well. The ZZ-stage 33^{rd} order model G_{zz} was reduced through balanced truncation to 28^{th} order reduced model rG_{zz}. Figure 3.11 shows the comparison between the transfer function estimate of the experimental FRF for ZZ-stage, the frequency response of the 13^{th} order model G_{zz} and the frequency response of the reduced ZZ-stage model rG_{zz}. The reduced order model matches the frequency response in magnitude and phase well. The model rG_{zz} is given in the Appendix B.

The XX-stage model G_{xx} poles and zeros are given in the Table 3.1. All poles are in the left-half plane (LHP), which makes the model G_{xx} a stable plant. There are six right-half plane (RHP) zeros (non-minimum phase zeros) of model G_{xx} which influences the system behavior, controller design, and closed-loop bandwidth [39]. Since, controllers are designed

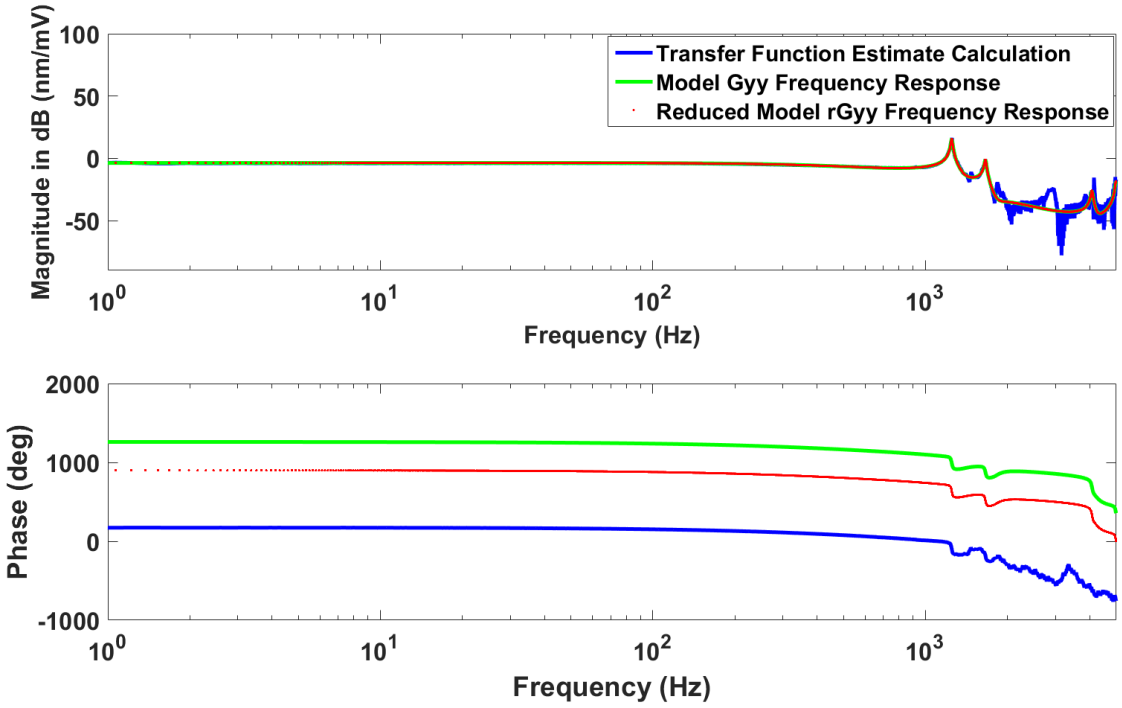

Figure 3.10: Comparison between the transfer function estimate calculation of the experimental FRF of YY-stage, the frequency response of the fitted 13^{th} order model, and frequency response of the reduced fitted 12^{th} order model.

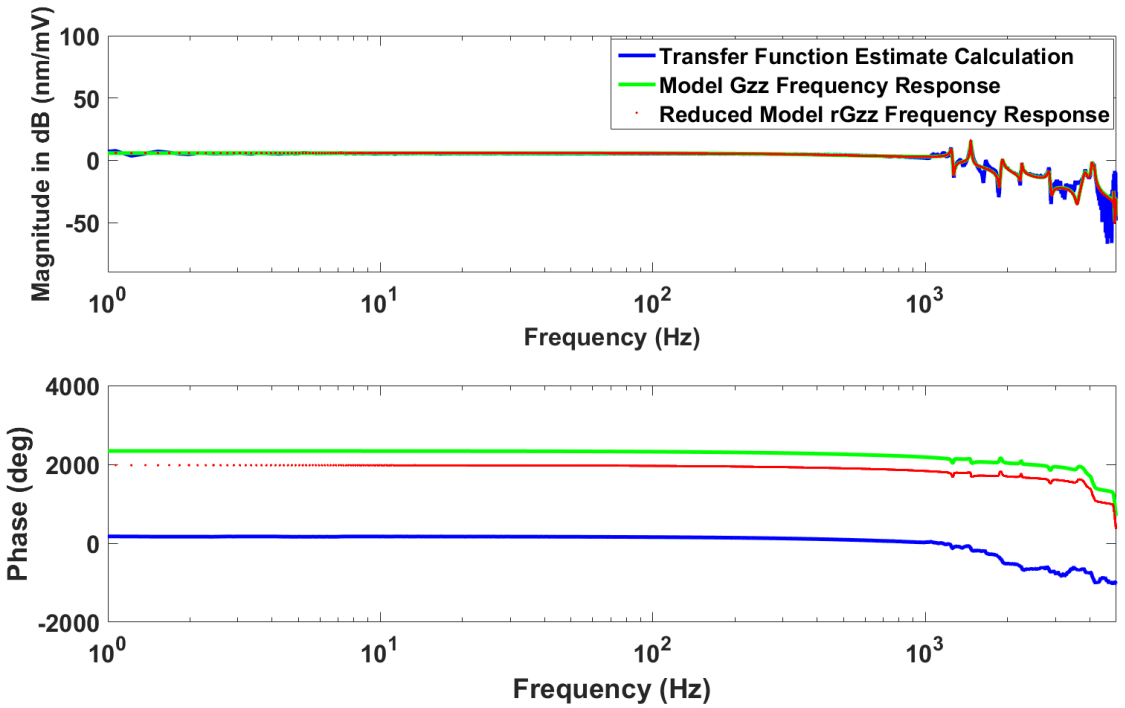

Figure 3.11: Comparison between the transfer function estimate calculation of the experimental FRF of ZZ-stage, the frequency response of the fitted 33^{rd} order model, and frequency response of the reduced fitted 28^{th} order model.

based on these experimentally identified stage models, these zeros are present in the closed-loop sensitivity transfer function S. These zeros influence the shape of the S transfer function and makes it hard to achieve large tracking bandwidth. For Velociprobe optics stages the open loop bandwidth is over 1 kHz. But due to presence of RHP zeros the achievable closed-loop bandwidth was just over 200 Hz. This limitation was observed for the previous EUI X-ray microscope optics scanning stages as well [12].

Table 3.1: Poles and Zeros of Velociprobe Optics XX-stage model G_{xx}

Poles	Zeros
-36575 + 0i	18915 + 11571i
-1.1234 + 31155i	18915 - 11571i
-1.1234 - 31155i	6590.3 + 31666i
-629.6 + 27833i	6590.3 - 31666i
-629.6 - 27833i	1.573 + 31164i
-35.944 + 26069i	1.573 - 31164i
-35.944 - 26069i	-75.747 + 27166i
-558.02 + 24560i	-75.747 - 27166i
-558.02 - 24560i	32.614 + 25223i
-91.743 + 8586.3i	32.614 - 25223i
-91.743 - 8586.3i	-697.48 + 8711.8i
-3046 + 7670i	-697.48 - 8711.8i
-3046 - 7670i	-4971.5 + 0i
-3375.5 + 1807i	
-3375.5 - 1807i	

The RHP zeros causes a number of performance limitations. According to classical root-locus analysis, when the feedback gain is increased towards infinity then the closed-loop poles migrate towards the position of the open-loop zeros. So, even with a stable plant (all poles in LHP), the closed-loop poles might migrate from LHP to the open-loop RHP zeros, making the closed-loop unstable. According to [39], for a real RHP zero z the approximate requirement for bandwidth is,

$$\omega_b < z/2$$

and the requirement for a complex-pair of RHP zeros z is,

$$\omega_b < \begin{cases} |z|/4 & : Re(z) \gg Im(z) \\ |z|/2.8 & : Re(z) = Im(z) \\ |z| & : Re(z) \ll Im(z) \end{cases}$$

In case of Velociprobe optics XX-stage model G_{xx} the upper bound over the closed-loop bandwidth due to the complex pair of RHP zeros are 882, 5147, and 4960 Hz. So, closed-loop bandwidth cannot be more than 882 Hz. This is less than the open loop bandwidth (1.3 kHz) and will act as a limitation.

$$for\ z_1, z_2 : \omega_b < |18915 + 11571i|/4 = 5543\, rad/s\ (882Hz) \tag{3.2}$$

$$for\ z_3, z_4 : \omega_b < |6590.3 + 31666i| = 32345\, rad/s\ (5147Hz) \tag{3.3}$$

$$for\ z_5, z_6 : \omega_b < |1.573 + 31164i| = 31164\, rad/s\ (4960Hz) \tag{3.4}$$

Table 3.2: Poles and Zeros of Velociprobe Optics YY-stage Reduced model rG_{yy}

Poles	Zeros
-175.4 + 31392i	25376 + 0i
-175.4 - 31392i	-21527 + 0i
-195.48 + 25653i	11925 + 21264i
-195.48 - 25653i	11925 - 21264i
-3511.8 + 879.67i	1218 + 26705i
-3511.8 - 879.67i	1218 - 26705i
-78.861 + 10427i	-660.64 + 11443i
-78.861 - 10427i	-660.64 - 11443i
-52.515 + 7842.7i	-856.59 + 8671.1i
-52.515 - 7842.7i	-856.59 - 8671.1i
-2307.6 + 8047.1i	
-2307.6 - 8047.1i	

The reduced YY-stage model rG_{yy} poles and zeros are given in the Table 3.2. rG_{yy} is a stable model with all LHP poles. There are five non-minimum phase zeros. The real RHP zero $z_1 = 25376$ results in the upper-bound $\omega_b < 12688$ rad/s (2019 Hz) for the closed-loop bandwidth. Similarly, for the complex pair of RHP zeros the upper bound on closed loop bandwidth is 3.8 kHz. So, for YY-stage upper bound on closed loop bandwidth is 2 kHz which does not pose any limitation due the open loop bandwidth being 1.2 kHz.

$$for\, z_3, z_4 : \omega_b < |11925 + 21264i| = 24380\, rad/s\ (3880Hz) \tag{3.5}$$

$$for\, z_5, z_6 : \omega_b < |1218 + 26705i| = 26733\, rad/s\ (4254Hz) \tag{3.6}$$

The reduced ZZ-stage model rG_{zz} poles and zeros are given in the Table 3.3. The model is stable with all LHP poles. There are nine non-minimum phase zeros. The real RHP

zero $z_3 = 18540$ results in the upper-bound $\omega_b < 9270$ rad/s (1475 Hz) on the closed-loop bandwidth. The complex pair of RHP zeros pose an upper bound of 4 kHz on the closed-loop bandwidth, which does not create any limitations on achievable bandwidth.

$$for\, z_4, z_5 : \omega_b < |5.8909 + 31328i| = 31328 rad/s\ (4986 Hz) \tag{3.7}$$

$$for\, z_6, z_7 : \omega_b < |22.441 + 31060i| = 31060 rad/s\ (4943 Hz) \tag{3.8}$$

$$for\, z_8, z_9 : \omega_b < |24.397 + 30764i| = 30764 rad/s\ (4896 Hz) \tag{3.9}$$

$$for\, z_{10}, z_{11} : \omega_b < |5337.8 + 24868i| = 25434 rad/s\ (4048 Hz) \tag{3.10}$$

Table 3.3: Poles and Zeros of Velociprobe optics scanning ZZ-stage reduced model rG_{zz}

Poles	Poles	Zeros	Zeros
-17286 + 0i	-2095.6 - 22646i	-1.965e+06 + 0i	833.87 - 25368i
-33.556 + 31319i	-145.17 + 17854i	-34256 + 0i	-233.76 + 22635i
-33.556 - 31319i	-145.17 - 17854i	18540 + 0i	-233.76 - 22635i
-149.73 + 31172i	-3358.1 + 0i	5.8909 + 31328i	-135.26 + 18214i
-149.73 - 31172i	-3041.5 + 7889i	5.8909 - 31328i	-135.26 - 18214i
-8.1725 + 30765i	-3041.5 - 7889i	22.441 + 31060i	-92.1 + 14027i
-8.1725 - 30765i	-29.105 + 9211.3i	22.441 - 31060i	-92.1 - 14027i
-184.87 + 26098i	-29.105 - 9211.3i	24.397 + 30764i	-59.93 + 11725i
-184.87 - 26098i	-60.91 + 7835.5i	24.397 - 30764i	-59.93 - 11725i
-135.49 + 25623i	-60.91 - 7835.5i	5337.8 + 24868i	-33.541 + 7965.9i
-135.49 - 25623i	-101.86 + 11995i	5337.8 - 24868i	-33.541 - 7965.9i
-352.83 + 24155i	-101.86 - 11995i	-633.67 + 25885i	-253.38 + 9260.7i
-352.83 - 24155i	-63.983 + 14162i	-633.67 - 25885i	-253.38 - 9260.7i
-2095.6 + 22646i	-63.983 - 14162i	833.87 + 25368i	

3.1.6 Model Verification

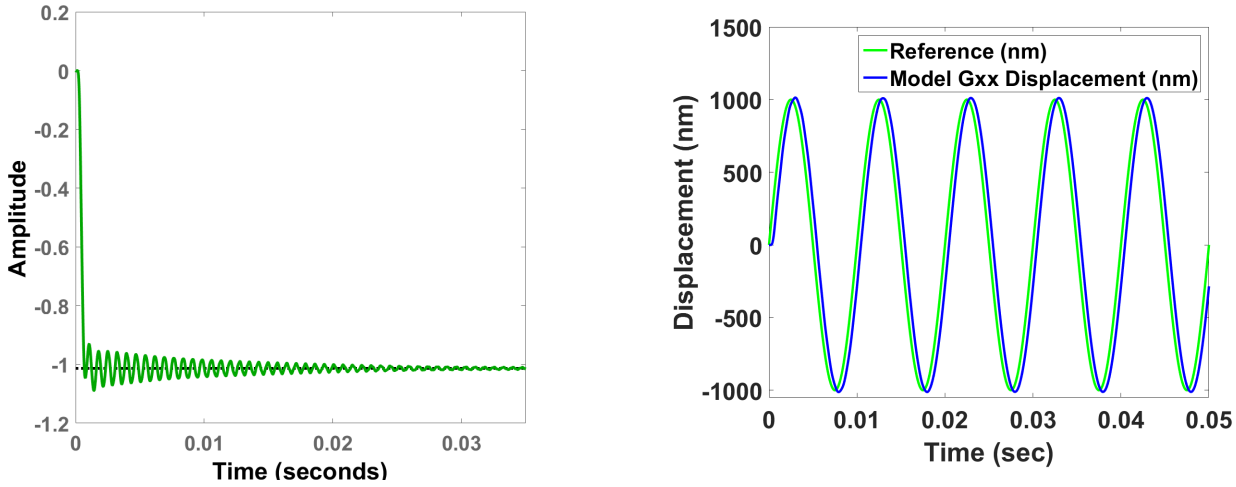

(a) (b)

Figure 3.12: (a) Open loop step response of fitted model G_{xx}, and (b) Open loop tracking of sine wave with amplitude 1000 nm and frequency 100 Hz by the fitted model G_{xx}.

The step response of the XX-stage model G_{xx} is shown in the Figure 3.12a. The optics XX-stage sensitivity is 1.7378 nm/mV, which means for 1 mV input to the X piezo-stack actuator the stage undergoes a displacement of 1.7378 nm. As a qualitative measure of the fit G_{xx} tracking of a sine wave with 1000 nm amplitude and frequency of 100 Hz is shown in Figure 3.12b.

Similarly, the YY-stage reduced fitted model rG_{yy} step response is shown in the Figure 3.13a. The optics YY-stage sensitivity is 0.6528 nm/mV, which means for 1 mV input to the Y piezo-stack actuator the stage undergoes a displacement of 0.6528 nm. As a qualitative measure of the fit tracking of a sine wave of 1000 nm amplitude and frequency of 100 Hz is shown in the Figure 3.13b.

The step response of the ZZ-stage reduced model rG_{zz} is shown in the Figure 3.14a. The optics ZZ-stage sensitivity is 1.9407 nm/mV, which means for 1 mV input to the Z piezo-stack actuator the stage undergoes a displacement of 1.9407 nm. As a qualitative measure of the fit tracking of a sine wave of 1000 nm amplitude and frequency of 100 Hz is shown in the Figure 3.14b.

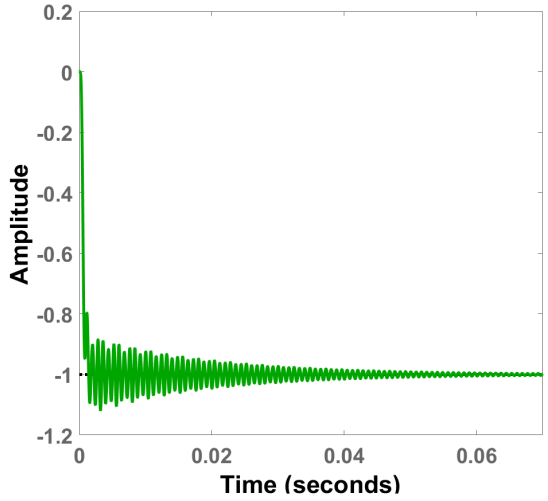

(a)

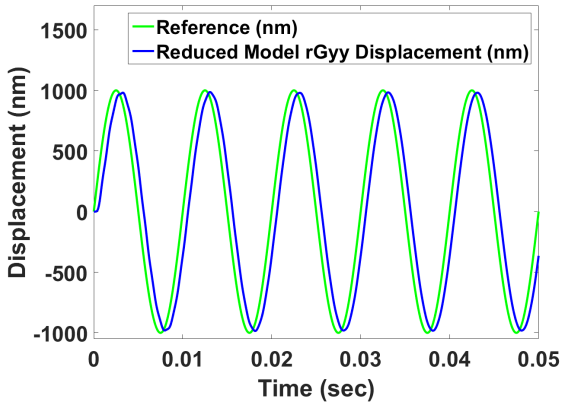

(b)

Figure 3.13: (a) Open loop step response of reduced model rG_{yy}, and (b) open loop tracking of sine wave with amplitude 1000 nm and frequency 100 Hz by the reduced model rG_{yy}.

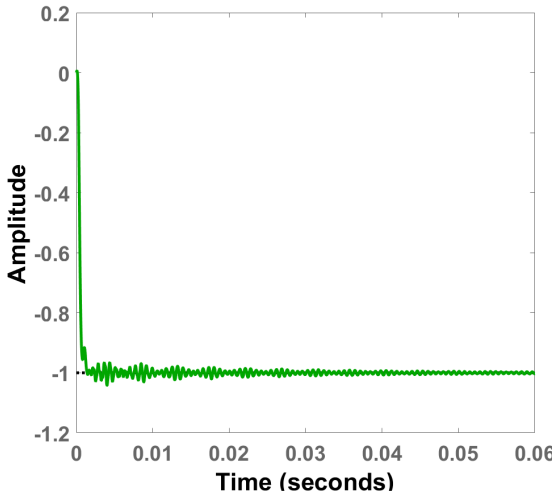

(a)

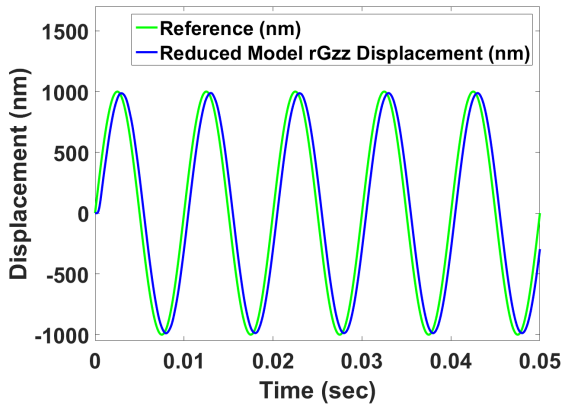

(b)

Figure 3.14: (a) Open loop step response of reduced model rG_{zz}, and (b) Open loop tracking of sine wave with amplitude 1000 nm and frequency 100 Hz by the reduced model rG_{zz}.

3.1.7 Open Loop Resolution

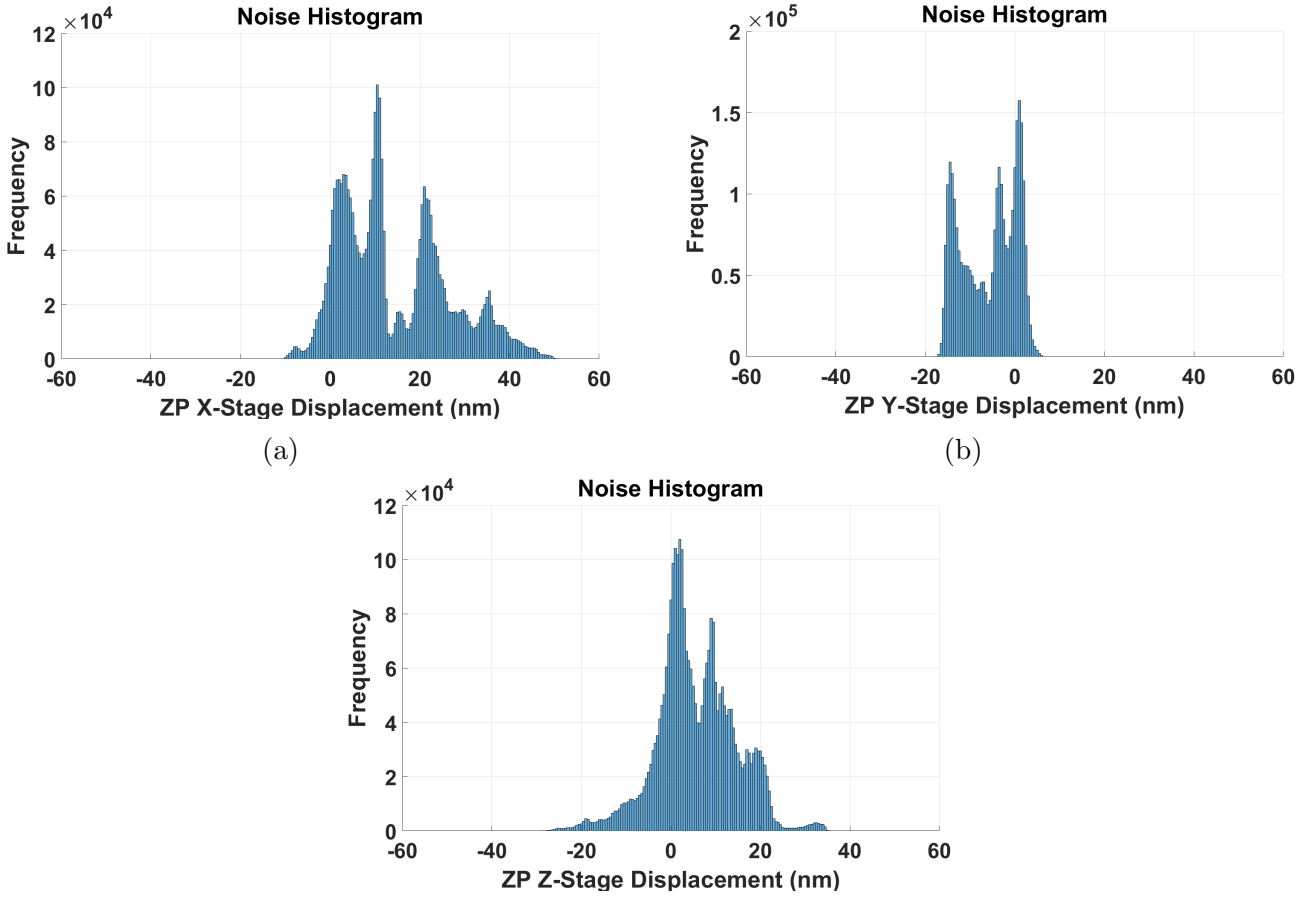

Figure 3.15: Noise histogram of Velociprobe optics stage displacement in open loop, (a) X-stage with 3σ positioning resolution of 33 nm, (b) Y-stage with $3\,\sigma$ positioning resolution of 12 nm, and (c) Z-stage with $3\,\sigma$ positioning resolution of 29 nm.

To calculate the resolution of the open loop X, Y, Z optics scanning stages a zero amplitude, zero frequency input were given to these stages and their respective displacement were measured. So, the only input going to the PI XYZ stages were environmental noise and disturbance. Noise histograms of each of the XYZ stage displacement were then plotted as shown in the Figure 3.15a, Figure 3.15b, and Figure 3.15c, respectively. None of the noise histograms are symmetric or has Gaussian distribution. The reason behind this is that the open loop XYZ stages are continuously and slowly drifting away from the starting point. All the noise histograms for XYZ stages in open loop have large offset from the mean and have large standard deviation. The large standard deviation means that the data is widely dispersed or spread away from the average. Based on the standard deviation (σ), the 3σ resolution of X, Y, and Z stage in open loop is approximately 33, 12, and 29 nm, respectively.

3.2 Control Design for Velociprobe

In this section, we are going to address the control design objectives, challenges, limitations observed for the case of Velociprobe XYZ fine positioning optics stages. In particular, we would showcase the designs with PID controller and H_∞ optimal controller, talk details about implementation and compare the results achieved with the Velociprobe X-ray microscope at the APS Sector 2 beamline.

3.2.1 PID Controller Algorithm

PID controllers were designed and used to establish the baseline performance of the Velociprobe optics fine positioning stages. The zone plate fine positioning stages are typically moved in a raster scan pattern to obtain the image of a sample. As such, a PID (or PI) controller becomes particularly attractive as compared to open loop because of the capability to track ramp signals with zero steady-state error due to the integral action. Since PID implementations are low order designs (usually first or second order), they are not flexible enough to simultaneously accommodate multiple design objectives such as tracking bandwidth, positioning resolution, and robustness. It is easy to implement and helps debug implementation issues in new control hardware.

3.2.1.1 Design

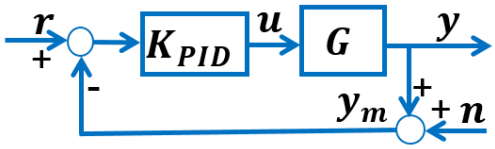

Figure 3.16: Transfer function block diagram of PID controller in feedback loop.

Figure 3.16 shows a PID controller K_{PID} in feedback loop with the experimentally identified XX-stage model $G = G_{xx}$. Where, r is the reference signal, y is XX-stage displacement, n is the measurement noise, and $y_m = y + n$ is the measured stage displacement. The PID controllers were designed by tuning the proportional, integral, and derivative design parameters with the objective of achieving large tracking bandwidth and stable controllers. The performance of the designed PID controller is verified through simulation of the discretized controllers in MATLAB simulation, Simulink simulation and LabVIEW simulation

(Figure 3.17). The designed continuous-time controllers were discretized using Tustin's (Bilinear) method or zero-pole matching method. Zero-pole matching method worked particularly well in the cases where the controller transfer function had high frequency dynamics. The controller dynamics are considered high frequency dynamics when the dynamics are in frequency region close to half of the sampling rate or Nyquist frequency. The typical sampling rate for controller implementations are 25 kHz. In the Simulink simulation, the discretized PID controllers were represented in biquad structure (detailed in the implementation section) and the plant was a continuous time transfer function model. In LabVIEW simulation both the controller and the identified plant model were represented by biquad structures. The independent simulations in Simulink and LabVIEW verified the performance of the designed discrete time control algorithms.

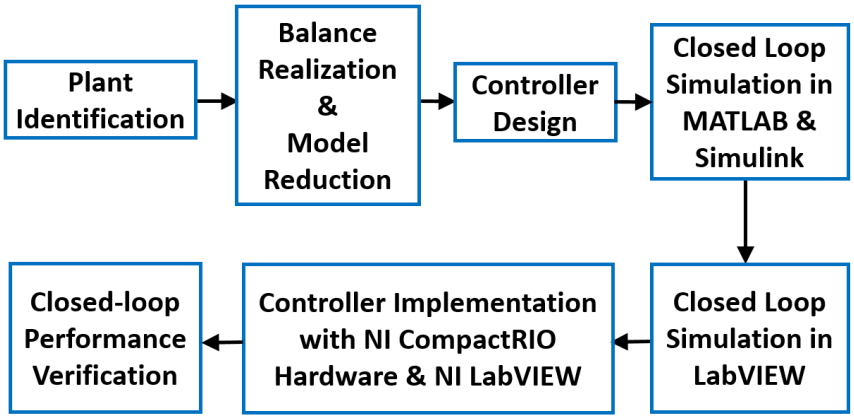

Figure 3.17: A block diagram showing the step-by-step process of designing and implementing a controller.

3.2.1.2 Implementation

The PID controllers for PI XYZ optics scanning stages were implemented in diagonal format, i.e. three separate controllers $K_{PID,XX}$, $K_{PID,YY}$, and $K_{PID,ZZ}$ were designed for the XX, YY, and ZZ-stages and were implemented without any consideration to the cross-coupling action between the stages. The discretized PID controllers were implemented through the NI cRIO control hardware and NI LabVIEW. NI cRIO system includes a reconfigurable FPGA chassis, an embedded real-time controller, and I/O modules. The discrete controllers are run at a certain rate (here we chose 25 kHz, which is flexibly specifiable) on the FPGA that is in the cRIO chassis. The existing function blocks for PID controller and transfer function in the LabVIEW FPGA library had some limitations and were not used. Controller transfer

functions having an order more than two were not successfully implementable using the existing transfer function block. So, an alternative way of representing the transfer functions in the FPGA had to be found. The biquad structure [40] or the "second order sections" shown in Figure 3.18 was utilized. One biquad or one second order section represents a second order transfer function. Using the second order sections in series, any order controller transfer function can be represented. PID controllers were represented by this biquad structures in the FPGA for implementation in the experiment. Running the controller directly in the FPGA fabric significantly increases the close loop rate and minimizes the latency.

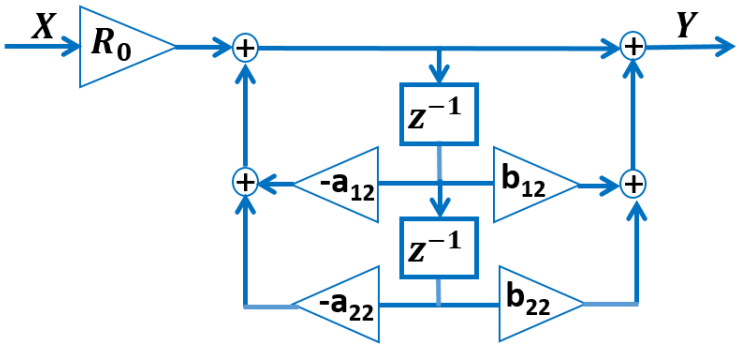

Figure 3.18: A Biquad structure showing one second order section that can represent a second order transfer function.

A stable PID controller $K_{PID,XX}$ with $-3\,dB$ bandwidth of 149 Hz was implemented successfully on the Velociprobe optics scanning X-stage. The bode plot of the PID controller is shown in Figure 3.19. The transfer function of the PID controller is as follows,

$$K_{PID,XX} = \frac{-0.001783\,s^2 - 850.4\,s - 1.138e06}{s^2 + 1596\,s} \tag{3.11}$$

For Y and Z stage, PID controllers $K_{PID,YY}$ and $K_{PID,ZZ}$ with -3 dB bandwidth of 134 Hz and 151 Hz, respectively, were implemented successfully on the Velociprobe optics scanning X-stage. The transfer functions $K_{PID,YY}$ and $K_{PID,ZZ}$ controllers are as follows,

$$K_{PID,YY} = \frac{-0.0383\,s^2 - 2459\,s - 2.895e6}{s^2 + 1707\,s} \tag{3.12}$$

$$K_{PID,ZZ} = \frac{-0.01638\,s^2 - 808.2\,s - 8.91e5}{s^2 + 1342\,s} \tag{3.13}$$

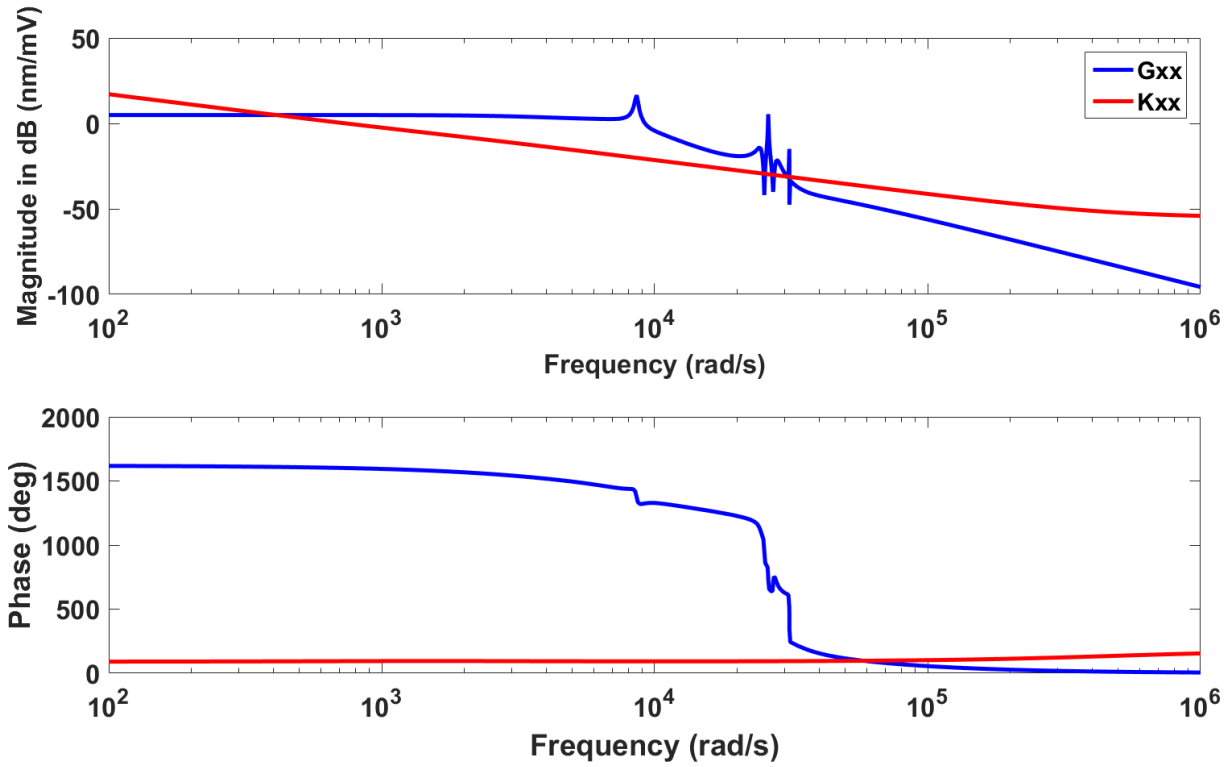

Figure 3.19: Bode plot of a $149\,Hz$ $-3\,dB$ bandwidth PID controller for XX-stage.

$$e = r - y = r - G\,u = r - GKe \tag{3.14}$$

$$e = (1 + GK)^{-1}\,r = S\,r \tag{3.15}$$

$$y = G\,u = GKe = GK(r - y) \tag{3.16}$$

$$y = (1 + GK)^{-1}\,GK\,r = T\,r \tag{3.17}$$

Where, $S = 1/(1 + G\,K)$ is the sensitivity transfer function, which is a closed-loop transfer function map from reference r to tracking error signal, $e = r - y$, and $T = G\,K/(1 + G\,K)$, known as the complementary sensitivity transfer function, is the closed-loop transfer function map from reference r to the system output y. The sensitivity transfer function can also be expressed as $\frac{dy/y}{dG/G}$ that represents the percentage change in the plant output to percentage change in the plant model. In other words, S gives a measure of robustness of the closed-loop system to uncertainty in the identified plant model G. A general criteria for robust stability of the closed-loop is the peak of the sensitivity transfer function S should be less than 6 dB or, in other words,

$$\|S\|_\infty \leqslant 2 \tag{3.18}$$

The -3 dB bandwidth ω_b is determined based on the frequency corresponding the point sensitivity transfer function S crosses of the -3 dB line. For larger bandwidth S should cross the -3 dB line as late as possible. Similarly, ω_{bt} is the bandwidth determined by the crossing of the -3 dB line by the complementary sensitivity transfer function T. Smaller the value of ω_{bt} the greater the noise attenuation and better the positioning resolution. Bandwidth ω_{bt} would be smaller if T starts rolling off early and has a has high roll-off rate. Since, $y = Tr$ so it is expected that the value of T be approximately equal to 1 in the frequency region where good tracking is required. These, requirements would determine the shape of T transfer function.

3.2.1.3 Implementation Verification

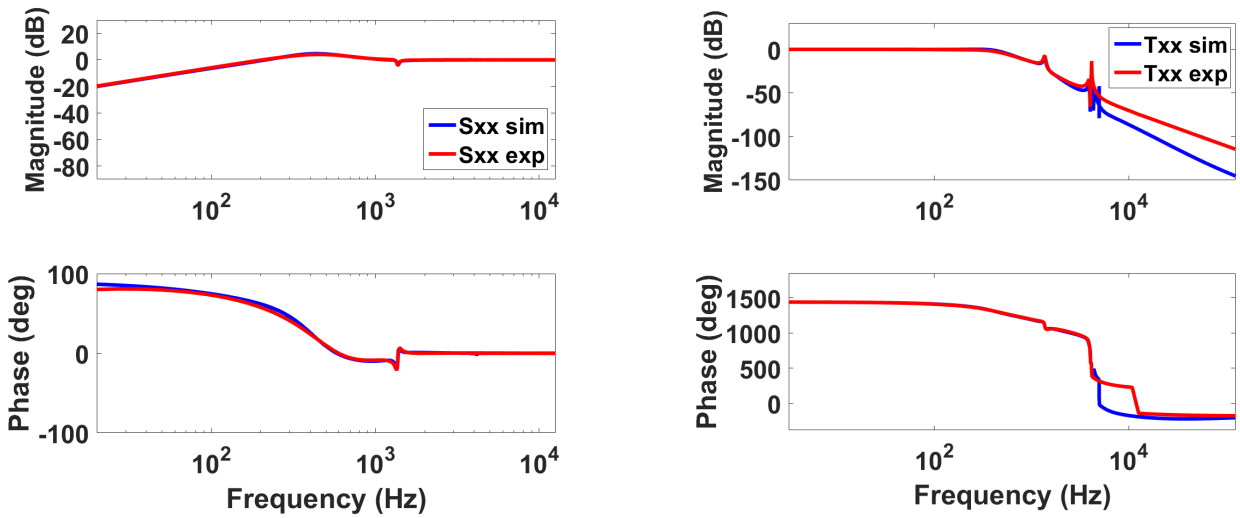

(a) (b)

Figure 3.20: Comparing the design and experimental closed loop transfer function for the scanning X stage. (a) Bode plot of $S_{xx,sim}$ and $S_{xx,exp}$, and (b) Bode plot of $T_{xx,sim}$ and $T_{xx,exp}$.

It is imperative to make sure that the designed discrete controllers are being implemented in NI cRIO FPGA properly and with high fidelity. To verify that the designed controllers

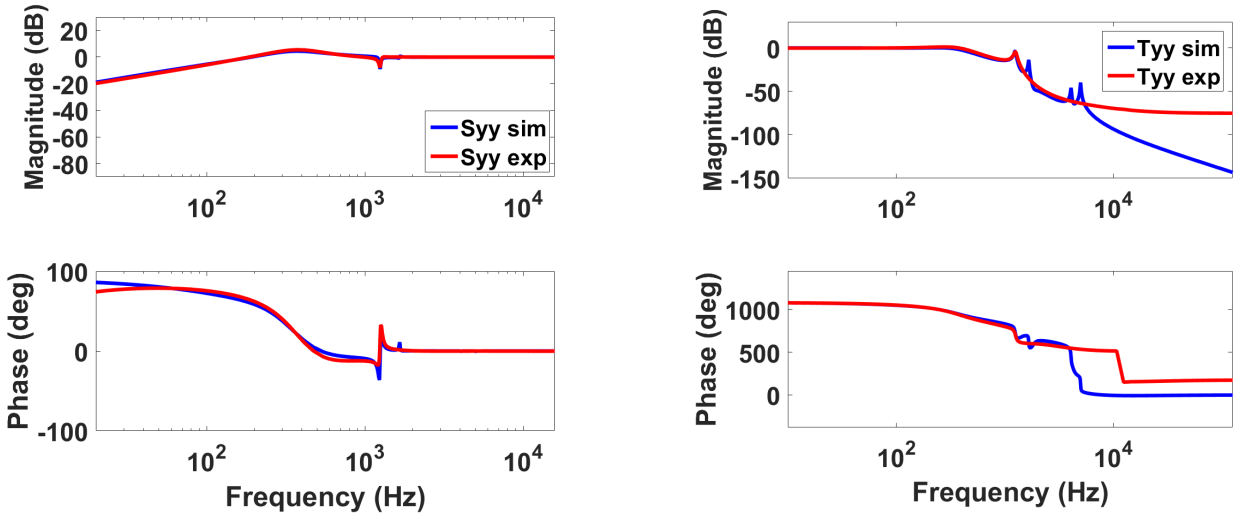

(a) (b)

Figure 3.21: Comparing the design and experimental closed loop transfer function for the scanning Y stage. (a) Bode plot of $S_{yy,sim}$ and $S_{yy,exp}$, and (b) Bode plot of $T_{yy,sim}$ and $T_{yy,exp}$.

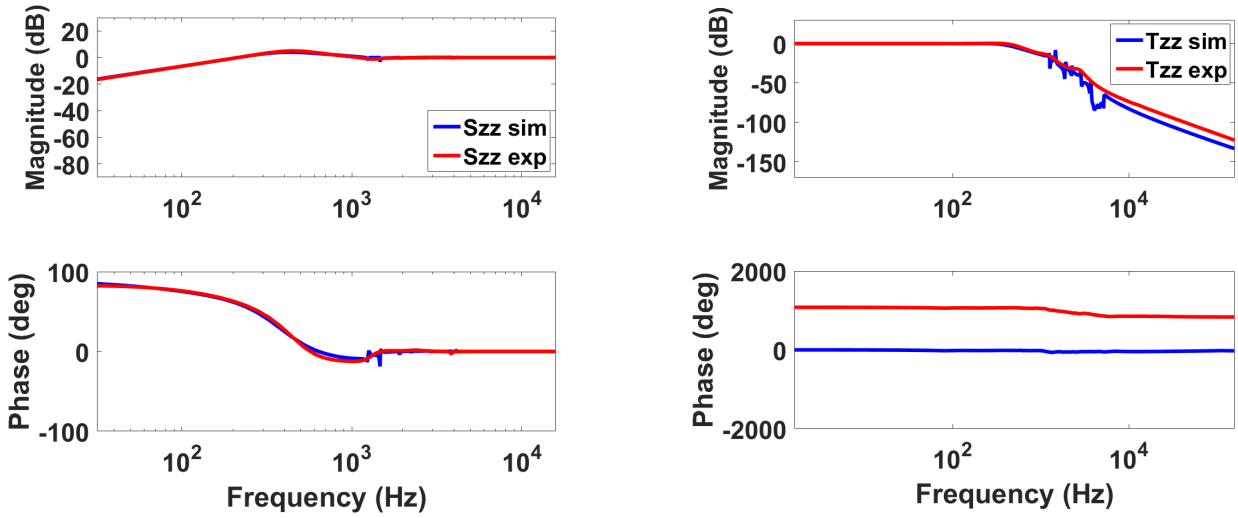

(a) (b)

Figure 3.22: Comparing the design and experimental closed loop transfer function for the scanning Z stage. (a) Bode plot of $S_{zz,sim}$ and $S_{zz,exp}$, and (b) Bode plot of $T_{zz,sim}$ and $T_{zz,exp}$.

were implemented properly, the closed-loop sensitivity transfer function S and complementary sensitivity transfer function T needs to be identified from experimental data and compared to the corresponding design transfer functions. The comparison between the experimental and simulation S_{xx} and T_{xx}, for the scanning X-stage, are shown in the Figure 3.20a and Figure 3.20b, respectively. The experimental $S_{xx,exp}$ and design $S_{xx,sim}$ transfer functions matches closely except at very low frequency. The bandwidth based on the S transfer function, gives $\omega_{b\,sim} = 149$ Hz and $\omega_{b\,exp} = 141$ Hz for simulation and experimental, respectively. In case of, $T_{xx,exp}$ and $T_{xx,sim}$ the match is good except at very high frequency. The bandwidth based on T transfer function are $\omega_{bt\,sim} = 442$ Hz and $\omega_{bt\,exp} = 497$ Hz for simulation and experimental, respectively.

The comparison between the experimental and simulation closed loop transfer function S_{yy} and T_{yy} for the scanning Y stage are shown in the Figure 3.21a and Figure 3.21b, respectively. The experimental $S_{yy,exp}$ and design $S_{yy,sim}$ sensitivity transfer functions matches closely except at very low frequency. In case of complementary sensitivity transfer function $T_{yy,exp}$ and $T_{yy,sim}$ the match is good except at very high frequency. The bandwidth based on the S transfer function, gives $\omega_{b\,sim} = 134$ Hz and $\omega_{b\,exp} = 135$ Hz for simulation and experimental, respectively. The bandwidth based on T transfer function are $\omega_{bt\,sim} = 416$ Hz and $\omega_{bt\,exp} = 474$ Hz for simulation and experimental, respectively.

In case of Z-stage, the comparison between the experimental and simulation closed loop transfer function S_{zz} and T_{zz} for the scanning Z stage are shown in the Figure 3.22a and Figure 3.22b, respectively. The experimental $S_{zz,exp}$ and design $S_{zz,sim}$ sensitivity transfer functions matches closely except at very low frequency. In case of complementary sensitivity transfer function, $T_{zz,exp}$ and $T_{zz,sim}$ matched closely except at very high frequency, but has a approximately same roll-off rate. The bandwidth based on the S transfer function, gives $\omega_{b\,sim} = 151$ Hz and $\omega_{b\,exp} = 150$ Hz for simulation and experimental, respectively. The bandwidth based on T transfer function are $\omega_{bt\,sim} = 450$ Hz and $\omega_{bt\,exp} = 530$ Hz for simulation and experimental, respectively.

3.2.1.4 Results

3.2.1.4.1 Tracking Results Here, the tracking results for the X (horizontal stage) and Y (vertical stage) scanning stages of the Velociprobe X-Ray microscope will be showcased. Tracking experiments, with the PID controllers running, were carried out with the X-Ray microscope optics fine positioning stages. The tracking of sine wave reference trajectory

with amplitude 1000 nm and frequency 100 Hz and 200 Hz with optics X-stage is shown in the Figure 3.23a and Figure 3.23c. The X-stage closed loop tracking error (Figure 3.23b and Figure 3.23d) is quiet big for the cases of both reference signals. The higher reference frequency of 200 Hz results in larger error due the being beyond the -3 dB bandwidth of the X-stage PID controller. The vertical Y-stage tracking with same reference signals are shown in Figure 3.24a and Figure 3.24c. PID controllers tracks 100 Hz triangular wave better than the 200 Hz one, due to the former being within design bandwidth. The Y-stage closed loop tracking error (Figure 3.24b and Figure 3.24d) is also quiet large.

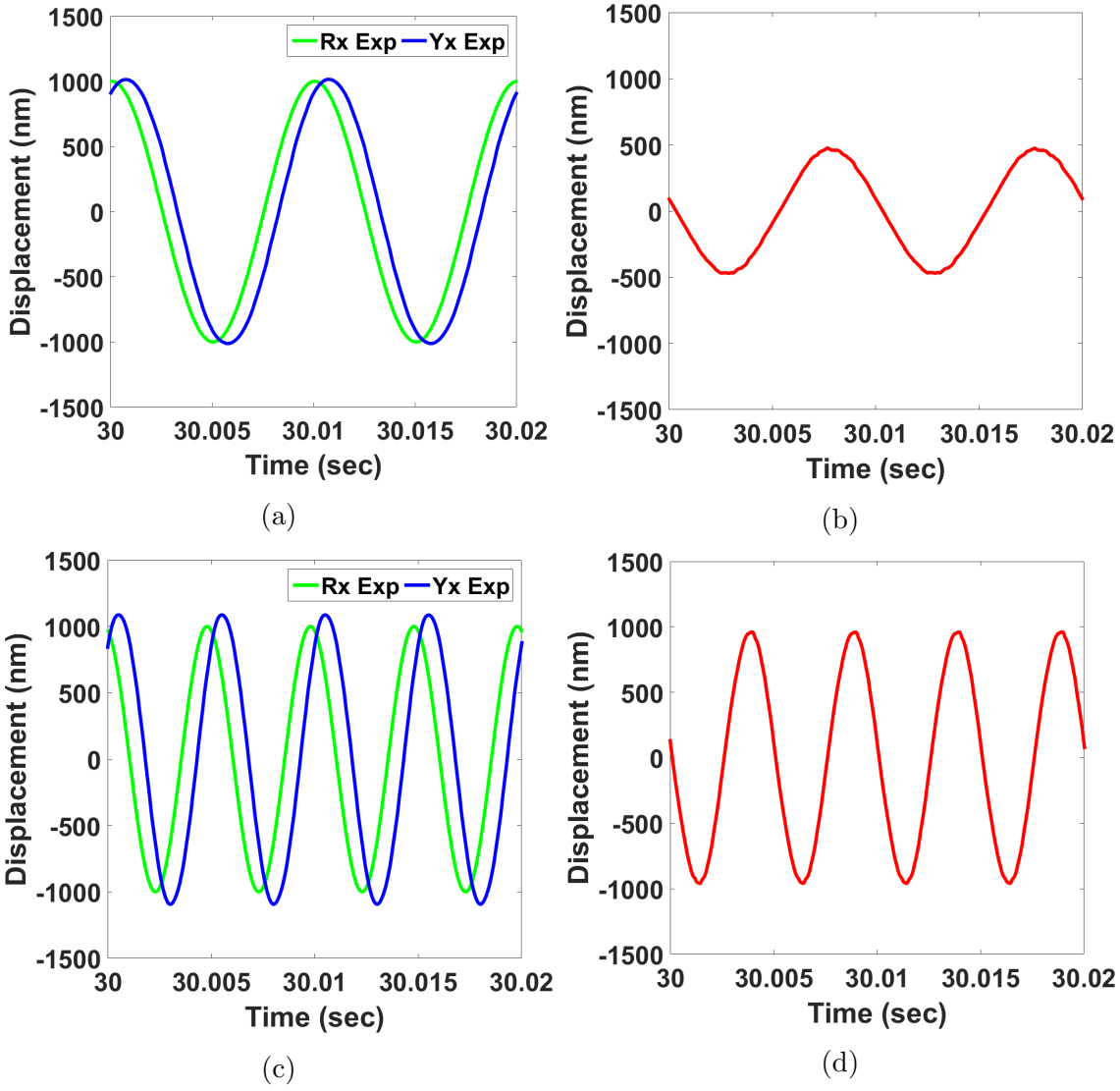

Figure 3.23: X-Stage sine wave reference tracking for 149 Hz -3 dB bandwidth PID controller, (a) 1000 nm amplitude 100 Hz sine wave reference tracking, and (c) 1000 nm amplitude 200 Hz sine wave reference tracking. (b) and (d) are the corresponding tracking error.

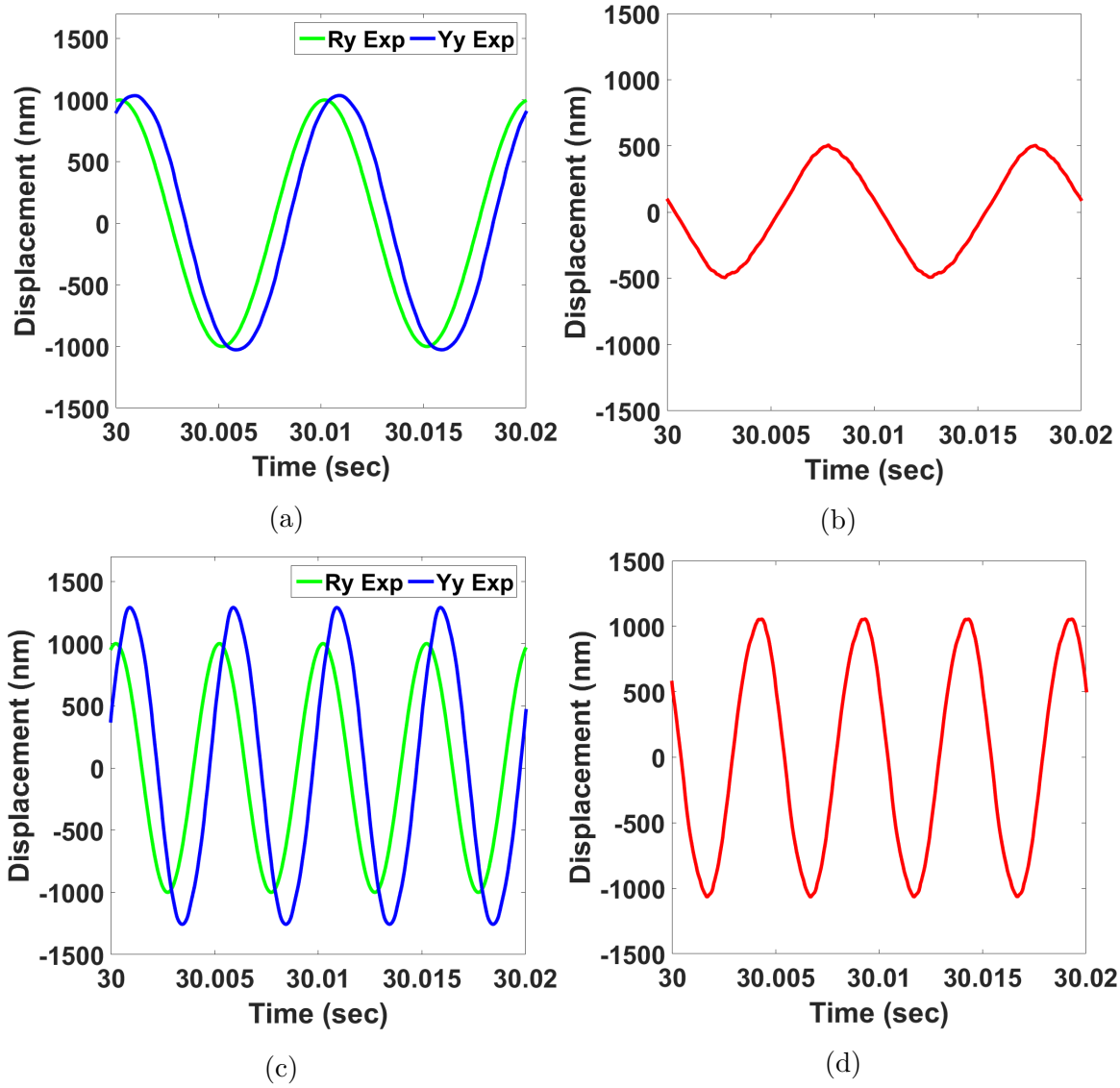

Figure 3.24: For Velociprobe X-Ray microscope XY-plane is the scanning plane, which is vertical to the incoming X-ray beam along Z-axis. Two different sine wave reference with same amplitude of 1000 nm and frequency 100 Hz and 200 Hz, respectively, were given to the Y-stage for tracking performance verification of a 134 Hz -3 dB bandwidth PID controller. Here, (a) 1000 nm amplitude 100 Hz sine wave reference tracking, and (c) 1000 nm amplitude 200 Hz sine wave reference tracking. (b) and (d) are the corresponding tracking error. The tracking error is much larger in case of 200 Hz frequency reference since it is beyond the -3 dB bandwidth of the PID controller for Y-stage. 200 Hz reference frequency was chosen to compare tracking performance with robust optimal controller, which is shown in later sections

3.2.1.4.2 Positioning Resolution Results The positioning resolution of the closed loop system was calculated by giving zero amplitude, and zero frequency input to the PID XYZ fine positioning stages and the stage displacement were measured simultaneously. A noise histogram of the closed-loop stage displacement and open loop stage displacement is shown in the Figure 3.25a, Figure 3.25b, and Figure 3.25c for XX, YY, and ZZ stage, respectively. The noise histogram for closed-loop is symmetric and has much smaller standard deviation than open loop. Based on the standard deviation (σ), the 3σ resolution of the closed-loop data is approximately 1.9 nm, 1.5 nm, and 2.0 nm for XX, YY, and ZZ stage, respectively, which is 194%, 187.5%, and 193% improvement of positioning resolution over open loop.

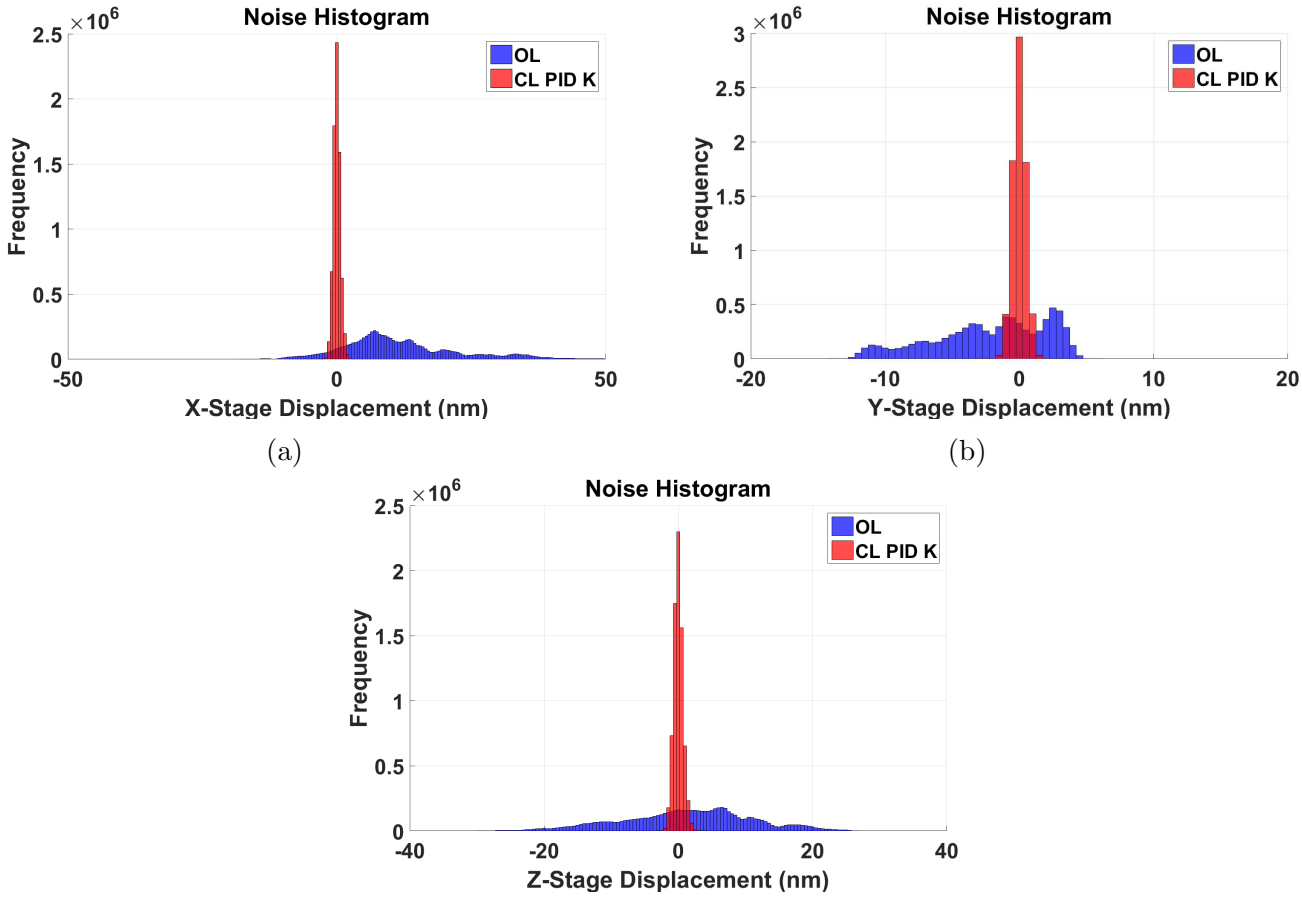

Figure 3.25: Comparing noise histogram of Velociprobe optics stage displacement in open loop and closed loop with PID controller; (a) X-stage closed loop 3σ positioning resolution with PID is 1.9 nm compared to 33 nm open loop resolution, (b) Y-stage closed loop 3σ positioning resolution with PID is 1.5 nm compared to 12 nm open loop resolution, and (c) Z-stage closed loop 3σ positioning resolution with PID is 2.0 nm compared to 29 nm open loop resolution.

3.2.2 H_∞ Controller Algorithm

In the Velociprobe work we use the H_∞ control design architecture, where we pose an optimization problem that incorporates simultaneously the design objectives of large tracking bandwidth, high positioning resolution, bounded control effort, sufficient environmental disturbance rejection, and attenuation of measurement noise. The H_∞ algorithm gives a generalized framework through which the desired closed-loop objectives can addressed.

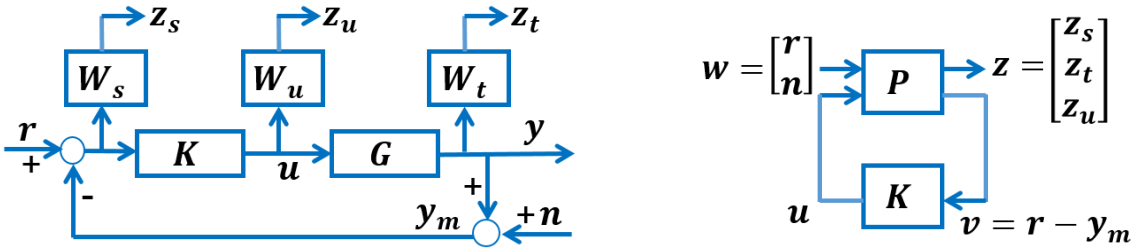

(a) (b)

Figure 3.26: Closed loop transfer function block diagrams for the $S\backslash T\backslash KS$ mixed sensitivity minimization problem. (a) Closed loop system with the identified plant model G, reference r, controller output u, measurement noise n, design weights W_s, W_t, W_u, and regulated outputs $z = [z_s\ z_t\ z_u]^T$, (b) Generalized plant framework with the transfer function going from exogenous inputs $w = [r\ d\ n]^T$ to regulated outputs z to be minimized to achieve the optimum control law K. The error signal $v = r - y_m$ available to the controller is utilized to give the proper controller output u. Here, $y_m = y + n$ is the measured displacement of the stages.

For the transfer function block diagram shown in Figure 3.26a the closed-loop sensitivity transfer function S and the complementary sensitivity transfer function T are given as follows,

$$S = \frac{1}{(1+GK)}, \qquad T = \frac{GK}{(1+GK)} = I - S \tag{3.19}$$

The closed-loop objectives are as follows:

- The controller K needs to stabilize the system G.
- For disturbance rejection the maximum singular value of S needs to be small
- For reference tracking the maximum singular value of $T \approx 1$
- For noise attenuation the maximum singular value of T needs to be small
- For control energy to be small the maximum singular value of KS needs to be small

In the 1 DOF H_∞ algorithm the closed-loop objectives are achieved by designing the weights W_s, W_t, and W_u to shape the closed-loop transfer functions S, T, and KS, respectively. The weights are designed in such way so that the H_∞ algorithm minimizes the H_∞ norm of the weighted closed-loop transfer functions $\|W_p\,S\|_\infty$, $\|W_t\,T\|_\infty$, and $\|W_u\,KS\|_\infty$ for some stabilizing controller K. The block diagram in Figure 3.26a can be expressed in the general control configuration as shown in Figure 3.26b. Here, $w = [r\ n]^T$ is the exogenous input signals, u is the control signal, v is the measured variable, and $z = [z_s\ z_t\ z_u]$ are the error signals or regulated variables. P is the generalized plant which contains the nominal plant G and all the design weights W_s, W_t, and W_u. The controller K is the robustly stabilizing H_∞ controller that provides with all the closed-loop objectives. The regulated variables are the signals of interest in the optimization problem. The weighted tracking error $z_s = W_s\,(r - y)$ gives an idea about the tracking error objective, the weighted stage displacement $z_t = W_t\,y$ reflects the noise attenuation and tracking objective, and weighted control effort $z_u = W_u\,u$ reflects the bound on the control effort.

$$\left[\begin{array}{c} z_s \\ z_t \\ z_u \\ \hline v \end{array}\right] = \left[\begin{array}{cc|c} W_s & -W_s & -W_sG \\ 0 & 0 & W_tG \\ 0 & 0 & W_u \\ \hline I & -I & -G \end{array}\right] \left[\begin{array}{c} r \\ n \\ \hline u \end{array}\right] \tag{3.20}$$

$$\left[\begin{array}{c} z \\ \hline v \end{array}\right] = \left[\begin{array}{c|c} P_{11}(s) & P_{12}(s) \\ \hline P_{21}(s) & P_{22}(s) \end{array}\right] \left[\begin{array}{c} w \\ \hline u \end{array}\right] = P(s) \left[\begin{array}{c} w \\ \hline u \end{array}\right] \tag{3.21}$$

Lets consider, that the generalized plant has the following state-space realization,

$$P(s) = \left[\begin{array}{c|cc} A & B_1 & B_2 \\ \hline C_1 & D_{11} & D_{12} \\ C_2 & D_{21} & D_{22} \end{array}\right] \tag{3.22}$$

The H_∞ norm of the close-loop transfer function from w to z is minimized in the H_∞ controller design process. This closed-loop transfer function is given by the lower linear fractional transformation, given as follows,

$$F_l(P, K) = P_{11} + P_{12}K(I - P_{22}K)^{-1}P_{21} \tag{3.23}$$

In particular, the lower linear fractional transformation can be given in terms of the weighting transfer functions and closed-loop transfer functions (Equation 3.25).

$$\begin{bmatrix} z_s \\ z_t \\ z_u \end{bmatrix} = \begin{bmatrix} W_sS & -W_sS \\ W_tT & -W_tT \\ W_uKS & -W_uKS \end{bmatrix} \begin{bmatrix} r \\ n \end{bmatrix} \tag{3.24}$$

$$z = \begin{bmatrix} W_sS & -W_sS \\ W_tT & -W_tT \\ W_uKS & -W_uKS \end{bmatrix} \omega = F_l(P,K)\,\omega \tag{3.25}$$

The goal of this multi-objective optimization is to minimize the H_∞ norm of the lower linear fractional transformation, $F_l(P,K)$

$$\|F_l(P,K)\|_\infty = \max_\omega \sigma_{max}(F_l(p,K)(j\omega)) \tag{3.26}$$

$$\min_{stab.\,K} \|F_l(P,K)\|_\infty = \min_{stab.\,K} \max_\omega \sigma_{max}(F_l(p,K)(j\omega)) \tag{3.27}$$

$$\min_{stab.\,K} \|F_l(P,K)\|_\infty = \min_{stab.\,K} \left\| \begin{bmatrix} W_sS & -W_sS \\ W_tT & -W_tT \\ W_uKS & -W_uKS \end{bmatrix} \right\|_\infty \tag{3.28}$$

Since, the columns of $F_l(P,K)$ shows the same terms corresponding to r and n, we can simplify the optimization problem by considering only one column corresponding to r.

$$\min_{stab.\,K} \|F_l(P,K)\|_\infty = \min_{stab.\,K} \left\| \begin{bmatrix} W_sS \\ W_tT \\ W_uKS \end{bmatrix} \right\|_\infty \tag{3.29}$$

As mentioned before designing optimal controller demands large computational effort and is unnecessary. It is a better idea to design a suboptimal controller. Suppose, the minimum value of the H_∞ norm of $F_l(P,K)$ be γ_{min}. Multi-objective optimization using a suboptimal $\gamma > \gamma_{min}$ gives a suboptimal H_∞ controller.

$$\gamma_{min} = \min_{stab.\,K} \|F_l(P,K)\|_\infty \tag{3.30}$$

$$\|F_l(P,K)\|_\infty < \gamma \tag{3.31}$$

Equation 3.31 is solved iteratively, where a bisection algorithm is used to choose a value of γ that approaches γ_{min} iteratively, until it is accurate enough based on a predetermined tolerance. In every iteration it is verified that $\gamma > \gamma_{min}$ holds.

3.2.2.1 Design

The design objectives of H_∞ control algorithm are robust stability, large tracking bandwidth, high positioning resolution, noise attenuation and disturbance rejection. Some of the fundamental constraints on achieving design objectives are:

- $S + T = 1$
- The Bode integral law: $\int_0^\infty log|S(j\omega)|\, d\omega = 0$
- $\omega_b < \omega_{bt}$

For large tracking bandwidth and good disturbance rejection the sensitivity transfer function S needs to be small up to the bandwidth frequency. For good noise attenuation complementary sensitivity transfer function needs to be small at frequencies where noise are predominant (usually in the high frequency region). Due to the first fundamental constraint T will have to be large in the frequencies S is small and vice-versa. This will result in a trade-off between the tracking bandwidth and positioning resolution. The Bode integral law states that if the S is low at some frequency range then it will have to be large at other frequencies. This means if S is kept small for a large frequency range a peak of S will result in high frequency region resulting into lack of robust stability. The third fundamental constraint brings in the trade-off between bandwidth and resolution into play. If high bandwidth is targeted then the resolution will be low and vice-versa.

The design weights W_s, W_t, and W_u are chosen so as to emphasize the frequency ranges where the corresponding signals z_s, z_t, and z_u are to be small; accordingly, $|W_s(j\omega)|$, $|W_t(j\omega)|$, and $|W_u(j\omega)|$ are designed to have high magnitudes respectively at frequencies up to desired tracking bandwidth, at high frequencies where noise attenuation is desired, and at frequencies up to bandwidth to ensure that control signal is bounded and implementable. Such a choice of W_s (as a low-pass filter) places an upper bound on the S transfer function in a way that S becomes small at low frequency; resulting in a system having small tracking error below the crossover frequency. The crossover frequency of W_s is chosen such that it covers the frequency range where small tracking error is desired. This constraint effectively enforces a lower bound to the achievable closed loop bandwidth ω_b [39]. Typically, the bandwidth of

the closed loop system is usually defined by the -3 dB bandwidth, which is the minimum frequency at which the magnitude $|S(j\omega)|$ becomes greater than -3 dB (note that -3 dB $\approx$ 70%). Thus an X-ray microscope scanner with a -3 dB bandwidth of ω_b Hz implies that the magnitude of tracking error is smaller than 70% of the magnitude of reference signal when its (reference signals) frequency components are within ω_b Hz. In this article, we will define analogously -40 dB bandwidth instead as a measure of bandwidth (note -40 dB = 1%).

In particular, the sensitivity weighting transfer function W_{sx} (Figure 3.27)for a controller designed for the Velociprobe optics scanning X-stage was chosen to be a first order proper transfer function given by Equation 3.32, where the magnitude of $1/W_{sx}$ has a gain less than -40 dB (1%) up to frequency of 16.3 rad/s (2.6 Hz). The maximum bandwidth H_∞ controller designed for X-stage was 200 Hz, which is 134% improvement in -3 dB bandwidth over that of PID controller.

$$W_{sx} = \frac{0.25\,s + 3142}{s + 3.142} \tag{3.32}$$

The complementary sensitivity weighting transfer function W_t influences high frequency noise attenuation and puts an upper bound on the bandwidth. It is chosen such that $1/W_t$ has the shape of a low-pass filter. Choosing $1/W_t$ in this way places an upper bound on the complementary sensitivity transfer function T. This results in the open loop transfer function GK and the complementary sensitivity transfer function $T = GK/(1 + GK)$ both to roll-off beyond the cross over frequency ω_{bt}. This design prevents high frequency noise from passing through the controller and being amplified in the closed loop system. The earlier in the frequency spectrum T rolls-off, the less noise will pass through the system, resulting in higher positioning resolution. However, $1/W_t$ also places an upper-limit on the closed loop tracking bandwidth (typically $\omega_b < \omega_{bt}$), therefore the design has to account for the corresponding trade-off between tracking bandwidth and noise attenuation [39].

Positioning resolution of a scanner, the smallest realizable displacement, is defined in terms of the statistics of the scanner motion measurements when the reference signal is zero. In this article we define the scanner positioning resolution as three times the standard deviation of such signal measured over a long time (over 5 minutes at 25 kHz sampling rate). Note that the scanner displacement is given by $y = Tn$ when the reference $r = 0$. In general, sensor noise is introduced into the system at high frequency, so designs with smaller ω_{bt} (lower roll-off frequencies for T) and with a higher roll-off rate (that is steeper slope for $|T(j\,\omega)|$ for $\omega > \omega_{bt}$) result in higher positioning resolution.

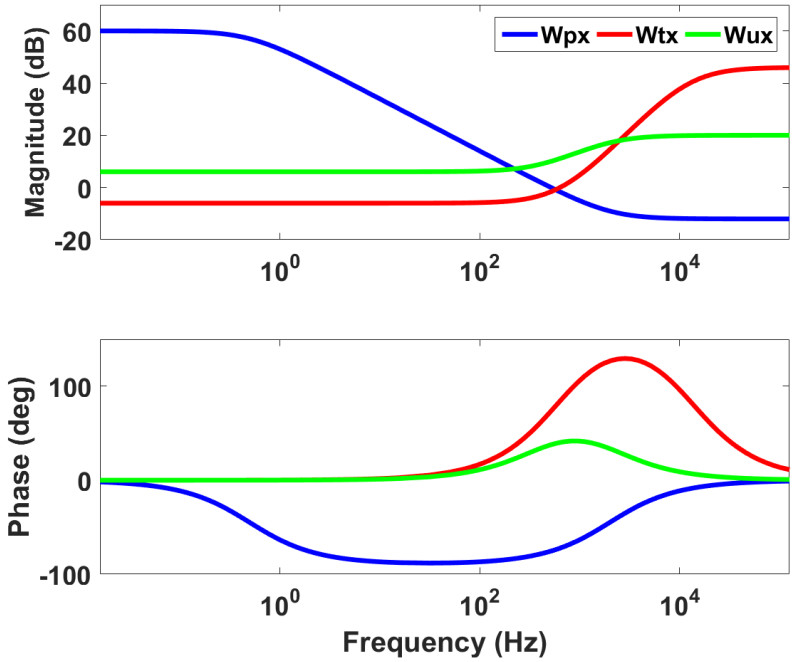

Figure 3.27: The weighting transfer functions W_{sx}, W_{tx}, and W_{ux} for the Velociprobe optics scanning X-stage corresponding to the H_∞ controller with -3 dB bandwidth 200 Hz and -40 dB bandwidth of 2.6 Hz.

For the same fine positioning X-stage controller (200 Hz -3 dB bandwidth) the complementary sensitivity weight W_{tx} was chosen to be a second order proper transfer function given by Equation 3.33. Here, $|1/W_{tx}(j\omega)|$ is greater than 0 dB (100%) up to frequency of 607 Hz and with a gain less than -8 dB at 1.3 kHz and rolling off at higher frequencies.

$$W_{tx} = \frac{s^2 + 7997\,s + 1.599e7}{0.005\,s^2 + 799.7\,s + 3.198e7} \tag{3.33}$$

The control effort weighting function W_u influences the size of the KS transfer function to prevent controller output saturation or meet other hardware limitations. It is chosen such that $1/W_u$ places an upper bound on the KS transfer function. For Velociprobe optics X-Stage the control effort weighting function is given as,

$$W_{ux} = \frac{10s + 2.513e4}{s + 1.257e4} \tag{3.34}$$

Figure 3.28 shows the Bode plot of the identified plant transfer function G_{xx} and the designed H_∞ controller K_{xx} (Appendix B) with 200 Hz -3 dB bandwidth and 2.6 Hz -40 dB bandwidth. The corresponding closed loop sensitivity transfer function S_{xx} and complementary sensitivity transfer function T_{xx} are also shown in the figure.

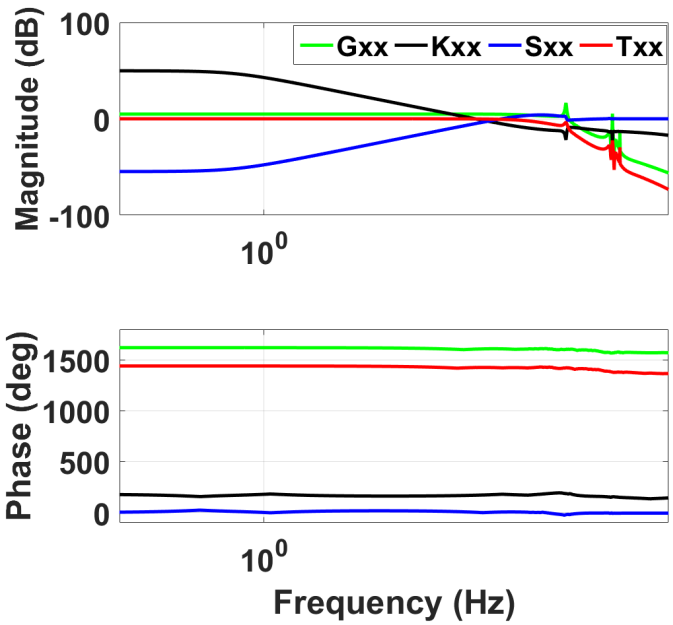

Figure 3.28: Bode diagram of the identified stage model G_{xx}, controller K_{xx}, sensitivity transfer function S_{xx} and complementary sensitivity transfer function T_{xx} are shown here.

In case of Velociprobe fine scanning Y-stage the highest -3 dB bandwidth achieved with H_∞ controller design is 200 Hz (150% improvement over PID controller), with a -40 dB bandwidth of 2.6 Hz. The sensitivity weighting transfer function W_{sy} (Figure 3.29) for this controller was chosen to be a first order proper transfer function given by Equation 3.35, where the magnitude of $1/W_{sy}$ has a gain less than -40 dB (1%) up to frequency of 15.5 rad/s (2.5 Hz).

$$W_{sy} = \frac{0.25s + 1571}{s + 0.9425} \tag{3.35}$$

For the same fine positioning Y-stage controller (200 Hz -3 dB bandwidth) the complementary sensitivity weight W_{ty} was chosen to be a fourth order proper transfer function given by Equation 3.36. Here, $|1/W_{ty}(j\omega)|$ is greater than 0 dB (100%) up to frequency of 811 Hz and with a gain less than -7 dB at 1.2 kHz and rolling off at higher frequencies. The control effort weighting function W_{uy} is given in the Equation 3.37.

$$W_{ty} = \frac{s^4 + 2.232e04s^3 + 1.868e08s^2 + 6.95e11s + 9.695e14}{0.0008333s^4 + 147.9s^3 + 9.847e06s^2 + 2.913e11s + 3.232e15} \tag{3.36}$$

$$W_{uy} = \frac{s + 3.142e04}{s + 9.425e04} \tag{3.37}$$

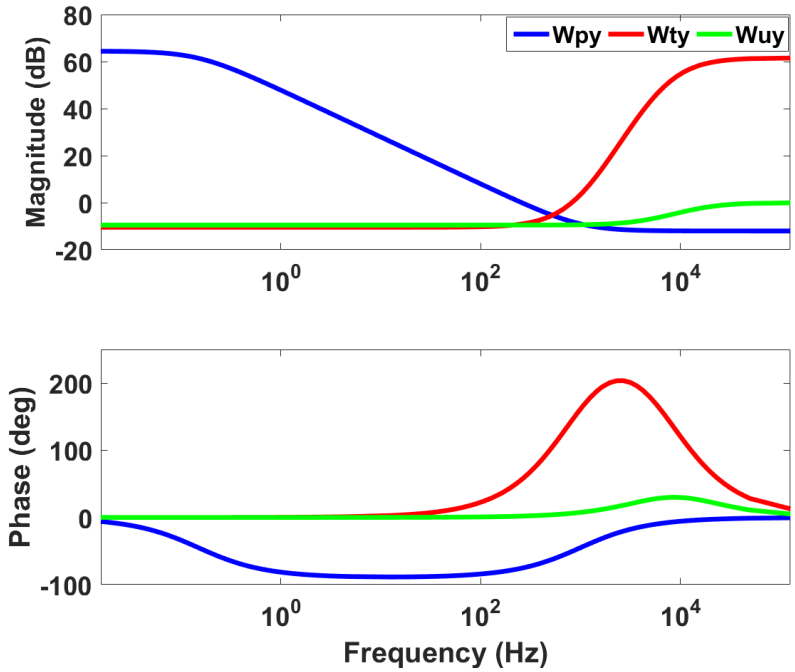

Figure 3.29: The weighting transfer functions W_{sy}, W_{ty}, and W_{uy} for the Velociprobe optics scanning X-stage corresponding to the H_∞ controller with -3 dB bandwidth 200 Hz and -40 dB bandwidth of 2.6 Hz.

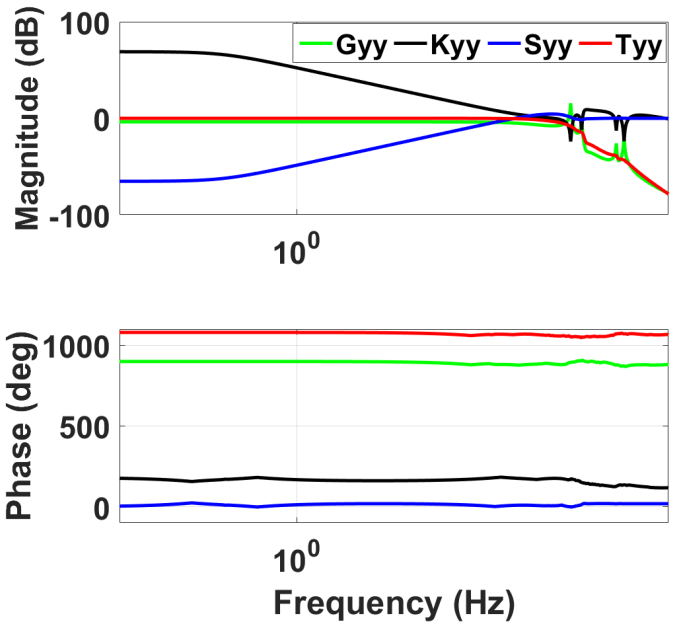

Figure 3.30: Bode diagram of the identified stage model G_{yy}, controller K_{yy}, sensitivity transfer function S_{yy} and complementary sensitivity transfer function T_{yy} are shown here.

Figure 3.30 shows the Bode plot of the identified plant transfer function G_{yy} and the designed H_∞ controller K_{yy} (Appendix B) with 200 Hz -3 dB bandwidth and 2.7 Hz -40 dB bandwidth. The closed loop transfer functions S_{yy} and T_{yy} are also shown in the figure.

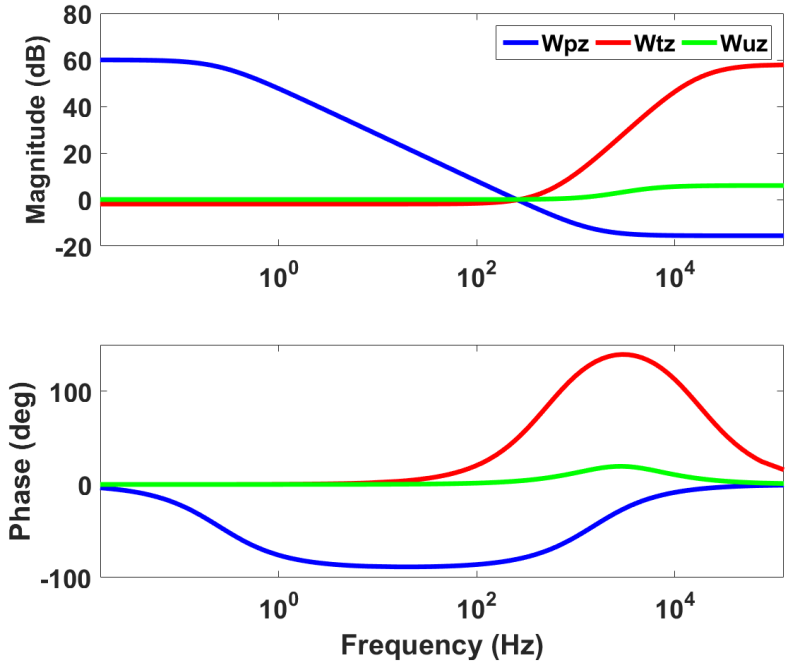

Figure 3.31: The weighting transfer functions W_{sz}, W_{tz}, and W_{uz} for the Velociprobe optics scanning X-stage corresponding to the H_∞ controller with -3 dB bandwidth 200 Hz and -40 dB bandwidth of 2.7 Hz.

Similarly, the design weights W_{sz}, W_{tz}, and W_{uz} for the H_∞ controller designed for the optics Z-stage is given in the following Equations. The maximum -3 dB bandwidth achieved was 200 Hz with a -40 dB bandwidth of 2.65 Hz. The design weights are plotted as a Bode diagram in Figure 3.31. The H_∞ design was an improvement of 132% over the PID controller design.

$$W_{sz} = \frac{0.1667s + 1571}{s + 1.571} \tag{3.38}$$

$$W_{tz} = \frac{s^2 + 6744s + 1.137e07}{0.00125s^2 + 266.6s + 1.421e07} \tag{3.39}$$

$$W_{uz} = \frac{2s + 2.513e04}{s + 2.513e04} \tag{3.40}$$

Figure 3.32 shows the Bode plot of the identified plant transfer function G_{zz} and the

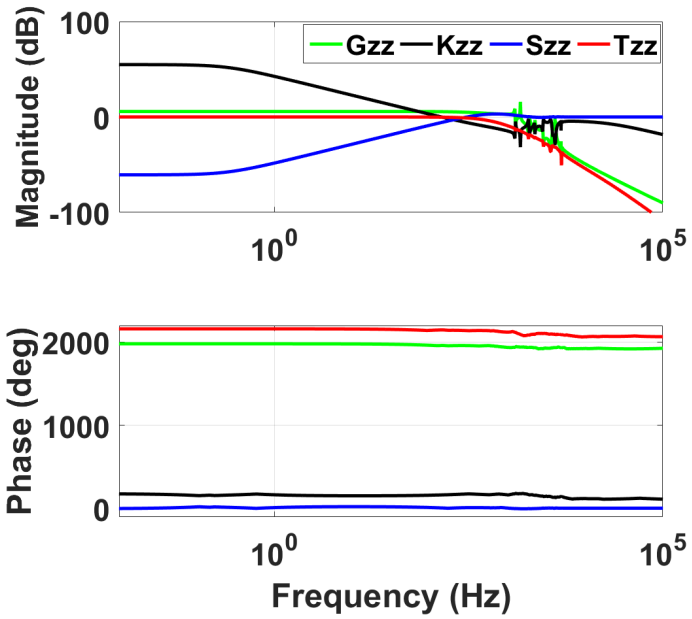

Figure 3.32: Bode diagram of the identified stage model G_{zz}, controller K_{zz}, sensitivity transfer function S_{zz} and complementary sensitivity transfer function T_{zz} are shown here.

designed H_∞ controller K_{zz} (Appendix B) with 200 Hz -3 dB bandwidth and 2.6 Hz -40 dB bandwidth. The closed loop transfer functions S_{zz} and T_{zz} are also shown in the figure.

3.2.2.2 Implementation

The designed continuous-time H_∞ controllers are discretized using the Tustin's method or zero-pole matching method and implemented on Velociprobe optics scanning stages in diagonal form. The discrete controllers were represented as biquad structures as explained before. Controllers up to bandwidth of 200 Hz were designed and implemented on the X,Y, and Z stages, which resulted in an improvement over 130% for all stages when compared to the corresponding PID controllers.

To verify that the controllers were implemented properly the closed-loop transfer functions S and T needs to be identified from experimental data and compared to the corresponding design transfer functions. The bode plot of XX-stage closed loop sensitivity transfer function S_{xx} and complementary sensitivity transfer function T_{xx} for simulation and experiment are plotted in the Figure 3.33a and Figure 3.33b, respectively. The experimental S_{xx} and T_{xx} transfer functions matches closely with the the simulation results. The bandwidth based on the S transfer function, gives $\omega_{b\,sim} = 200$ Hz and $\omega_{b\,exp} = 192$ Hz for simulation and experimental, respectively. The bandwidth based on T transfer function are $\omega_{bt\,sim} = 650$

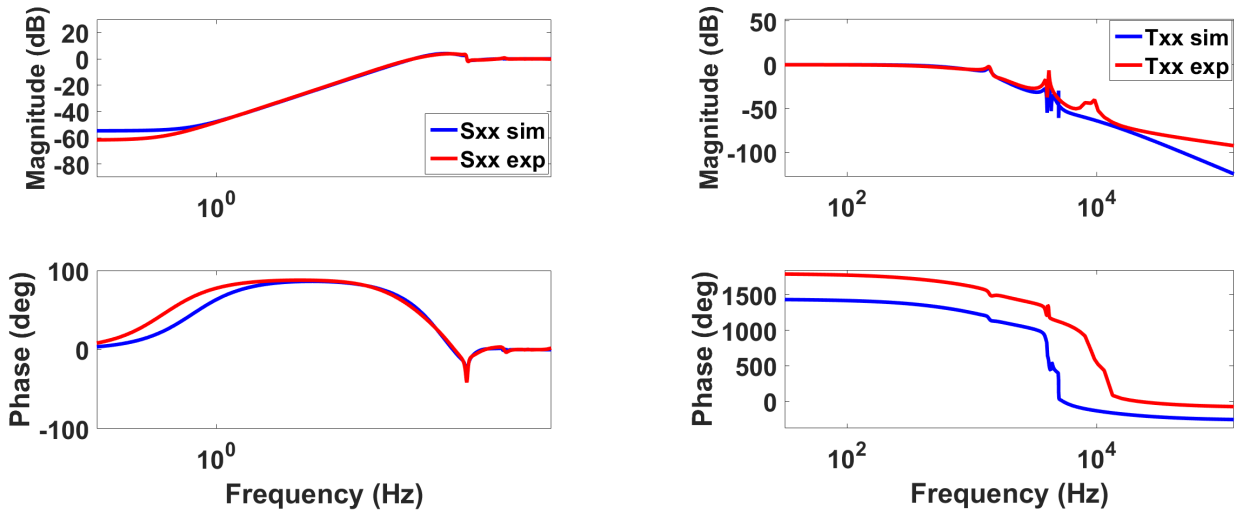

(a) (b)

Figure 3.33: Comparing the design and experimental closed loop transfer function, (a) Bode plot of $S_{xx,sim}$ and $S_{xx,exp}$, and (b) Bode plot of $T_{xx,sim}$ and $T_{xx,exp}$

Hz and $\omega_{bt\,exp} = 570$ Hz for simulation and experimental, respectively.

Similarly, for YY-stage the closed loop transfer function S_{yy} and T_{yy} are identified from experimental data and compared to the corresponding design transfer functions in Figure 3.34a, and Figure 3.34b, respectively. The bode plot of experimental S_{yy} and T_{yy} matches with design transfer functions quiet well. The bandwidth based on the S transfer function, gives $\omega_{b\,sim} = 200$ Hz and $\omega_{b\,exp} = 204$ Hz for simulation and experimental, respectively. The bandwidth based on T transfer function are $\omega_{bt\,sim} = 750$ Hz and $\omega_{bt\,exp} = 900$ Hz for simulation and experimental, respectively.

Similarly, for ZZ-stage the closed loop transfer function S_{zz} and T_{zz} are identified from experimental data and compared to the corresponding design transfer functions in Figure 3.35a, and Figure 3.35b, respectively. The bode plot of experimental S_{zz} and T_{zz} matches well with design transfer functions quiet. The bandwidth based on the S transfer function, gives $\omega_{b\,sim} = 102$ Hz and $\omega_{b\,exp} = 114$ Hz for simulation and experimental, respectively. The bandwidth based on T transfer function are $\omega_{bt\,sim} = 224$ Hz and $\omega_{bt\,exp} = 180$ Hz for simulation and experimental, respectively.

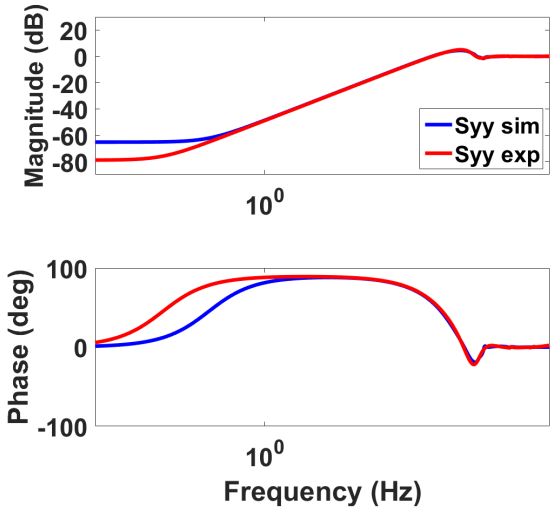

(a)

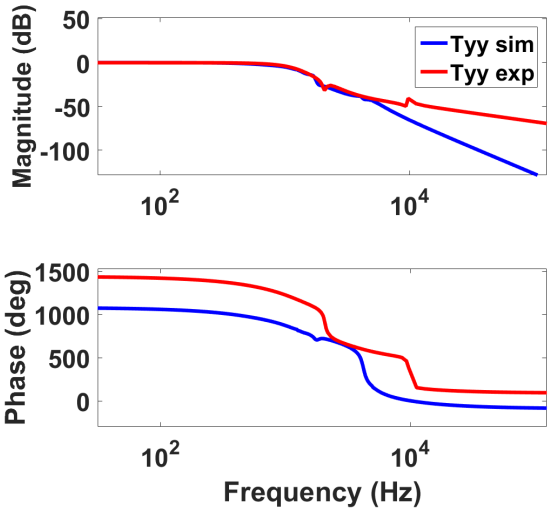

(b)

Figure 3.34: Comparing the design and experimental closed loop transfer function, (a) Bode plot of $S_{yy,sim}$ and $S_{yy,exp}$, and (b) Bode plot of $T_{yy,sim}$ and $T_{yy,exp}$

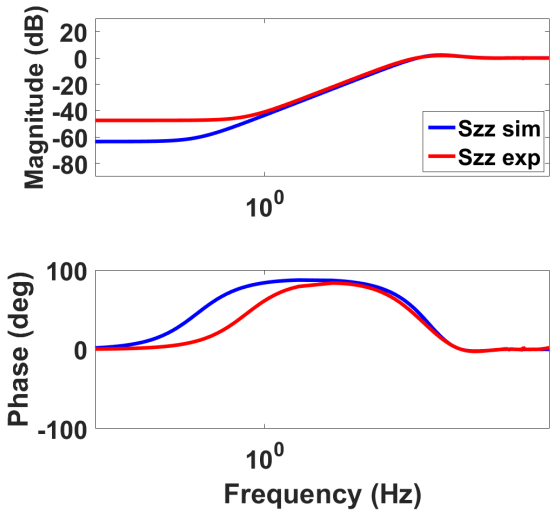

(a)

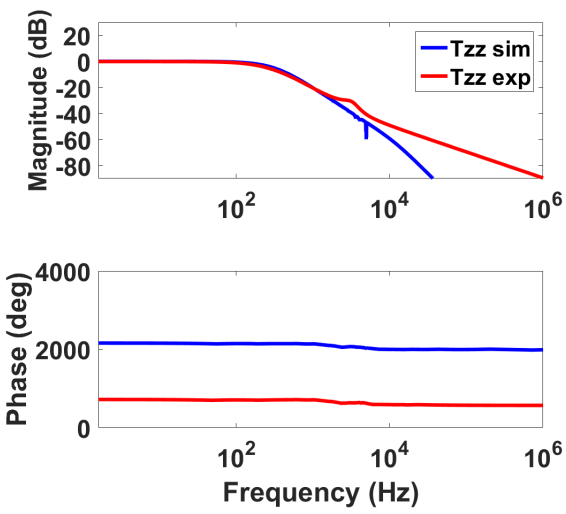

(b)

Figure 3.35: Comparing the design and experimental closed loop transfer function, (a) Bode plot of $S_{zz,sim}$ and $S_{zz,exp}$, and (b) Bode plot of $T_{zz,sim}$ and $T_{zz,exp}$

3.2.2.3 Results

3.2.2.3.1 Tracking Results XX-stage and YY-stage tracking of a sine wave reference of amplitude 1000 nm and frequencies 100 Hz and 200 Hz are shown in Figure 3.36 and Figure 3.37, respectively. The H_∞ controllers for the scanning XY stages tracks the reference trajectory better and with less phase offset than baseline PID controllers. The X-stage and Y-stage closed loop tracking error is smaller than that observed with PID controllers. The XY stages are used to do the high-precision high-bandwidth scanning during X-ray imaging. So, it is important that the XY stage achieves best scanning performance.

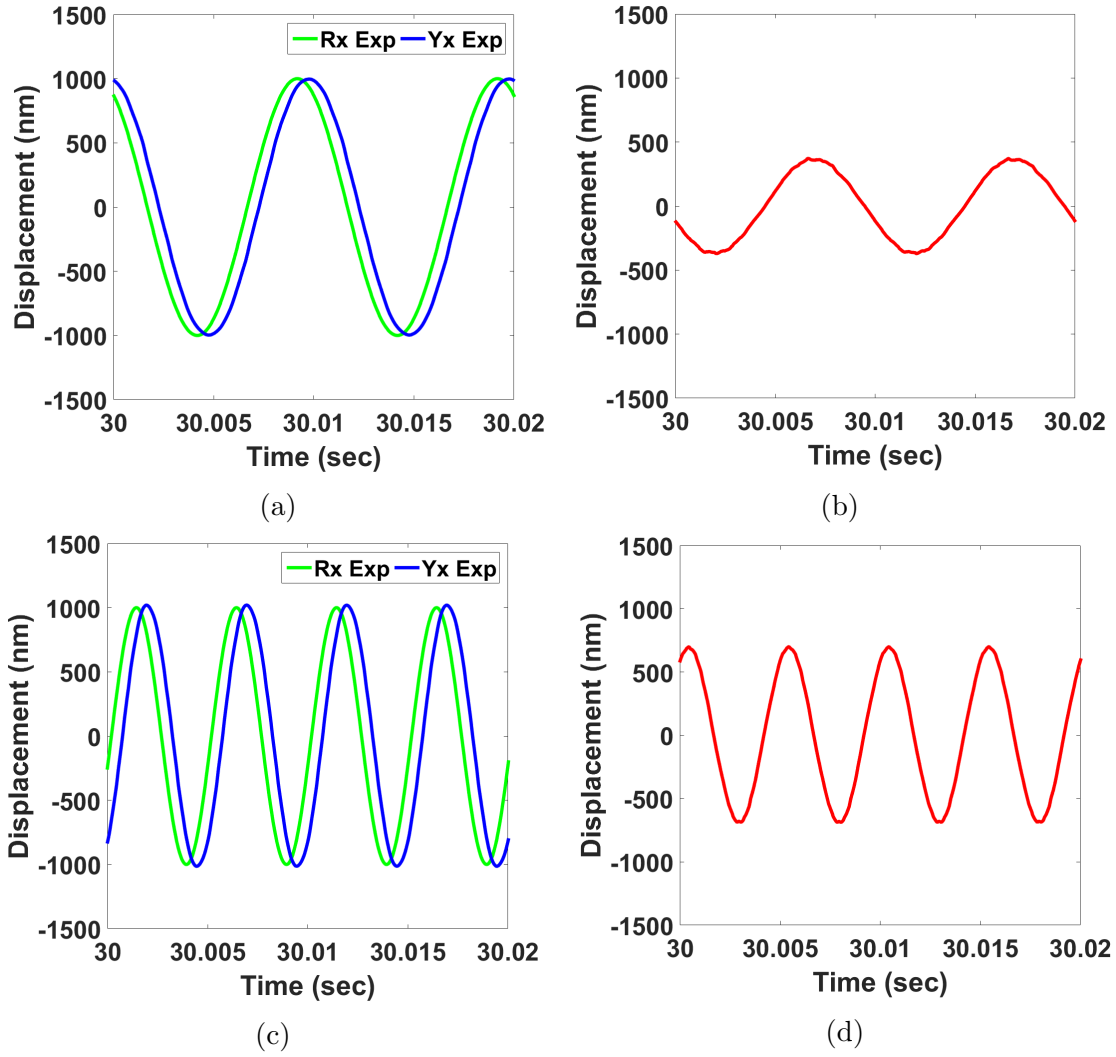

Figure 3.36: X-Stage sine wave reference tracking for 200 Hz −3 dB bandwidth H-infinity controller, (a) 1000 nm amplitude 100 Hz sine wave reference tracking, and (c) 1000 nm amplitude 200 Hz sine wave reference tracking. (b) and (d) are the corresponding tracking error.

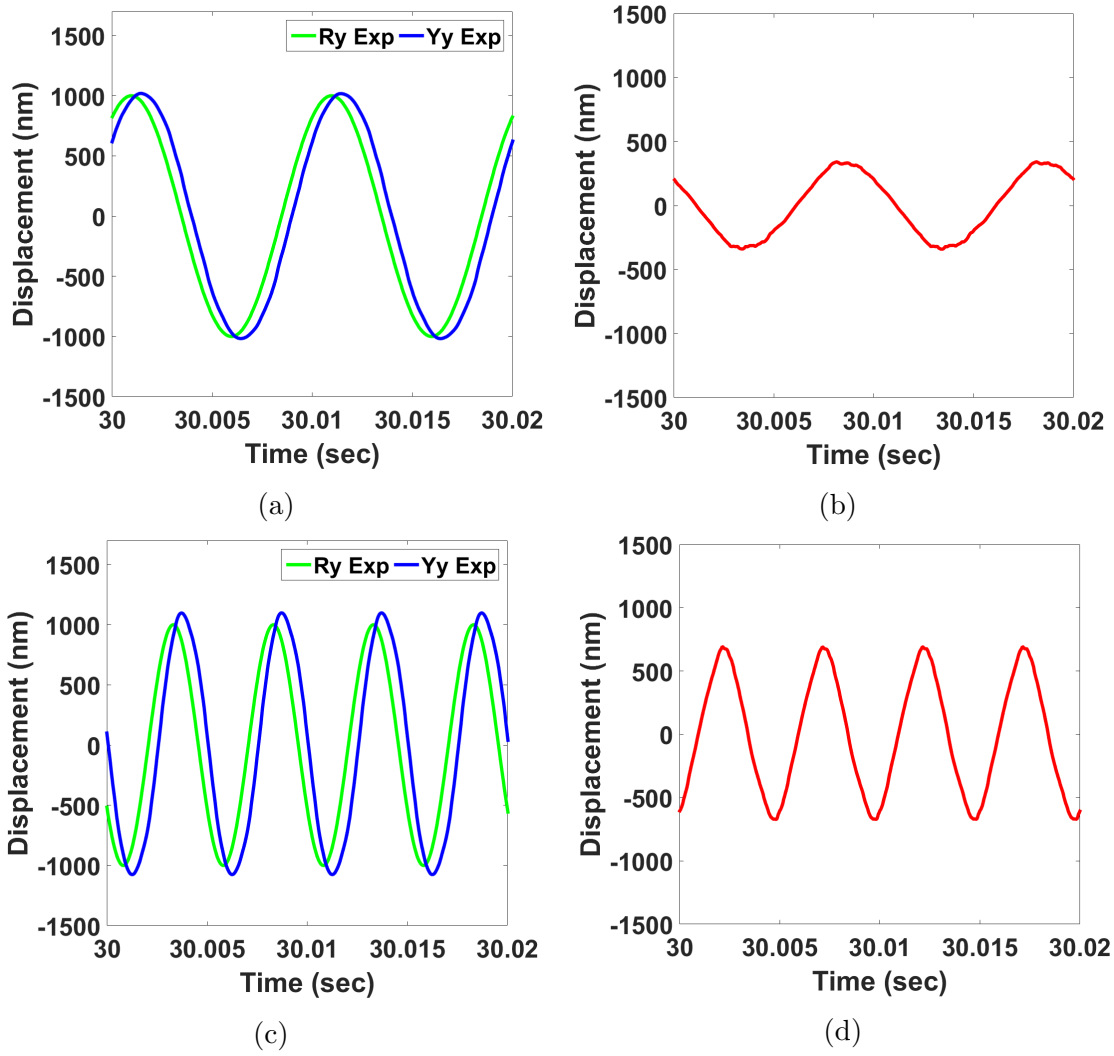

Figure 3.37: Y-Stage sine wave reference tracking for 200 Hz −3 dB bandwidth H-infinity controller, (a) 1000 nm amplitude 100 Hz sine wave reference tracking, and (c) 1000 nm amplitude 200 Hz sine wave reference tracking. (b) and (d) are the corresponding tracking error.

3.2.2.3.2 Positioning Resolution Results Noise experiment (as explained before) was performed on X, Y, and Z optics scanning stages to quantify the positioning resolution in closed-loop. Figure 3.38, Figure 3.39, and Figure 3.40 shows the noise histogram of the closed loop XX, YY, and ZZ stage displacements for the H_∞ controllers in diagonal form. Compared to the open loop the H_∞ controllers have much better $3\,\sigma$ resolution. For the XX, YY, and ZZ stage the closed loop $3\,\sigma$ resolution are 1.9 nm, 1.4 nm, and 1.9 nm, respectively, resulting into an improvement of 194%, 188%, 193% over open loop. This controllers were designed for high bandwidth tracking of custom trajectories. So, the resolution achieved in closed loop is approximately the same as PID controllers. X-ray microscope optics scanning stage positioning resolution of $1-2$ nm is sufficient to achieve high X-Ray image spatial resolution. Results showing X-Ray images with good spatial resolution, which were imaged at high imaging speed is shown in the next section.

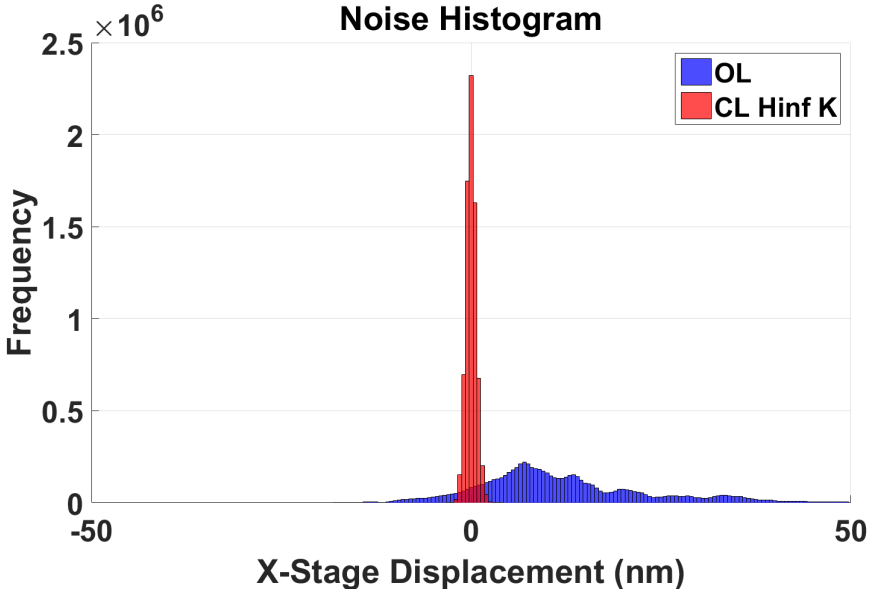

Figure 3.38: X-stage closed-loop noise histogram with a 200 Hz bandwidth H-infinity controller giving a resolution of approx 1.9 nm. Whereas the open loop resolution is approx 33 nm.

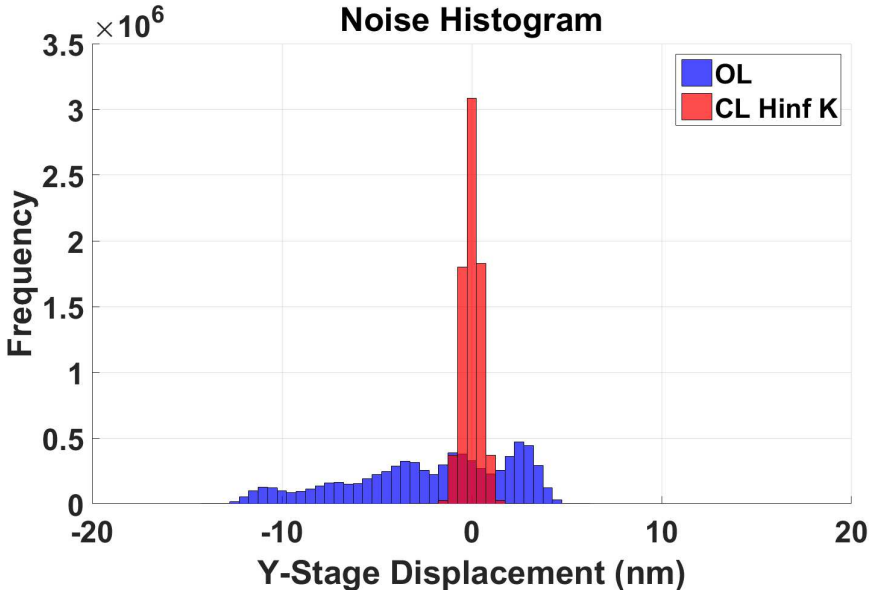

Figure 3.39: Y-stage closed-loop noise histogram with a 200 Hz bandwidth H-infinity controller giving a resolution of approx 1.4 nm. Whereas the open loop resolution is approx 12 nm.

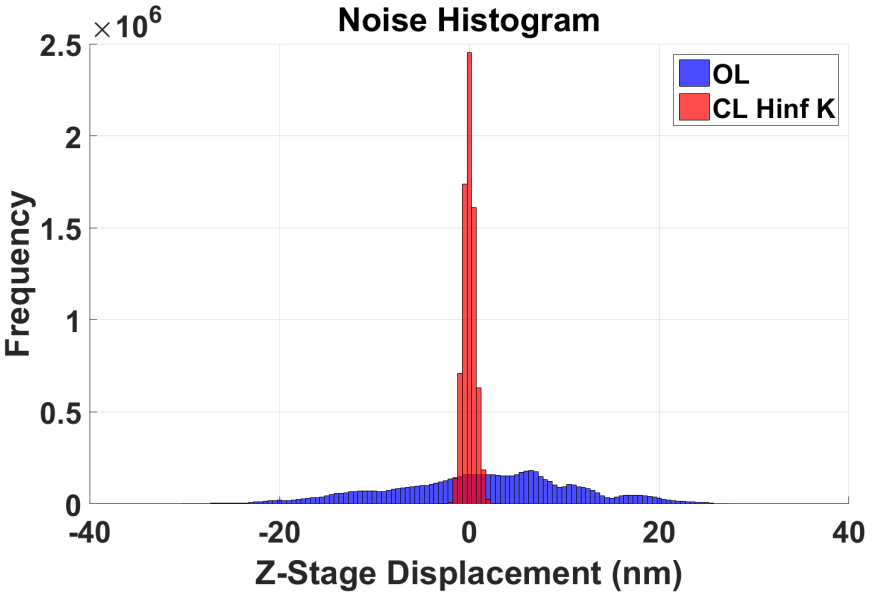

Figure 3.40: Z-stage closed-loop noise histogram with a 113 Hz bandwidth H-infinity controller giving a resolution of approx 1.9 nm. Whereas the open loop resolution is approx 29 nm.

3.3 X-ray Imaging with Velociprobe

3.3.1 Step Scan X-ray Imaging Results

In step scan X-ray imaging to cover a predefined region in raster scan trajectory, first the X-ray spot is focused on to the sample at point A and the corresponding diffraction pattern is collected at the detector downstream of the sample. Then the X-ray spot is moved to the second location with a predefined horizontal and\or vertical step size. An overhead time is given to the optics scanning stages to reach to the second position (about 150 ms) before another diffraction pattern is recorded for a predefined exposure time (30 ms). Only then the optics scanning stages move the X-ray spot the third location and so on.

The results showcased here is for the designed H_∞ controllers applied to the PI XYZ stages. H_∞ controllers with bandwidth around 150 Hz were used for these X-ray imaging experiments. Figure 3.41 shows the X-ray images of a $3\,\mu m \times 3\,\mu m$ area on a Siemens Star pattern through the step scan technique in three modes: (a) zone plate only and open loop mode, (b) zone plate only and closed loop mode, and (c) differential and closed loop mode, respectively. In all modes the sample stage remains fixed. Each of the step scans took 18.9 minutes. With previously existing methods at APS this scans took around 2.52 hours. So, that is approximately 8 times improvement of step scan imaging bandwidth achieved through the use of NI control hardware.

In the zone plate only and open loop mode, the sample stage remains fixed, the zone plate optics scanning stage scans the predefined area on the sample following raster scan trajectory in open loop (no controllers engaged). The absorption image (diffraction pattern collected as intensity by the detector) and phase change image (recovered by solving the "phase problem") obtained in this mode is shown in Figure 3.41a and Figure 3.41b. Clearly, the images are skewed, the circular patterns are appearing like ellipsoids, the straight features are not that straight and there is edge ambiguity of the straight features. Figure 3.41c and Figure 3.41d are the absorption and phase change images for zone plate only and closed loop mode. Only difference from the previous mode is that the H_∞ controllers are engaged. The X-ray image is much better with circular patterns, straight features and with some edge ambiguity still present. The third mode (differential and closed loop mode) is where the zone plate optics stages tracks both reference trajectory and the sample stages (to counter the drift of sample stages) in closed loop with the H_∞ controllers. Figure 3.41e and Figure 3.41f are absorption and phase change images for the differential mode and is much better than that observed with the other two cases.

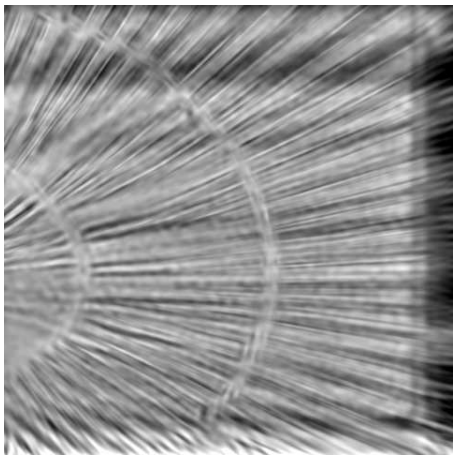

(a) Absorption

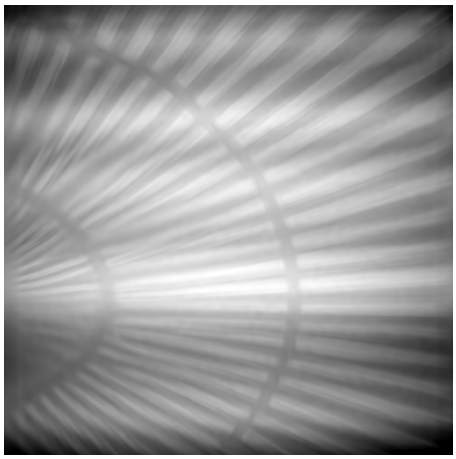

(b) Phase

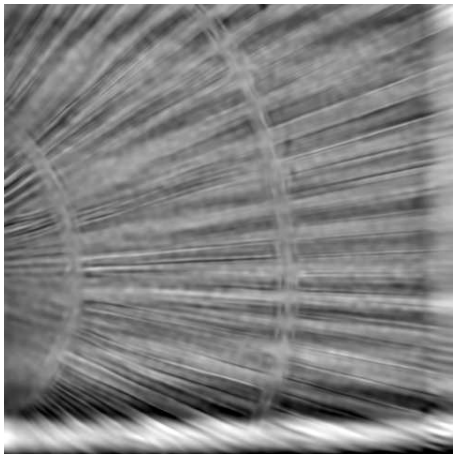

(c) Absorption

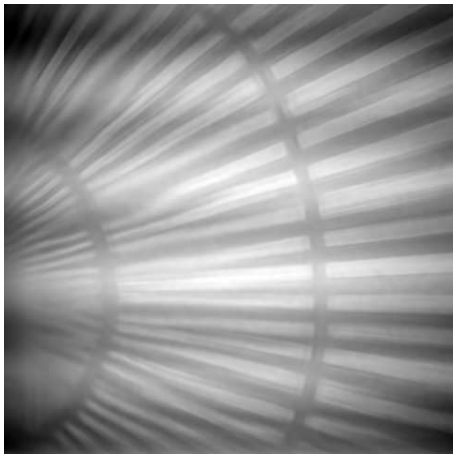

(d) Phase

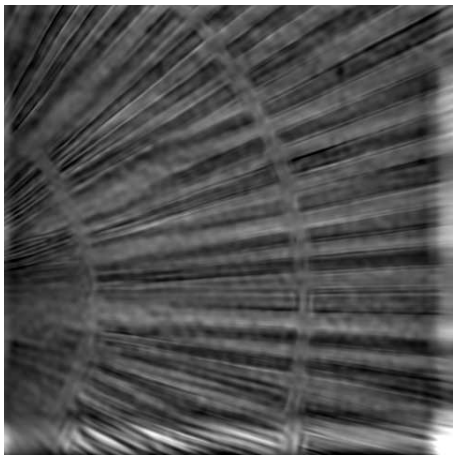

(e) Absorption

(f) Phase

Figure 3.41: Step scan image of a Siemens Star pattern by (a) and (b) zone plate only and open loop mode, (c) and (d) zone plate only and closed loop mode with the H_∞ controllers in diagonal, and (e) and (f) differential mode and closed loop mode with the H_∞ controllers in diagonal. (b), (d), and (f) are the phase change of the X-ray recovered using the Extended Ptychographic Iterative Engine (ePIE).

3.3.2 Flyscan X-ray Imaging Results

In this section we showcase the X-ray images obtained by flyscan imaging technique. In the flyscan technique, the optics scanning stages continuously tracked a square snake scan trajectory to scan the X-ray spot and cover the region of interest of the sample while the diffraction patterns were simultaneously collected at the area detector downstream of the sample. The square snake scan trajectory is a custom trajectory generated in the FPGA (for the purpose of flyscan) which has a custom scanning speed directly tied to the detector trigger frequency, size of scan area, horizontal and vertical step size, and probe overlap duty cycle (in percentage).

The flyscan technique enabled the scanning of a $1\,\mu m \times 1\,\mu m$ area in 0.01 seconds compared to the 2.1 minutes required for the step scan to scan the same area, which is a 12600 times improvement over step scan. Flyscan also resulted into an overall improvement of 100800 times over the previous step scan performance at the APS.

The X-ray images in Figure 3.42, Figure 3.43, Figure 3.44 and Figure 3.45 shows the comparison of the PID and H_∞ controllers in flyscan technique with detector trigger frequency being 500 Hz, 1 kHz, 2 kHz, and 3 kHz. All the flyscans were done in zone plate only and closed loop mode, with the sample stage being fixed all the time. For each experiment we are showing the absorption image (diffraction pattern or intensity collected the area detector) and the phase change image (recovered by solving "phase problem"). We can see that overall the performance of PID and H_∞ controller in terms of X-ray images is very similar. The reason behind this sources from the combined effect of the custom square snake scan trajectory and ptychographic X-ray imaging technique. First of all, the square snake scan trajectory has long segments $(1 - 9\,\mu m)$ of straight line and with small vertical jumps to the next line at the end of each line. This makes it very easy for all types controllers to track. Secondly, in the ptychographic imaging technique (explained in Chapter 2) the probes have horizontal and vertical overlap of $(30\% - 70\%)$ which results in lot of redundant information. Also the detector trigger signal (square wave generated in the FPGA) is chosen so as to have a very high duty cycle (up to 99.5%), which interprets as the detector collecting data almost all of the time. Custom trajectory, large probe overlap and continuous data collection by the detector helps the ePIE technique to work good for both PID and H_∞ controllers. The benefit of H_∞ controller will be emphasized in experiments where higher bandwidth requirement is needed, trajectory is not made up of just straight lines but has lot of curves like spiral, circular, and Lissajous trajectory. Even then the images obtained using H_∞ controllers are sharper than that of the PID controllers, specifically looking at the faster detector triggering frequency experiments.

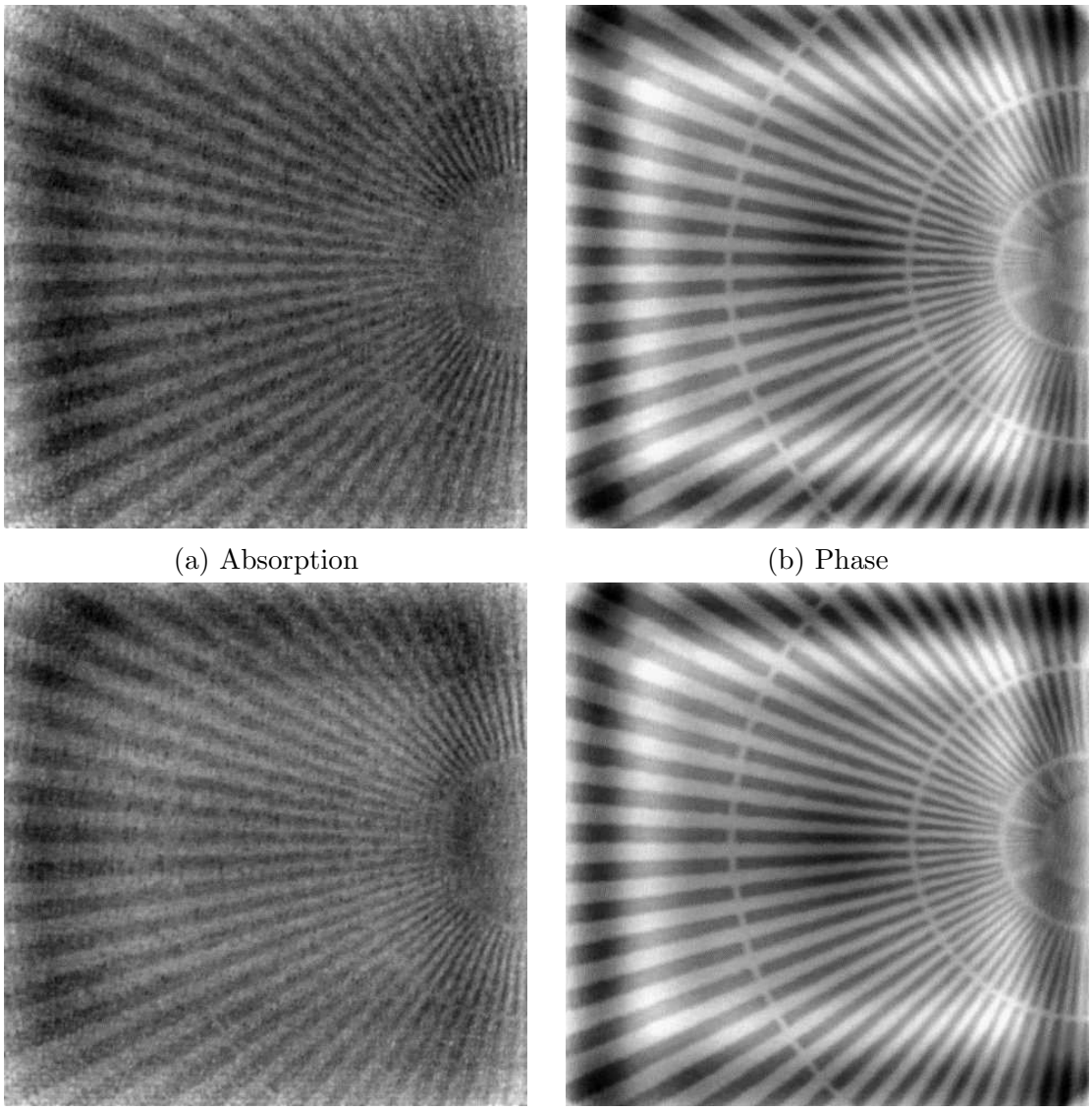

(a) Absorption (b) Phase

(c) Absorption (d) Phase

Figure 3.42: Flyscan X-ray image of a Siemens Star in Zone Plate Only Mode in closed loop. The detector trigger frequency is 500 Hz. (a) and (b) PID controller, and (c) and (d) H_∞ controller.

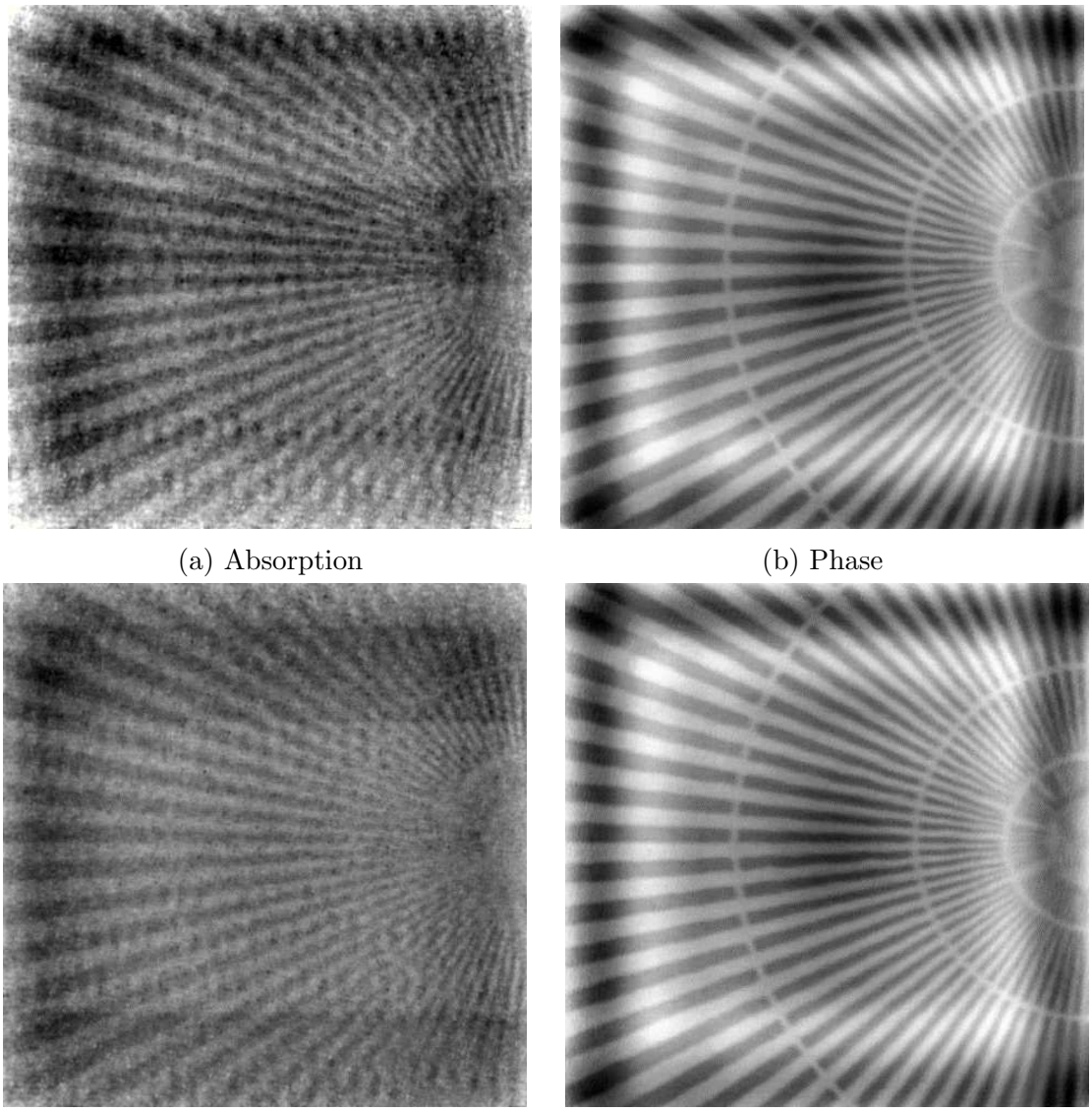

(a) Absorption (b) Phase

(c) Absorption (d) Phase

Figure 3.43: Flyscan X-ray image of a Siemens Star in Zone Plate Only Mode in closed loop. The detector trigger frequency is 1 kHz. (a) and (b) PID controller, and (c) and (d) H_∞ controller.

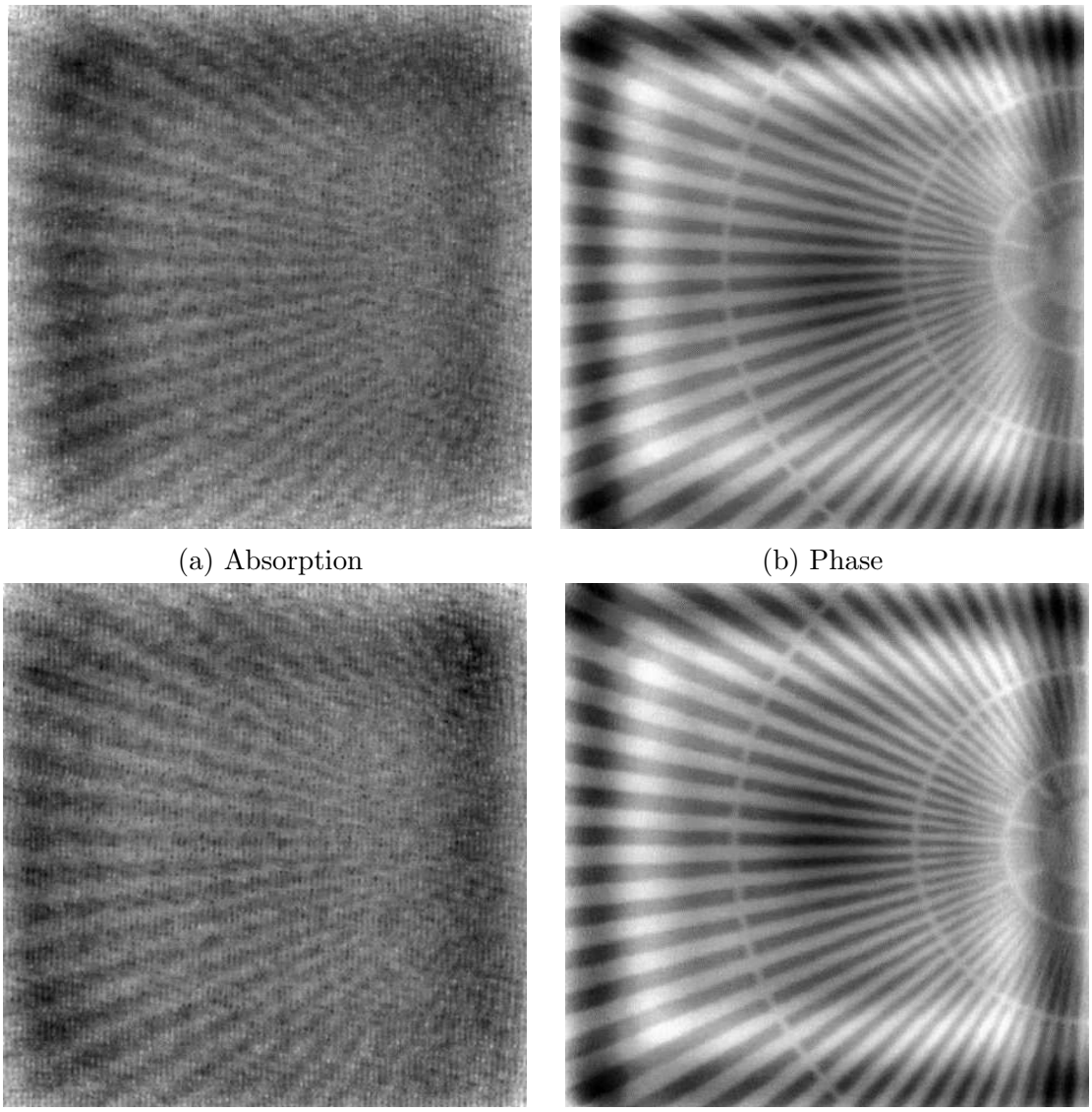

(a) Absorption (b) Phase

(c) Absorption (d) Phase

Figure 3.44: Flyscan X-ray image of a Siemens Star in Zone Plate Only Mode in closed loop. The detector trigger frequency is 2 kHz. (a) and (b) PID controller, and (c) and (d) H_∞ controller.

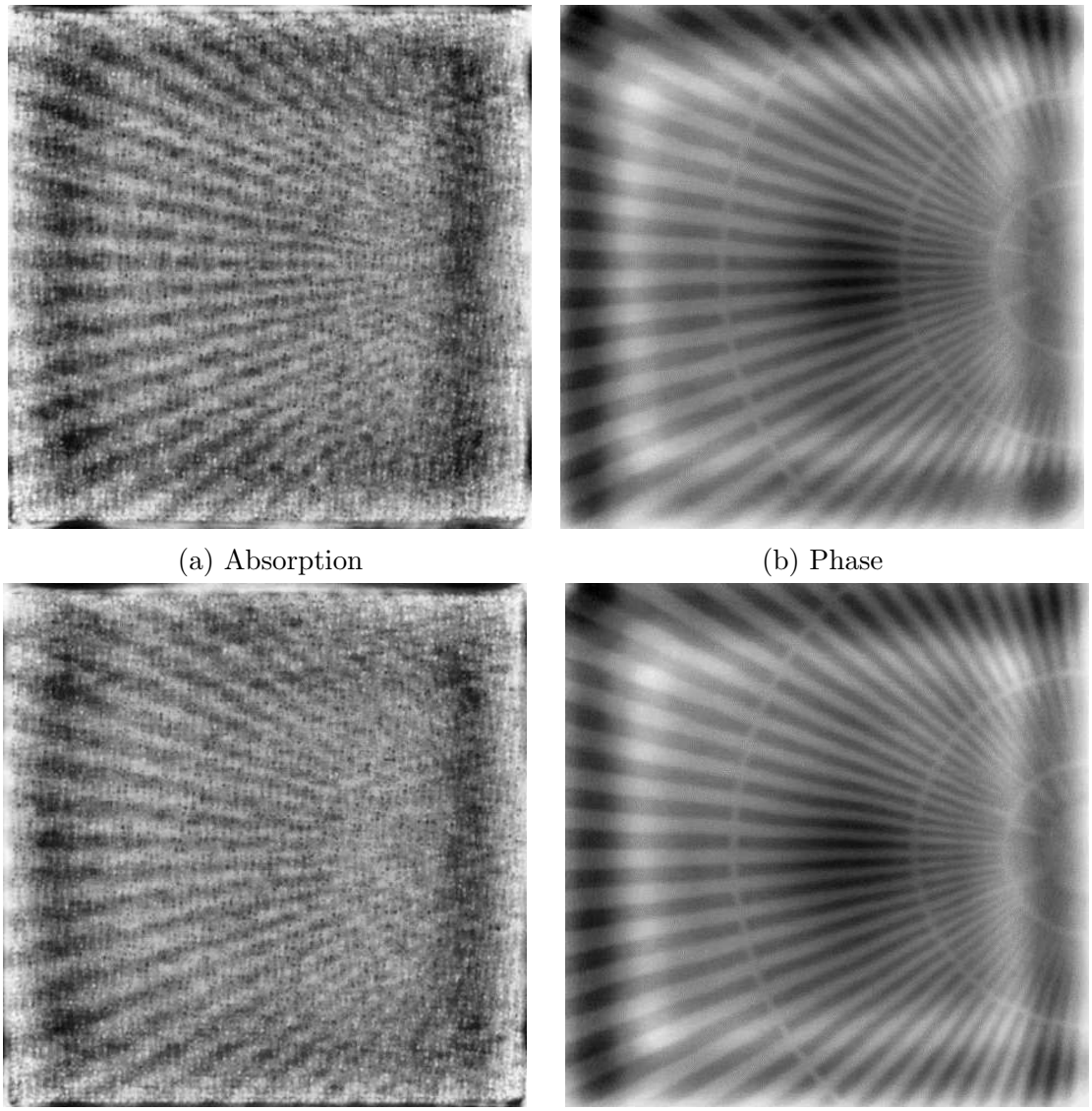

(a) Absorption (b) Phase

(c) Absorption (d) Phase

Figure 3.45: Flyscan X-ray image of a Siemens Star in Zone Plate Only Mode in closed loop. The detector trigger frequency is 3 kHz. (a) and (b) PID controller, and (c) and (d) H_∞ controller.

3.4 Impact on X-ray Microscopy

The work presented in this chapter covering control design, fast and robust optimal control, custom trajectory generation will have significant impact on the X-ray microscopy. Some case are as follows:

- In an imaging experiment where a target area of $1\,mm \times 1\,mm$ of a 10 nm technology Intel chip is being scanned in 2D with 100 nm diameter X-ray probe and 50 nm step size along both axes in the scanning plane, the total time required to do the scan would be 38.88 hours with flyscan imaging technique, custom square snake scan trajectory and robust optimal control presented here. This ptychogrphic flyscan would be done at 3 kHz detector trigger rate with $4.2e8$ number of exposures along a square snake scan pattern. With the step scan imaging technique using traditional raster scan pattern and robust optimal control presented here this scan would have taken over 55 years. And with previous performance at APS the time required would be 440 years. In short, experiments that were simply not possible before has just become fairly easy.

- To do X-ray tomography of the same 10 nm technology Intel chip with 180 projections to cover 180 degrees, the time required for the whole experiment will be much more but possible if we use the combination of flyscan, custom trajectory and robust optimal control.

- Image reconstruction errors like image feature ambiguity, stitching error would decrease significantly.

CHAPTER 4

COUNTERING SENSOR DRIFT IN X-RAY MICROSCOPE

In X-ray microscopy it is imperative that the relative position between the optics stage, that carries the X-ray focusing optics, and the sample stage follow a certain trajectory while either the optics or sample stage is being scanned. Main challenges in achieving this requirement include - open loop drift, environmental disturbance, measurement noise, sensor drift, and control hardware limit. The state-of-the-art in X-ray microscopy at APS at ANL (as showcased in chapter 3) features an H_∞ control architecture applied to only the optics stage (Zone Plate Stage Only Mode) or both the optics and sample stage (Differential Mode), achieving the objectives of large tracking bandwidth over 200 Hz (for X, Y, and Z stages), good positioning resolution on the order of $1-2$ nm, rejection of environmental disturbance, attenuation of measurement noise, good X-ray diffraction image resolution and significantly better imaging bandwidth. However, an unaddressed issue in our existing robust control design is that the sensors and the fixtures that hold the sensors drift with time due to changing air temperature in the APS beamline. This affects the relative position between the focusing optics and sample resulting into imaging artifacts and reduced image resolution. In this chapter, we demonstrate the rejection of the sensor drift by directly measuring the displacement of the sensor with respect to the global reference frame. Both the measured sensor displacement (i.e. sensor drift) and optics stage displacement are incorporated in the H_∞ optimal control architecture to achieve the objective of drift rejection. This will in turn improve the X-ray image resolution and reduce image artifacts.

Figure 4.1 shows the nanopositioning optics stages of the Velociprobe X-ray microscope on a table setup before being assembled on to the Velociprobe coarse granite stages at the APS beamline (Figure 3.1). The PI 3DOF XYZ nanopositioning optics stage is bolted to an Aluminum alloy reference frame. All the interferometric sensor heads, that are being used for high-precision measurement of the optics and sample stage displacement are held on to Aluminum alloy fixtures at predesignated locations on the reference frame.

Figure 4.2 shows varying air temperature at Sector-2 experimental hutch and the Velociprobe sample stage temperature measured for over 24 hours at APS beamline. The

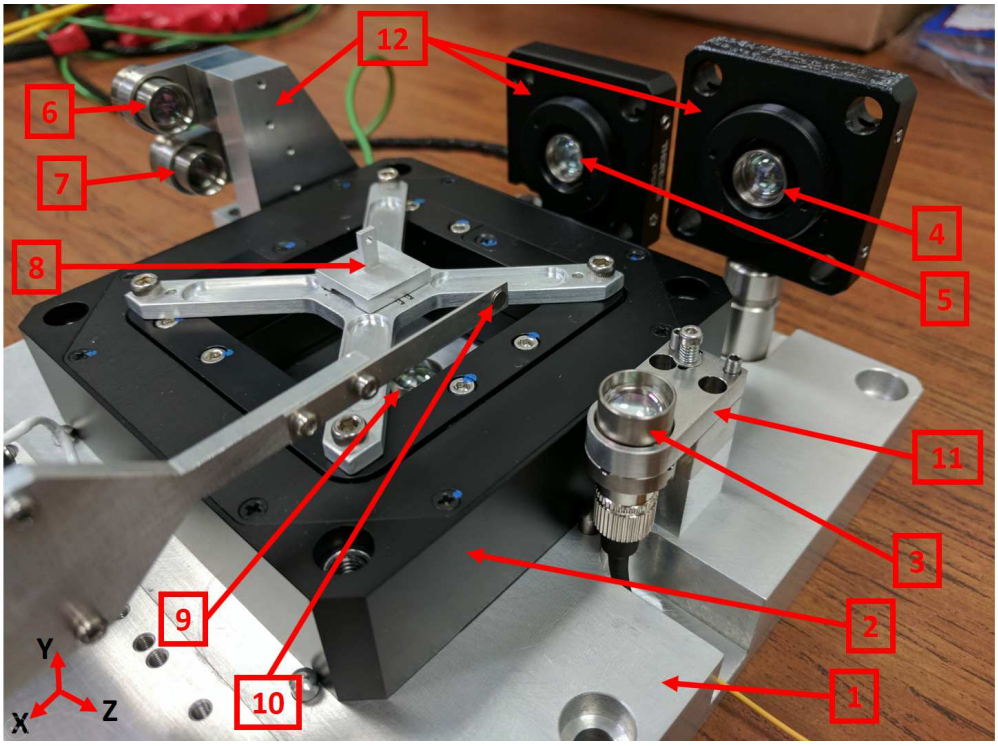

Figure 4.1: Velociprobe fine scanning optics stage assembly on a table, before the final assembly in an inverted orientation under the granite gantry shown in Figure 3.1. In details, 1 = reference frame, 2 = PI parallel kinematics XYZ nanopositioning stages, 3 = sensor head sample Y axis, 4 = sensor head sample X axis, 5 = sensor head optics X axis, 6 = sensor head sample Z axis, 7 = sensor head optics Z axis, 8 = zone plate optics kinematic holder, 9 = sensor head optics Y axis, 10 = order sorting aperture, and 11 and 12 = Aluminum alloy fixtures that hold the sensors. The Attocube Laser interferometric sensor heads are strategically positioned so as to measure the XYZ optics and sample stage displacement. The zone plate optics holder is attached kinematically on the cross-shaped Aluminum alloy fixture, which is in turn bolted on to the PI stage. For displacement measurement of the optics stage, mirrors (not shown here) are glued on the zone plate holder, so that the laser coming out of the standard Attocube focusing sensor heads can reflect back to the sensor heads.

maximum variation of the air and sample stage temperature over 24 hours is 0.5 and 0.25 degree Celsius, respectively. As mentioned before, the optics stage, the sample stage, optics and sample stage fixtures for holding zone plate optics, sample, Laser interferometric sensor heads are mostly made with Aluminum alloy. This means with the varying temperature cycle during operation at APS beamline all these components, which are critical for stage stability, positioning resolution, and image spatial resolution, would thermally drift due to expansion and contraction of Aluminum alloy. For example, a 100 mm long Aluminum alloy section would thermally drift by approximately 600 nm in the 24−hour time frame. So, both the high-precision optics and the sample stage sensors would drift by couple hundred nanometers during any given day. As mentioned at the beginning, the relative position between the optics stage and the sample stage should follow a predefined trajectory with nm to sub-nm level positioning resolution if we want to achieve the highest quality X-ray image with the good spatial resolution. The thermal drift that is observed in the sensor fixtures can very easily deteriorate the X-ray image quality by introducing relative positioning error between the optics and sample stage resulting in image ambiguity, image stitching error, and other imaging artifacts.

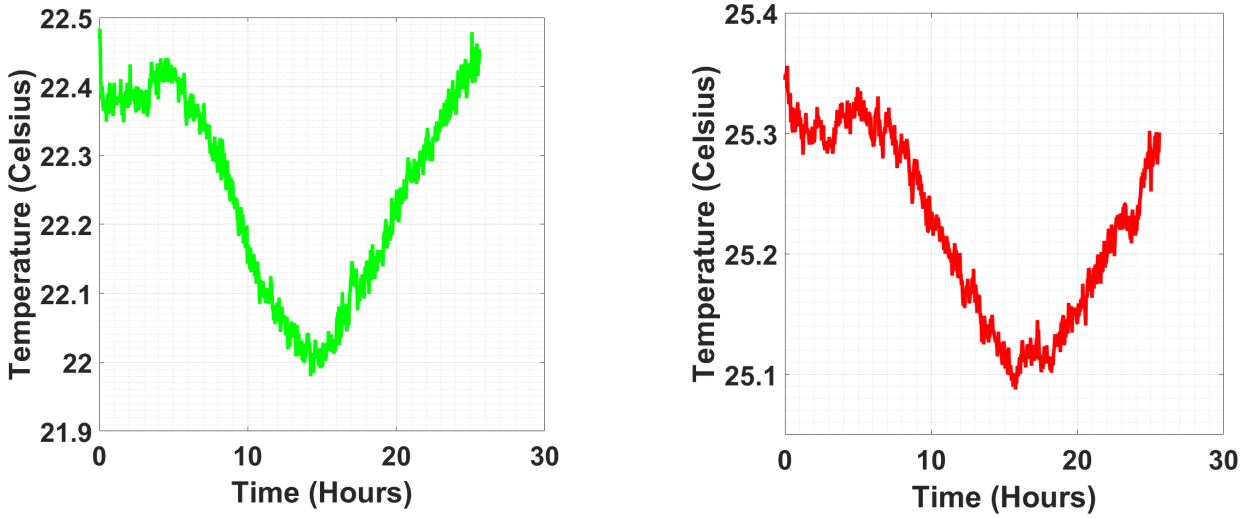

(a) (b)

Figure 4.2: Temperature log of over 24 hour recorded at Sector-2 experimental hutch at the APS beamline. (a) The air temperature in the experimental hutch, and (b) the sample stage temperature measured at the base.

All the work that has been done to enhance the performance of X-ray microscope positioning stages at the APS [12], [5], and [4], and in the Chapter 3 addresses objectives of actuator drift minimization, robust stability, large tracking bandwidth, good positioning resolution,

good disturbance rejection and adequate noise attenuation in real-time. There is no existing mechanism of countering the effect of thermal drift of the sensors themselves with respect to the global reference frame. The existing literature, regarding the other synchrotron light sources, covers some methods (linear, non-linear drift model, averaging, multiple exposures to increase SNR) to counter actuator drift in the post-processing part of X-ray imaging, but does not refer to the thermal drift of sensor.

In this chapter, we are presenting a technique that measures the sensor drift (for both optics and sample stages) in real time and incorporate the drift measurement into the optimal control problem to minimize the effect of the sensor drift on the optics stages scanning and eventually on the quality of the X-ray image. Also we explain fundamental limitations on achievable bandwidth that is imposed by the non-minimum phase zeros of our optics stage.

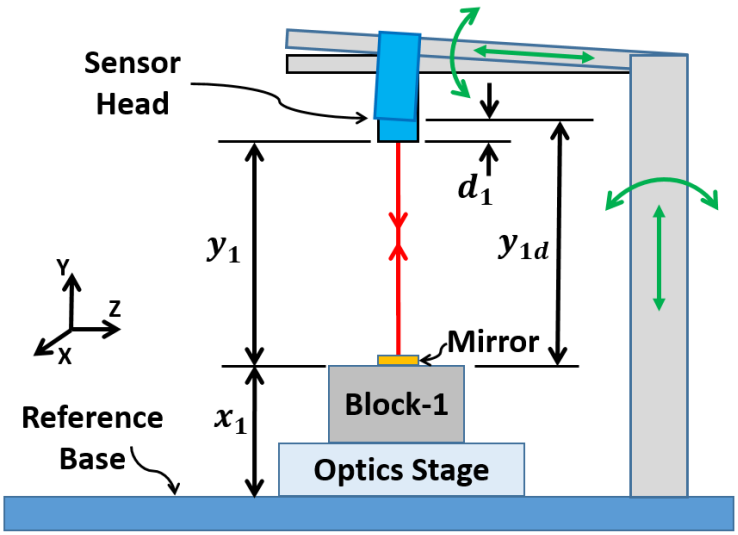

Figure 4.3: Schematic diagram showing the effect of thermal drift of the sensor fixtures on the measurement of X-ray microscope scanning stage displacement.

Figure 4.3 shows the schematic of the optics stage, optics stage laser interferometric sensor fixture and the thermal drift during operation. In the schematic, x_1 is the actual stage displacement with respect to the global reference frame, and y_1 is the measured displacement of the optics stage by the Laser interferometric sensor. Due to thermal drift of the Aluminum alloy sensor fixtures the sensor head itself drifts by a distance of d_1. This drift can be erroneously registered as the stage displacement by the sensor, giving the new measured displacement to be $y_{1d} = y_1 + d_1$. The corrective action of the feedback controller would actually move the optics stage by the amount of d_1 to wrong coordinates in space. Since, the zone plate optics is held on the optics stage, it will focus the X-ray beam in a different spot on

the sample downstream, away from the reference trajectory. This relative positioning error between the optics and sample stages will result in X-ray imaging artifacts, image stitching errors and reduce the achievable spatial image resolution. The alignment tolerance for the Attocube interferometric focusing sensor head that is used for this experiment is ± 2 degrees for a working distance up to 10 mm and smaller tolerance for larger working distances. So, the small angular rotation resulting from the thermal drift of the sensor fixtures will not take the sensor off alignment during X-ray imaging. We should remember that similar thermal drifts would affect the sample stages as well.

4.1 Drift Rejection Through Measurement

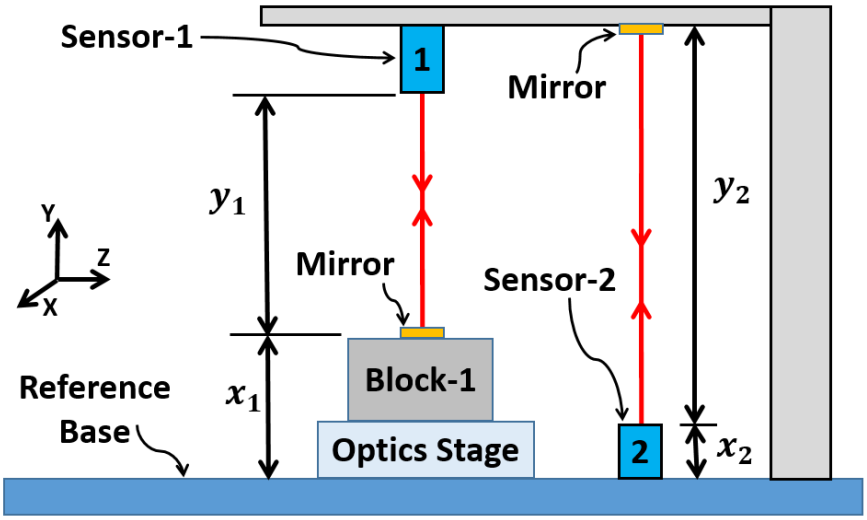

Figure 4.4: Schematic diagram showing the additional laser interferometer sensor introduced on the reference base to measure the sensor drift.

In this particular setup, two separate channels of the Laser interferometer sensor are being used to measure the optics stage displacement y_1 (with sensor-1) and the optics stage sensor-1 drift y_2 in real time (with sensor-2)(Figure 4.4). Although the above schematic shows absolute displacement y_1 and y_2 being measured by the sensors, actually the relative displacement is measured (since we are using a relative displacement sensor). That means from the start of the experiment we can observe the relative displacement of the stages and the relative displacement of the sensor fixture. The relative displacement of the sensor-1 fixture is defined as the drift d_1 of the sensor-1. This measured thermal drift d_1 is then incorporated in the optimal control algorithm. The control algorithm would ensure precise

positioning of the optics stage with respect to the global reference frame while remaining unaffected by the drifting sensor. The other closed-loop objectives of large tracking bandwidth, good positioning resolution, external disturbance rejection, measurement noise attenuation will also be achieved by the optimal control algorithm. We are only doing this experiment with optics stage (one axis only). But this experiment can be easily extended to optics XYZ stages and sample XYZ stages.

4.1.1 Device Description

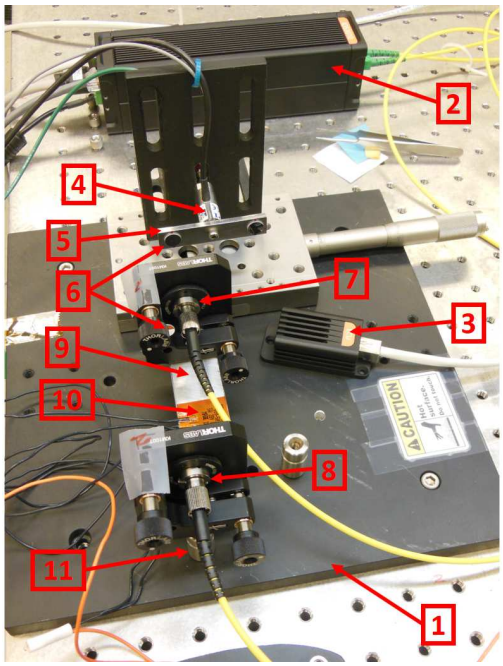

Figure 4.5: Experimental setup at APS used to prove the method of countering thermal drift of sensor in real time through measurement. Here, 1 = reference frame, 2 = Attocube IDS 3010 laser interferometric sensor, 3 = environmental compensation unit (ECU) for Attocube IDS 3010, 4 = PI piezo actuator, 5 = Aluminum alloy bar A, 6 = mirrors for reflecting Lasers sourcing from sensor heads, 7 = Sensor Head A, 8 = Sensor Head B, 9 = Aluminum alloy bar B, 10 = ultra thin flexible heat sheet, and 11 = Aluminum alloy post.

Figure 4.5 shows the experimental setup of the drift rejection experiment in a lab setup at APS. The Aluminum alloy bar A is attached at the end of a PI piezo actuator. When the piezo actuator is actuated it provides high-precision motion along single axis to the Aluminum bar A. In this experiment, we used Attocube Laser interferometric sensor to measure the displacement of the actuator (with sensor head A) and drift of sensor head A (with sensor head B) with high precision. A mirror is fitted on the Aluminum alloy bar A

for reflecting the Laser beam coming from the Sensor head A. Another mirror is fitted on the back of the sensor head A for reflecting the Laser beam coming from the Sensor head B. Sensor head A is screwed into a Thorlabs Aluminum alloy fixture, which in turn is positioned at the end of the horizontal Aluminum alloy bar B. The Aluminum alloy bar B is screwed on top of a small Aluminum alloy post. Sensor head B is screwed into another Thorlabs fixture, which is screwed on top of another small Aluminum post. Two ultra-thin flexible heat sheet was attached on the top and bottom surface of the Aluminum alloy bar B.

To replicate the thermal drift of sensors and sensor fixtures observed at the APS beamline Sector-2, the two heat sheets were turned ON/OFF for certain time periods. When the heaters are turned ON the Aluminum alloy bar B will extend due to increased temperature and when the heater is turned OFF the Aluminum alloy bar B will contract. In this way we can introduce thermal drift to the sensor head A, which will be measured by sensor head B.

4.1.2 System Setup

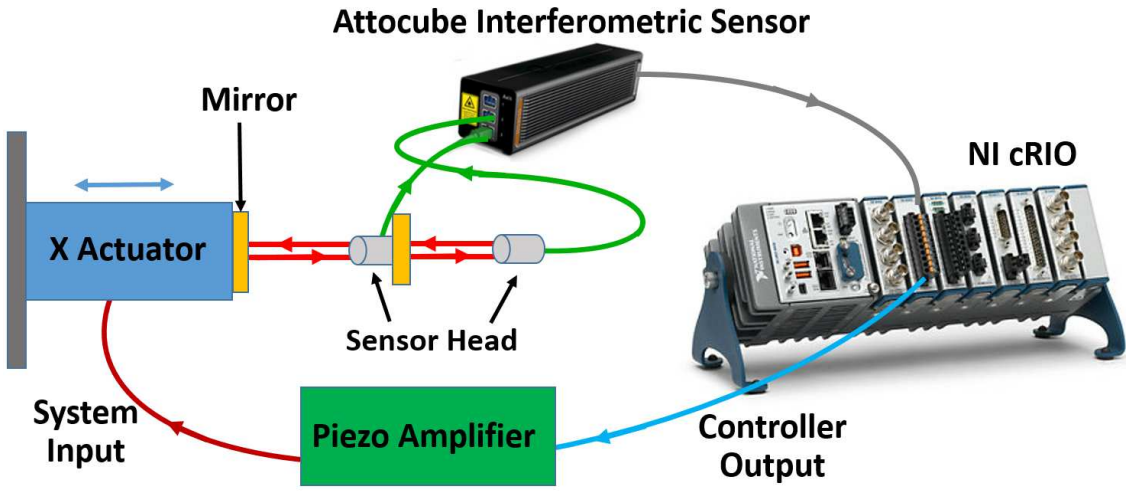

Figure 4.6: Schematic showing the closed-loop system layout for the thermal drift rejection experiment.

The system layout for the drift rejection experiment is shown in Figure 4.6. The displacement of the piezo actuator and the thermal drift of the sensor head A are measured by two separate channels of Attocube IDS interferometric sensor, namely the sensor head A and sensor head B, respectively. Attocube IDS sensor processes this raw displacement measurements and outputs two sets of quadrature signals. These quadrature signals are read through the 18 MHz NI-9402 DIO module directly into the FPGA in the NI control hardware. NI

control hardware used for this experiment consisted of the NI cRIO-9024 embedded real-time controller, paired with a NI cRIO-9118 chassis with an integral Virtex-5 $LX110$ FPGA running at 40 MHz rate. The reference trajectory generation, processing stage displacement information (sourcing from the Attocube sensors), running discrete feedback controller algorithm are done in the FPGA at 25 kHz sampling rate. The controller output voltage is provided by the NI-9263 analog output module. This voltage signal is amplified through a predefined scaling factor in the PI amplifier designed to work with the PI actuator. This is the feedback loop setup for this experiment.

4.1.3 System Identification

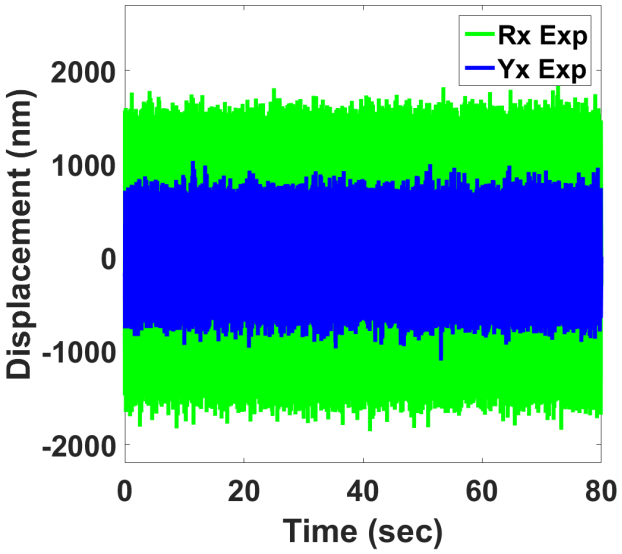

Figure 4.7: Band-limited uniform white noise (green) with 1500 nm amplitude is given as input to the PI actuator. The resulting actuator displacement (blue) is measured and used for system identification.

The PI piezo actuator dynamics was modeled using a frequency response based identification technique. A band-limited uniform white noise with amplitude 1500 nm was given as an input to the piezo actuator and the displacement was measured. A non-parametric frequency response function (FRF) was estimated from the time-domain input-output data. A fourth order Butterworth filter with cut-off frequency of 12 kHz was used to generate the band-limited uniform white noise from a source uniform full spectrum white noise. The frequency components in the input band-limited white noise signal covered our range of interest of 0 to 2 kHz, to make sure all the high frequency modes of the piezo actuator is also

excited. This will ensure the model generated from such input-output data represents all the significant dynamics up to the resonant frequency and at least one or two decades past the resonant frequency. The band-limited uniform white noise input and the measured output is shown in the Figure 4.7.

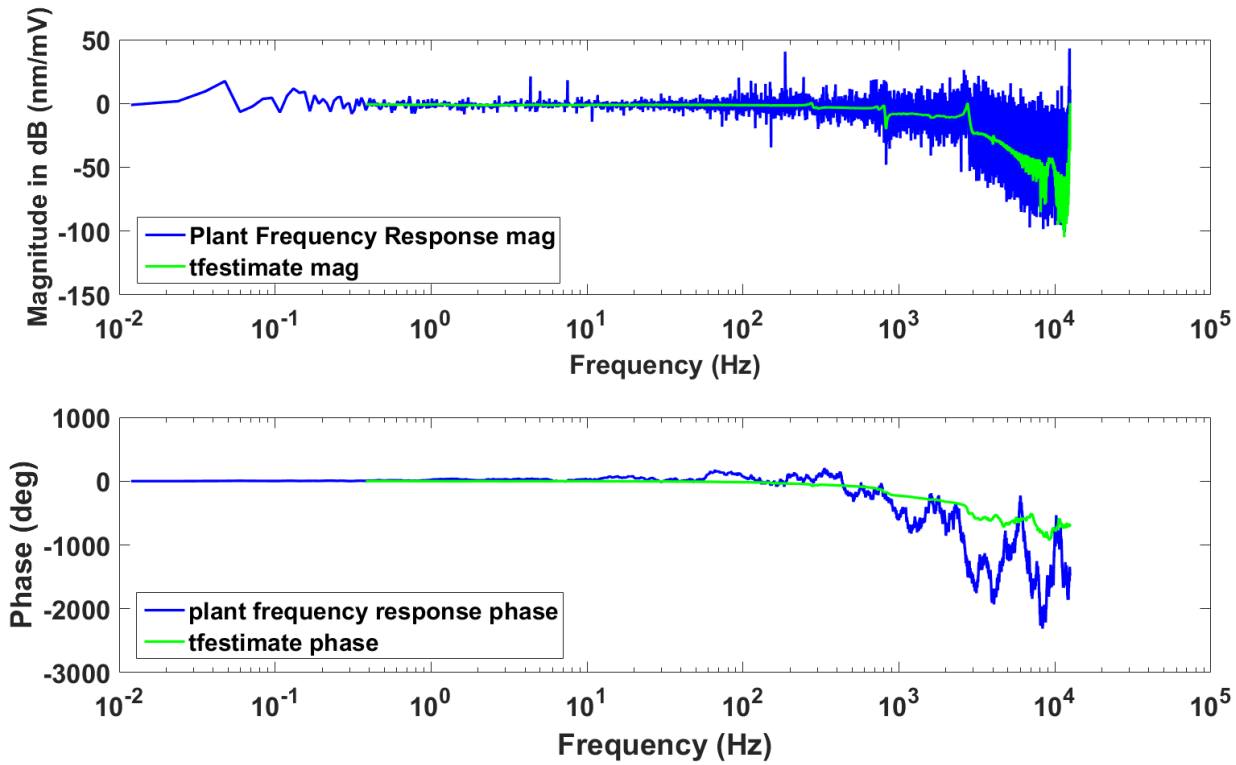

Figure 4.8: Comparison between the experimental plant frequency response (blue) and the transfer function estimate calculation (green).

Figure 4.8 shows the non-parametric transfer function estimate calculation for the experimental FRF. The first resonance peak is around 800 Hz. This non-parametric model is not suitable for designing control algorithms. A parametric model is fitted to this non-parametric model for this purpose.

4.1.4 Model Fitting

A parametric transfer function model G_1 (23^{rd} order, given in Appendix C) was fitted to the transfer function estimate calculation of the experimental FRF through curve fitting technique (Figure 4.9). This high order model for the actuator dynamics may exhibit behavior not consistent with the actual actuator dynamics. There can be unobservable and uncontrollable modes in this high order models. Design and implementation of controllers for

high order actuator model is complicated due to high computational cost, hardware resource usage and requiring higher sampling frequency during implementation.

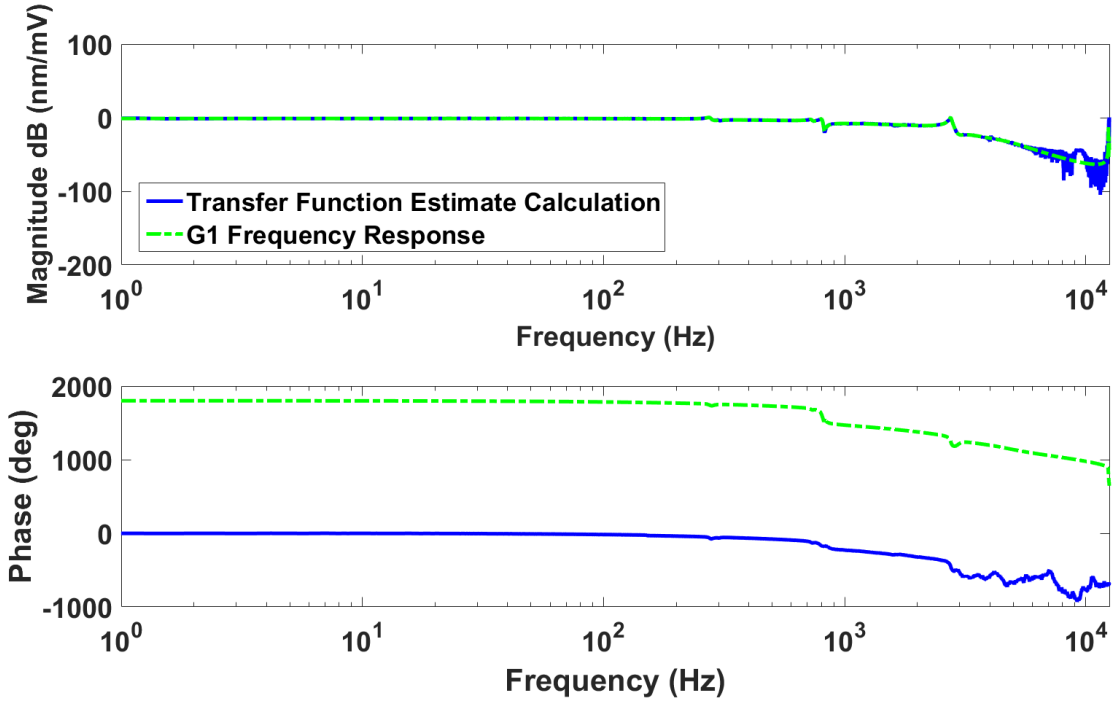

Figure 4.9: Comparison between the transfer function estimate calculation of the experimental FRF of the actuator and frequency response of the fitted 23^{rd} order model.

4.1.5 Balanced Realization and Model Reduction

We did a balanced truncation [38] of the 23^{rd} order model G_1 to get a reduced 18^{th} order model rG_1, given in Appendix C. Through balance realization the most observable and controllable states of the model are identified in hierarchical list. The states that are least observable and controllable are identified and removed from the model to get lower order model. Figure 4.10 shows the comparison between the actuators experimental FRF and the FRF of the reduced order actuator model. The first resonant peak is at 800 Hz for actuator model.

4.1.6 Model Verification

The step response of the actuator model G_1 and the reduced actuator model rG_1 is shown in the Figure 4.11. The actuator sensitivity is 0.88 nm/mV, which means for 1 mV input to the piezo actuator the undergoes a displacement of 0.88 nm. As a qualitative measure of

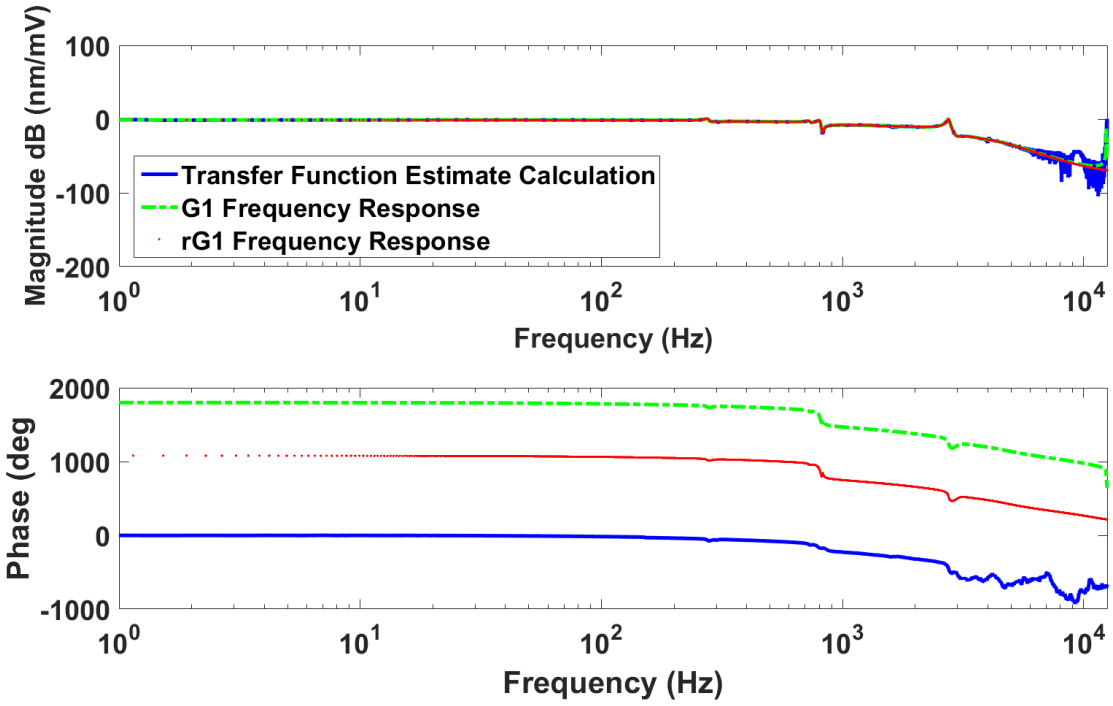

Figure 4.10: Comparison between the transfer function estimate calculation of the experimental FRF of the actuator, frequency response of the fitted 23^{rd} order model G_1 and reduced 18^{th} order model rG_1.

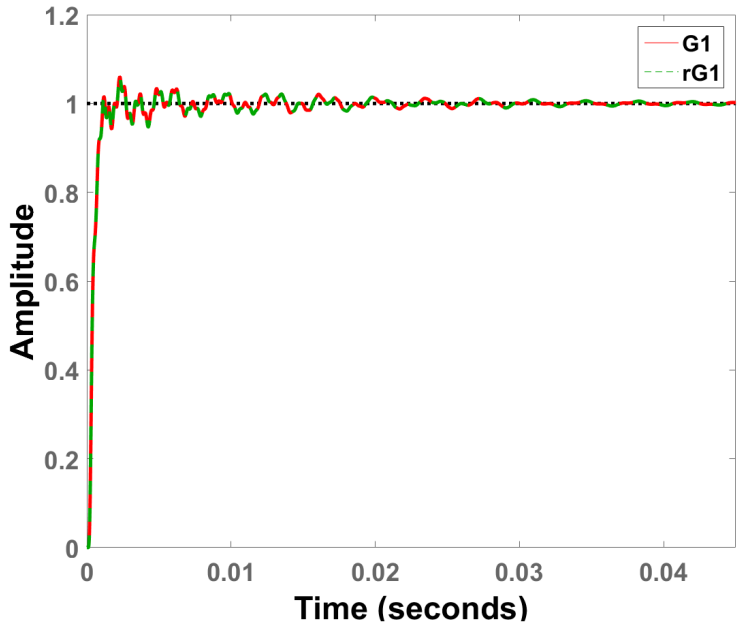

Figure 4.11: Comparison of the open loop step response (in simulation) of fitted plant model (23^{rd} order) and reduced plant model (18^{th} order).

the fit tracking of a sine wave of 1000 nm amplitude and frequency of 50 Hz is shown in the Figure 4.12.

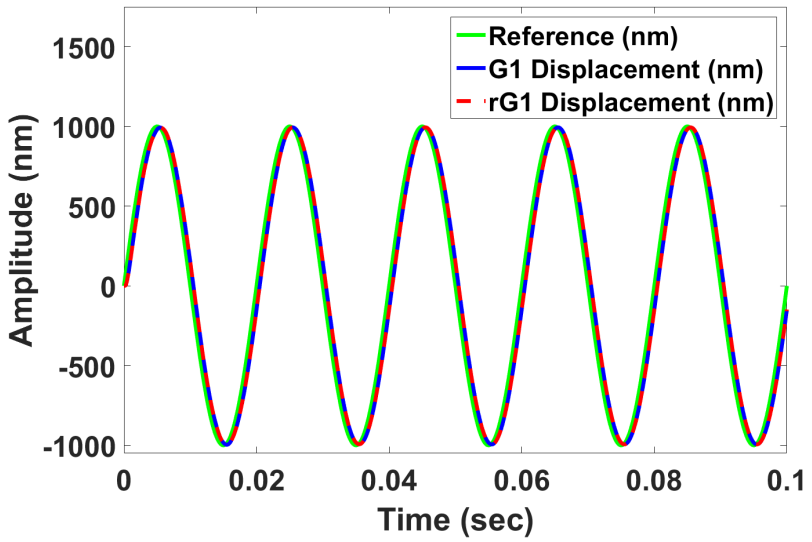

Figure 4.12: Open loop tracking (in simulation) of Sine wave with 1000 nm amplitude and 50 Hz frequency by the fitted plant model and reduced plant model.

4.2 Control Design for Drift Rejection

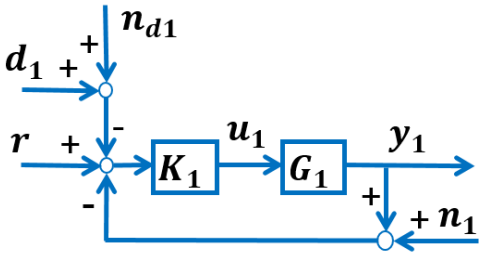

Figure 4.13: Transfer function block diagram of the negative feedback control architecture for the sensor drift rejection scheme. Here, G_1 is experimentally identified actuator model, K_1 is the designed controller, y_1 is the actuator displacement, d_1 is the actuator thermal drift, n_1 and n_{d1} are the measurement noise for the actuator position and sensor thermal drift.

The transfer function block diagram in Figure 3.11 shows sensor drift d_1 being introduced in the feedback loop. Our goal from the fine-scanning of actuator point is to achieve good tracking and minimize the tracking error, $e = r - y_1 - d_1$. Here,

$$y_1 = T_1(r - d_1 - n_1 - n_{d1}) \tag{4.1}$$

$$e = S_1(r - d_1) + T_1(n_1 + n_{d1}) \tag{4.2}$$

Where, $S_1 = 1/(1 + G_1 K_1)$ is the sensitivity transfer function and $T_1 = G_1 K_1/(1 + G_1 K_1)$ is the complementary sensitivity transfer function. To achieve good tracking, we would like to have $T_1 \approx 1$ within the bandwidth frequencies and also T_1 needs to be small in the high frequencies where measurement noise n_1 and n_{d1} are predominant. This would give $y_1 \approx r - d_1$, where $r - d_1$ can be thought of as the reference signal the actuator should track to eliminate the effect of thermal drift. To minimize the tracking error e, we need to make S_1 small in the bandwidth frequencies of reference signal r and in the low frequencies which is characteristic of thermal drift d_1, effectively making the term $S_1(r - d_1)$ small. Also, T_1 needs to be small in the high frequencies to minimize the second term $T_1(n_1 + n_{d1})$ in tracking error.

4.2.1 H_∞ Control Design for Drift Rejection

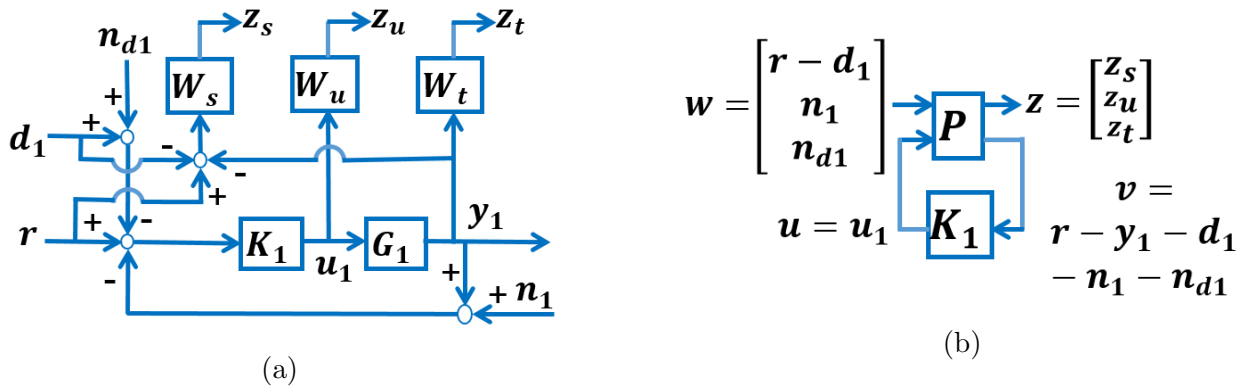

(a) (b)

Figure 4.14: (a) Transfer function block diagram of the H_∞ mixed-sensitivity minimization problem, which incorporates the measured sensor thermal drift d_1 in the optimal control architecture. Here, W_s, W_u, and W_t are the design weights and $z = [z_s\ z_u\ z_t]^T$ are the regulated outputs. (b) Generalized control format of the optimal control problem, where P is the generalized plant, $w = [r - d_1\ n_1\ n_{d_1}]^T$ are the exogenous inputs.

The transfer function block diagram for the H_∞ mixed-sensitivity minimization problem is shown in Figure 4.14a. The closed-loop objectives are achieved simultaneously by choosing appropriate design weight W_s, W_t, and W_u. The weighted tracking error $z_s = W_s(r -$

$y_1 - d_1$), weighted stage displacement $z_t = W_t\, y_1$, and weighted control effort $z_u = W_u\, u_1$ are the regulated output signals corresponding to the tracking bandwidth, noise attenuation and control effort closed-loop objectives. The closed-loop transfer function matrix T_{wz} from exogenous inputs $w = [r \; -d_1 \; n_1 \; n_{d1}]$ to regulated outputs $z = [z_s \; z_u \; z_t]$ is minimized to achieve the closed-loop objectives. The optimal control algorithm K_1 is obtained by solving the following minimization problem,

$$\min_{stab.\, K_1} \; \|T_{wz}\|_\infty \tag{4.3}$$

The design weights shape the closed loop transfer functions S_1, T_1, and $K_1\, S_1$. The sensitivity weight W_s is designed to have a low-pass filter shape, so that S_1 gets high pass filter shape, which effectively makes the tracking error small in the reference trajectory frequencies (Skogestad and Poslethwaite [39]). For example, a 70 Hz -3 dB bandwidth and 8 Hz -40 dB bandwidth H_∞ controller K_1 was designed, with the sensitivity weighting transfer function (Figure 4.15) given by,

$$W_s = \frac{s^4 + 1046\, s^3 + 4.103e5\, s^2 + 7.152e7\, s + 4.676e9}{2\, s^4 + 422.7\, s^3 + 3.35e4\, s^2 + 1.18e6\, s + 1.559e7} \tag{4.4}$$

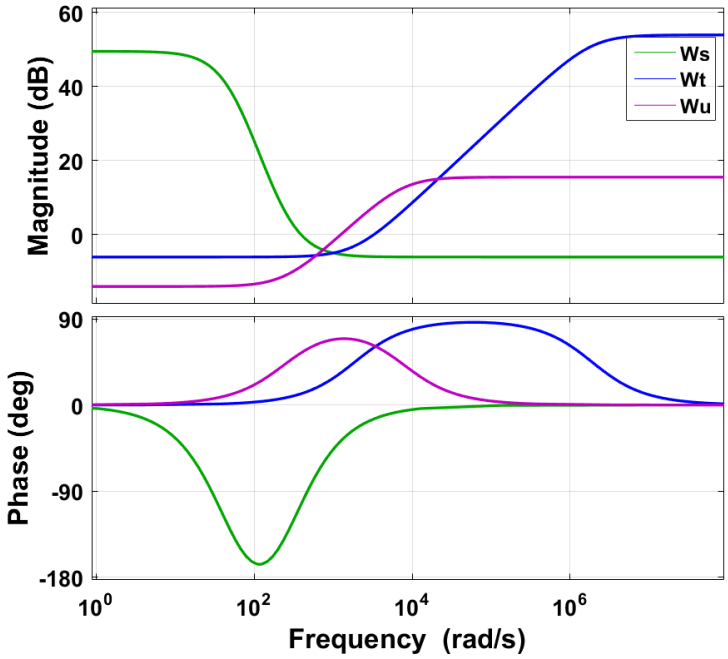

Figure 4.15: Bode diagram of the design weights W_s, W_t, and W_u for a particular H_∞ controller design.

The complementary sensitivity weight W_t is chosen to have a high pass filter shape, which

makes T_1 to have a low pass filter shape; $T_1 \approx 1$ in low frequencies for good tracking and small in high frequencies for measurement noise attenuation. Here, $1/|W_t(s)|$ acts as an upper bound for the absolute value of complementary sensitivity transfer function $|T|$. For the 70 Hz -3 dB bandwidth H_∞ controller that was mentioned above, with following first order proper complementary sensitivity weighting transfer function (Figure 4.15) was chosen.

$$W_t = \frac{s + 1885}{0.002\,s + 3770} \tag{4.5}$$

To bound the controller output the control effort weight W_u is chosen so that it keeps $K_1\,S_1$ small in bandwidth frequencies.

$$W_u = \frac{s + 251.3}{0.1667\,s + 1257} \tag{4.6}$$

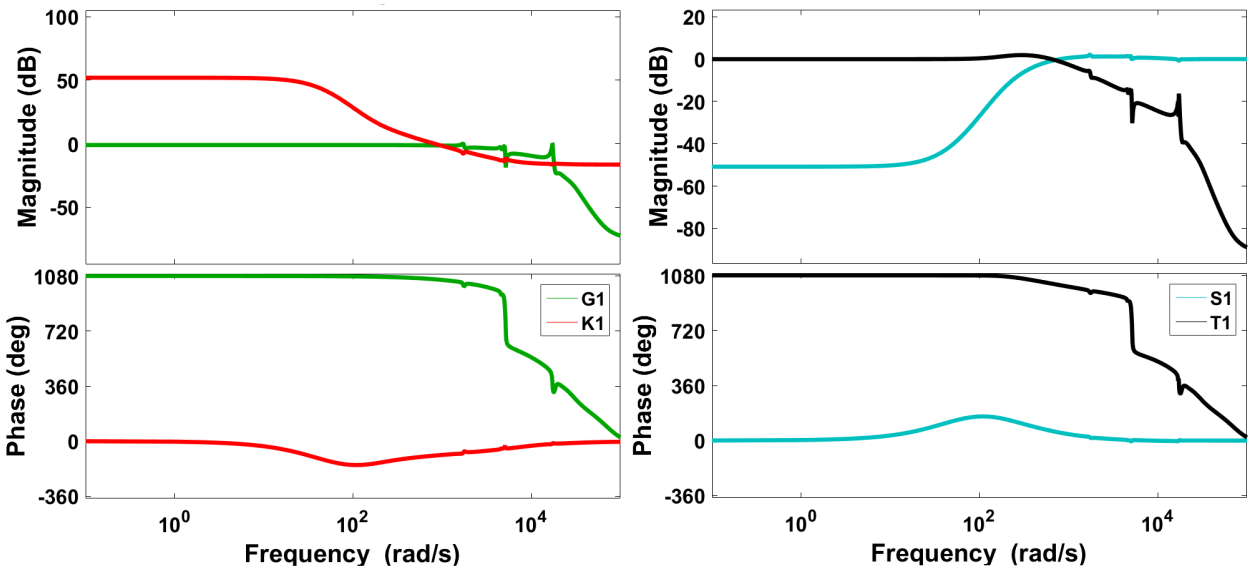

(a) (b)

Figure 4.16: (a) Bode diagram of the actuator model G_1 and the designed H_∞ controller K_1. (b) Bode diagram of the closed-loop transfer functions S_1 and T_1.

Figure 4.16a shows the Bode plot of the identified plant transfer function G_1 and the designed 16^{th} order H_∞ controller K_1 with 70 Hz -3 dB bandwidth and 8 Hz -40 dB bandwidth. The closed loop transfer functions S_1 and T_1 are shown in Figure 4.16b.

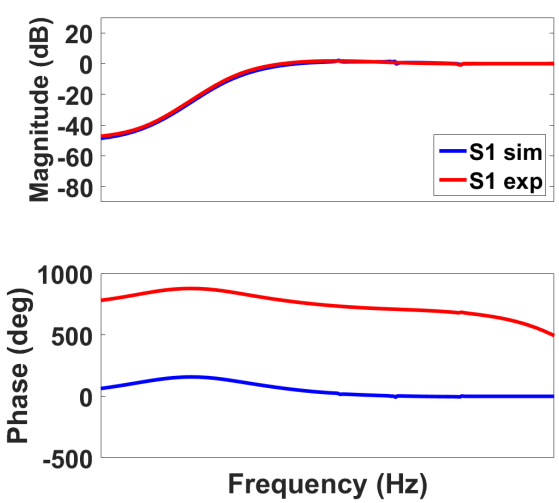

(a)

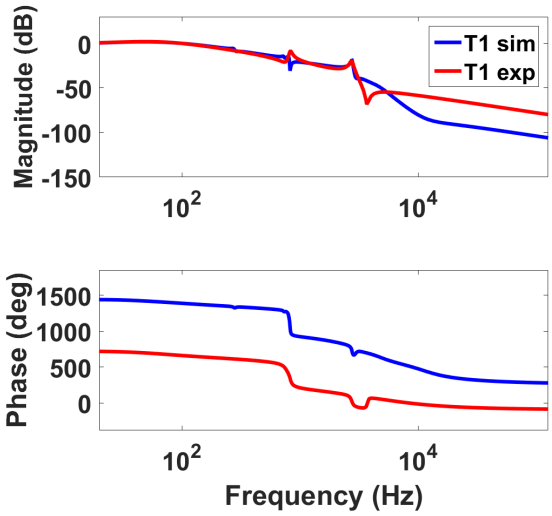

(b)

Figure 4.17: Comparing the design and experimental closed loop transfer function, (a) Bode plot of $S_{1,sim}$ and $S_{1,exp}$, and (b) Bode plot of $T_{1,sim}$ and $T_{1,exp}$

$$K_1 = \frac{num\, K_1}{den\, K_1}$$

$$\begin{aligned} num\, K_1 &= 2.4354e6(s+6012)(s+1563)(s+144.1)(s^2+262.6s+2.71e4) \\ &\quad (s^2+92.84s+3.039e6)(s^2+157.9s+2.1e7)(s^2+160.2s+2.567e7) \\ &\quad (s^2+9550s+2.731e8)(s^2+431.2s+2.993e8) \\ den\, K_1 &= (s+1.635e7)(s+1715)(s+59.72)(s+45.91)(s^2+105.7s+2838) \\ &\quad (s^2+115s+3.064e6)(s^2+164.5s+2.105e7)(s^2+151.3s+2.593e7) \\ &\quad (s^2+9339s+2.783e8)(s^2+498.6s+2.998e8) \end{aligned}$$

To verify that the controllers were implemented properly the closed-loop transfer functions S_1 and T_1 was identified from experimental data and compared to the corresponding design transfer functions. The bode plot of actuator closed loop sensitivity transfer function S_1 and complementary sensitivity transfer function T_1 for simulation and experiment are plotted in the Figure 4.17a and Figure 4.17b, respectively. The experimental S_1 and T_1 transfer functions matches closely with the the simulation results.

4.3 Results for Drift Rejection

In this section, we will show tracking and positioning resolution results for both open loop and closed loop cases. In particular the tracking results can be explained as four different cases: Case - I: open loop tracking with no knowledge of drift, Case - II: open loop tracking with knowledge of drift, Case - III: closed loop tracking with no knowledge of drift, and Case - IV: closed loop tracking with drift information given as part of the feedback. The positioning resolution results will be shown for three cases: Case - I: open loop positioning resolution with no knowledge of drift, Case - II: closed loop positioning resolution with no knowledge of drift, and Case - III: closed loop positioning resolution with drift information given as part of the feedback.

4.3.1 Tracking Results

4.3.1.1 Case - I: Open loop tracking with no knowledge of sensor drift

The tracking verification experiments are done where to replicate the thermal heating cycle of the environment at beamline experimental hutch the two heaters were turned ON for approximately 10 minutes and then turned OFF. Data was collected for around 30 minutes. The open loop tracking of sine wave with amplitude 1000 nm and frequency 8 Hz is shown in the Figure 4.18a and Figure 4.18b. The displacements shown in this two figures are absolute displacement with respect to the global reference frame. The actuator has no knowledge of the thermal drift. Although the sensor is itself drifting, this drift is considered by the sensor as a actuator motion. Clearly, the open loop stage absolute displacement is moving off by approximately the amount of the thermal drift of the sensor. At the maximum point of the drift the actuator has move away by about half a micron Figure 4.18b. This would surely result in a very bad X-ray images. The open loop tracking error $e_1 = r_1 - y_1$ is shown in the Figure 4.18c and Figure 4.18d. The tracking error follows the trend of the thermal drift shown in Figure 4.18e.

4.3.1.2 Case - II: Open loop tracking with knowledge of sensor drift

The open loop tracking of sine wave with amplitude 1000 nm and frequency 8 Hz is shown in the Figure 4.19a and Figure 4.19b. The displacements shown in this two figures are absolute displacement with respect to the global reference frame. The difference from the previous case is that, here the open loop has the knowledge of sensor drift d_1. Figure 4.19a

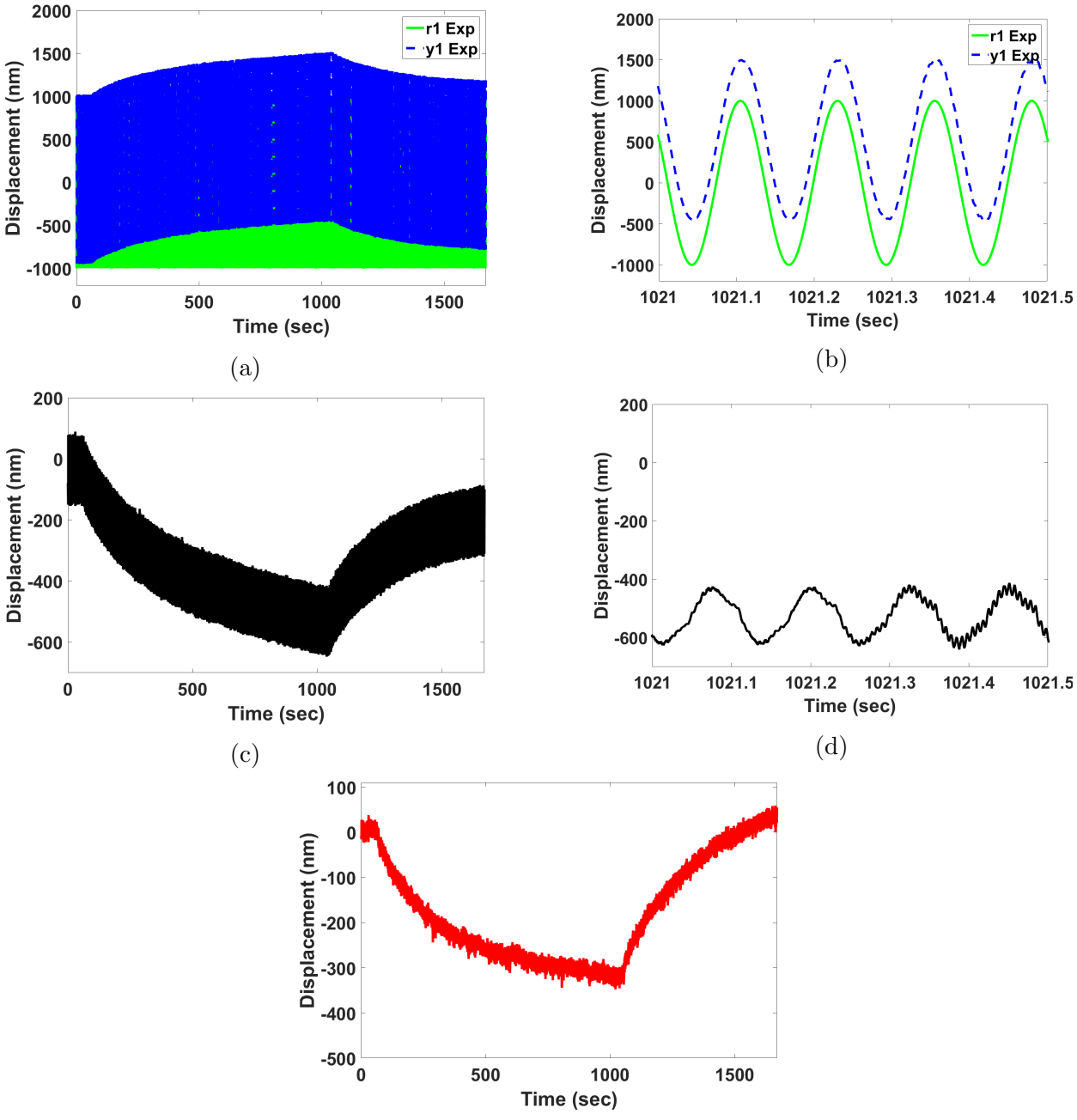

Figure 4.18: In this tracking experiment the open loop system has no knowledge (a) Open loop tracking for a sinusoidal reference trajectory with 1000 nm amplitude and 8 Hz frequency, (b) Magnified plot of the open loop tracking, (c) open loop tracking error $e_1 = r_1 - y_1$, (d) magnified plot of the open loop tracking error, and (e) drift d_1 observed during the open loop tracking experiment.

and Figure 4.19b are plots of reference r_1 and drift compensated actuator displacement $y_1 + d_1$. Compared to the previous open loop results a small drift is observed which is the typical open loop actuator drift, not the sensor thermal drift. The open loop tracking error $e_1 = r_1 - y_1 - d_1$ is shown in Figure 4.19c and Figure 4.19d is much smaller. We still observe error of couple hundred nm, but less than before. The corresponding thermal drift shown in Figure 4.19e.

4.3.1.3 Case - III: Closed loop tracking with no knowledge of sensor drift

This is the current state-of-the-art at the APS ANL. All results for Velociprobe X-ray microscope shown in chapter-3 corresponds to this case. The closed loop tracking of sine wave with amplitude 1000 nm and frequency 8 Hz is shown in the Figure 4.20a and Figure 4.20b. The displacements shown in this two figures are absolute displacement with respect to the sensor fixture and not the global reference frame. In this case the closed loop has no knowledge of the thermal drift, i.e. the drift is not given as feedback to the H_∞ controller. So, Figure 4.20a and Figure 4.20b are plots of reference r_1 and actuator displacement y_1. Clearly, the tracking is exceptionally good (as expected with the H_∞ controller) with minimum tracking error $e_1 = r_1 - y_1$ as shown in Figure 4.20c and Figure 4.20d. As explained before the tracking error is approximately 3.5% compared to the reference, which is larger than the 1% expected error, since noise floor of drift signal is high. Note the -40 dB bandwidth of the H_∞ controller is 8 Hz. The corresponding thermal drift d_1 is shown in Figure 4.20e.

The important difference to notice is that irrespective of the fact that the sensor itself is drifting by almost 400 nm the tracking still is very good. This is because the drift of the sensor itself is erroneously considered by the same sensor as stage motion. To compensate for this erroneous stage motion the controller moves the stages in wrong direction to maintain perfect tracking. Physically what this means is that, as the sensor thermally drifts the controller compensation moves the whole system with respect to the global reference frame. Now, in case of X-ray imaging such erroneous motion of the whole optics stage system with respect to sample stages will mean the X-ray images (end product for the X-ray microscope) will be affected. Without the knowledge of the drift, through measurement, it would always seem the stages are tracking the reference trajectory with respect to the global reference frame perfectly, when they are actually not.

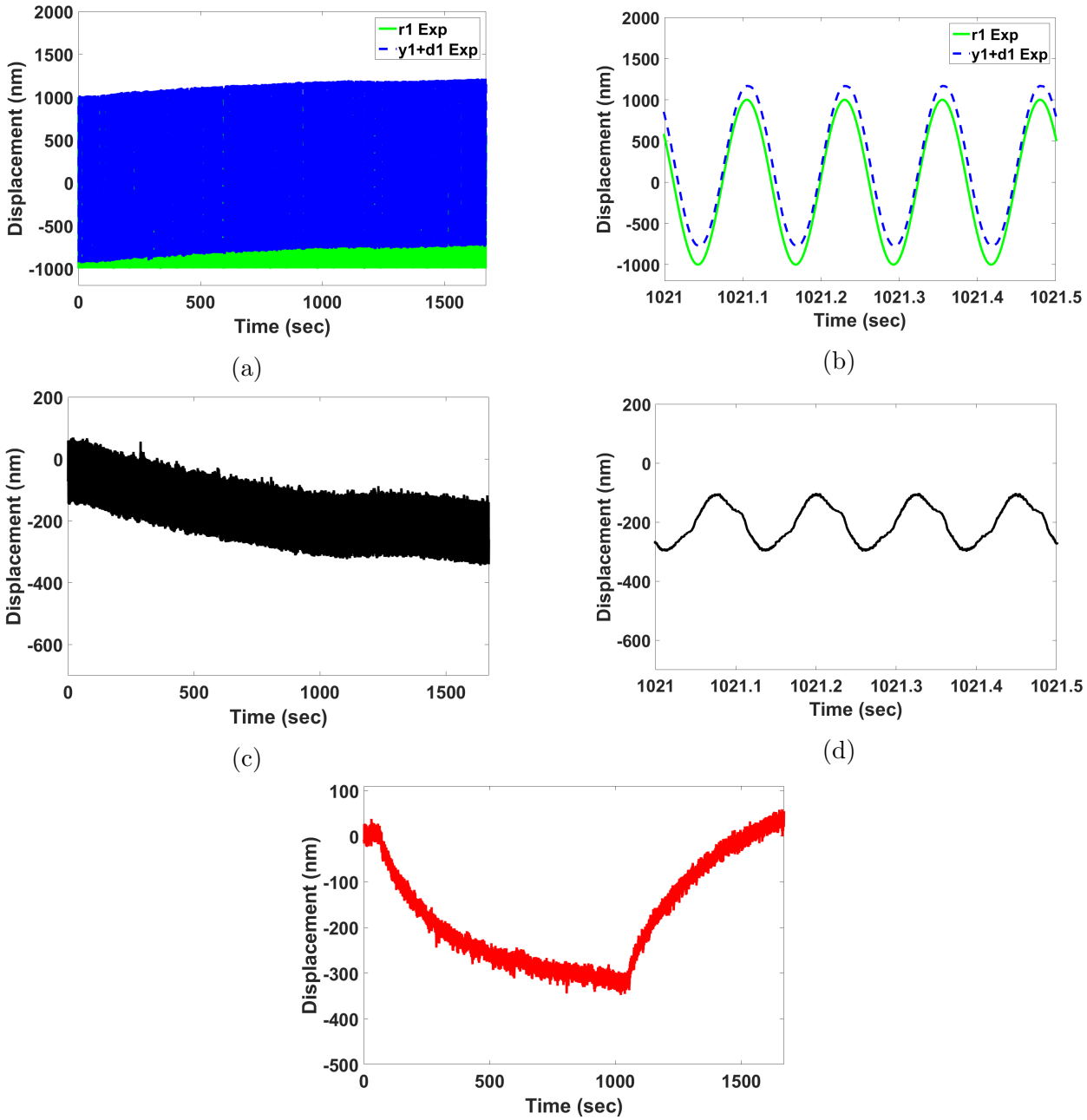

Figure 4.19: (a) Open loop tracking for a sinusoidal reference trajectory with 1000 nm amplitude and 8 Hz frequency, (b) Magnified plot of the open loop tracking, (c) open loop tracking error $e_1 = r_1 - y_1 - d_1$, (d) magnified plot of the open loop tracking error, and (e) drift d_1 observed during the open loop tracking experiment.

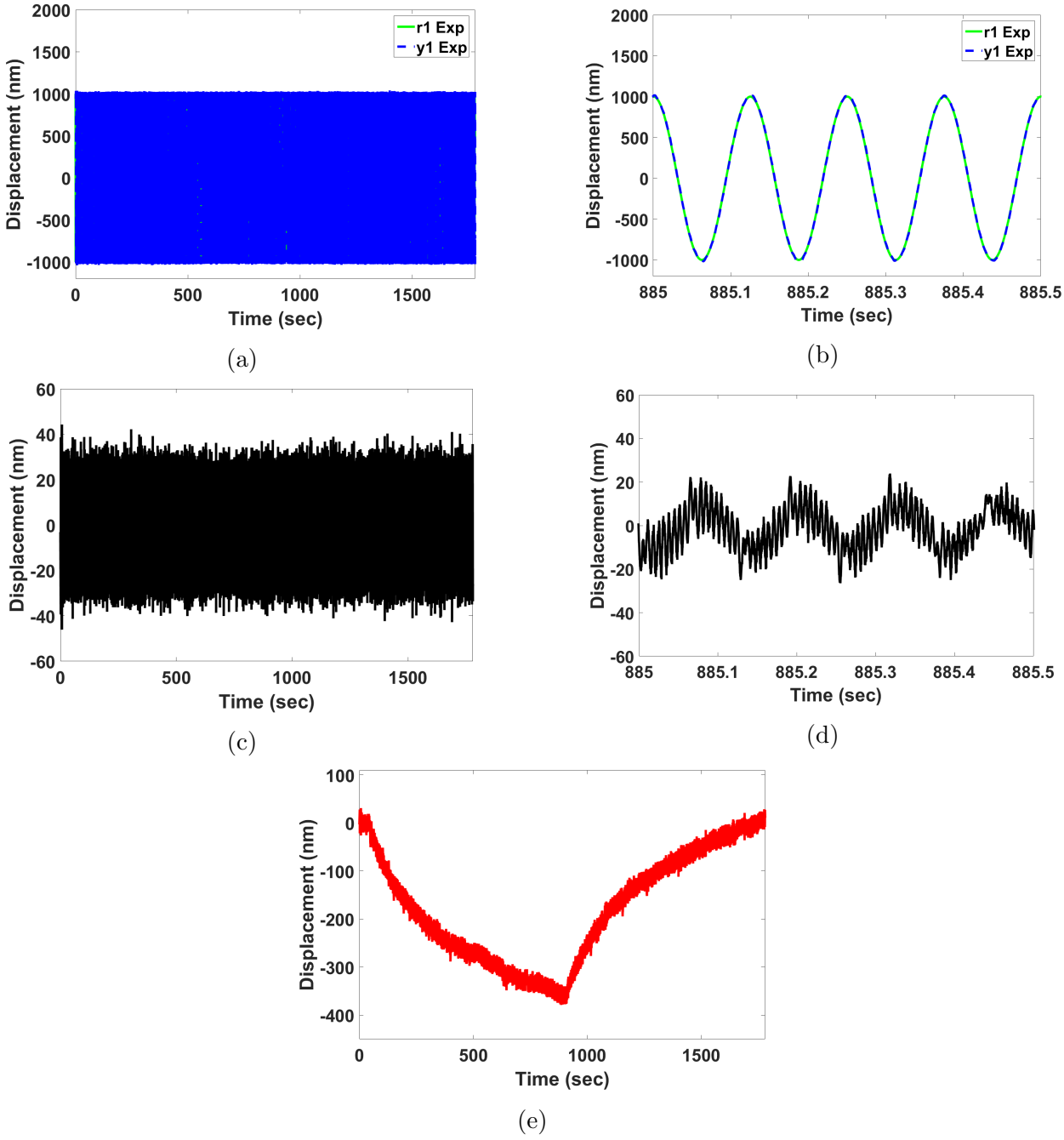

Figure 4.20: (a) Closed-loop tracking for a sinusoidal reference trajectory with 1000 nm amplitude and 8 Hz frequency with no knowledge of the thermal drift of the sensor, (b) Magnified plot of the same closed-loop tracking shows perfect tracking with very small tracking error, (c) closed loop tracking error, (d) magnified plot of the closed loop tracking error, and (e) Drift observed observed during the closed loop tracking experiment.

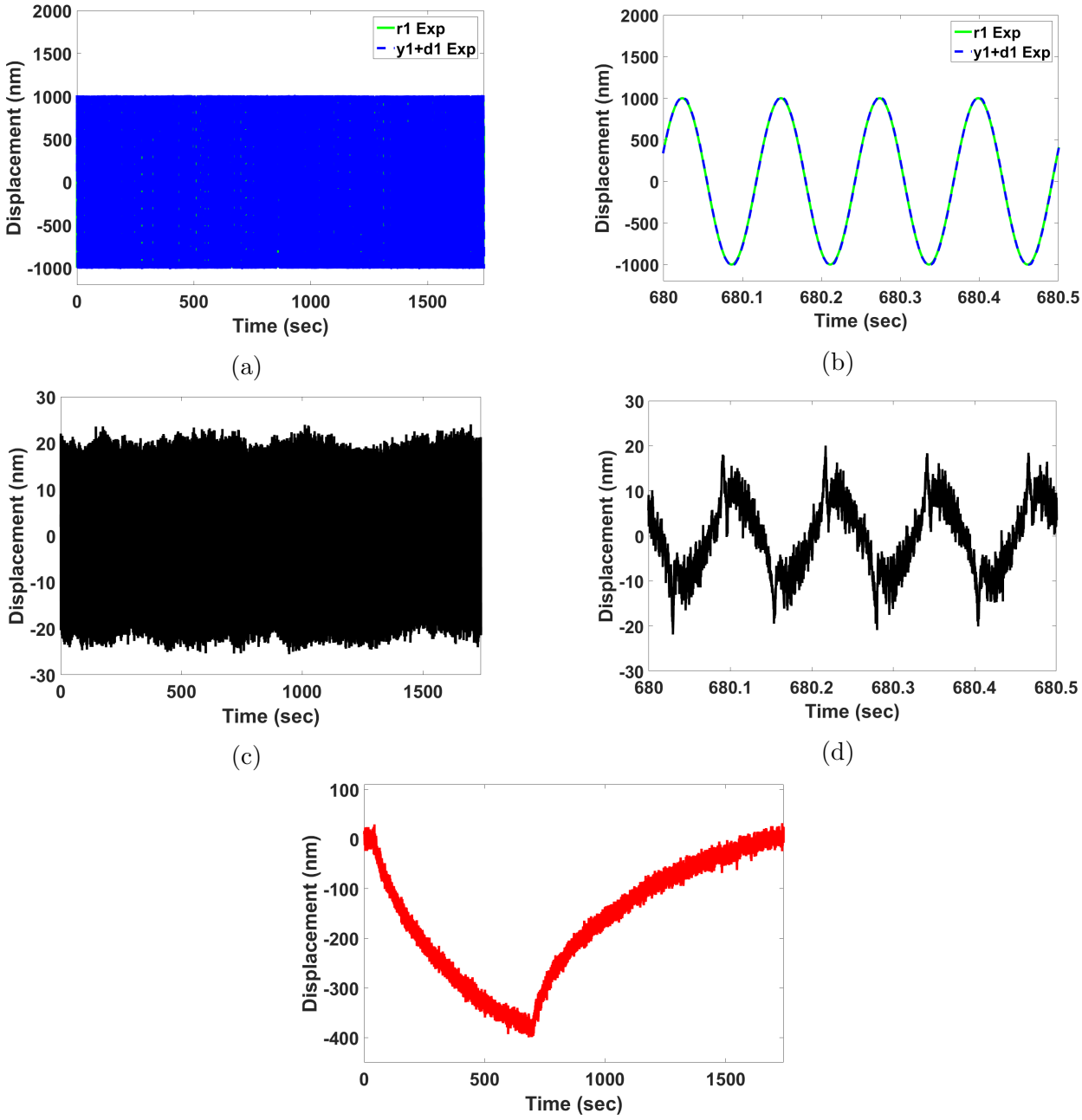

Figure 4.21: (a) Closed-loop tracking for a sinusoidal reference trajectory with 1000 nm amplitude and 8 Hz frequency with the measured thermal drift being part of the feedback signal $y_1 + d_1$, (b) Magnified plot of the closed-loop tracking, (c) closed loop tracking error, (d) magnified plot of the closed loop tracking error, and (e) Drift observed observed during the closed loop tracking experiment.

4.3.1.4 Case - IV: Closed loop tracking with measured sensor drift given as part of the feedback

The results in case - IV showcases the proof-of-concept for chapter 4. The closed loop tracking of sine wave with amplitude 1000 nm and frequency 8 Hz is shown in the Figure 4.21a and Figure 4.21b. The displacements shown in this two figures are absolute displacement with respect to the global reference frame. In this case the drift information is given as feedback to the H_∞ controller. Figure 4.21a and Figure 4.21b are plots of reference r_1 and drift compensated actuator displacement $y_1 + d_1$. Clearly, the tracking is exceptionally good with minimum tracking error $e_1 = r_1 - y_1 - d_1$ as shown in Figure 4.21c and Figure 4.21d. Given the reference amplitude of 1000 nm the tracking error is approximately 2%, which is expected since the -40 dB bandwidth of the H_∞ controller is 8 Hz. Although we expect 1% tracking error, the noise floor of the drift signal is contributing to the larger than 1% tracking error. The corresponding thermal drift d_1 is shown in Figure 4.21e. Now, we can confidently say that the actuator is tracking the reference (sine wave, can be any custom trajectory like raster scan, square snake scan, and so on) trajectory perfectly and in an absolute sense with respect to the global reference frame, even when the sensor (on which the feedback depends) itself is drifting due to temperature change in the surroundings.

4.3.2 Positioning Resolution Results

4.3.2.1 Case - I: Open loop positioning resolution with no knowledge of sensor drift

The positioning resolution of the actuator in open loop was calculated by giving a zero amplitude zero frequency input to the actuator and measuring the actuator response. Basically this means the actuator was driven by external disturbance and noise. Noise histogram of the actuator displacement is plotted in Figure 4.22. Clearly, the noise histogram is Gaussian but not centered to zero due to open loop drift of the actuator. No effect of the sensor drift is visible in this result, although the sensor is drifting by couple hundred nanometers. Due to large standard deviation of the data the $3\sigma-$ resolution of the actuator open loop displacement 35.6 nm.

4.3.2.2 Case - II: Closed loop positioning resolution with no knowledge of sensor drift

Figure 4.23 shows the noise histogram of the closed loop experiments for the cases where the feedback signal to the H_∞ controller is y_1. i.e. the closed loop has no knowledge that the sensor is drifting due to change of temperature in the environment or due to other

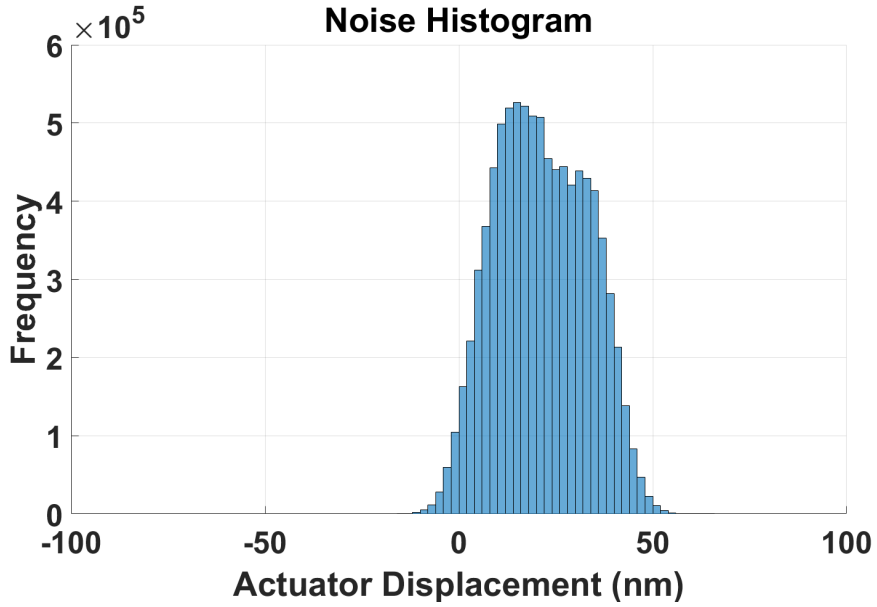

Figure 4.22: Noise histogram of experimental actuator displacement in open loop with the 3σ positioning resolution is 35.6 nm. The open loop displacement is y_1 and has no knowledge of drift signal.

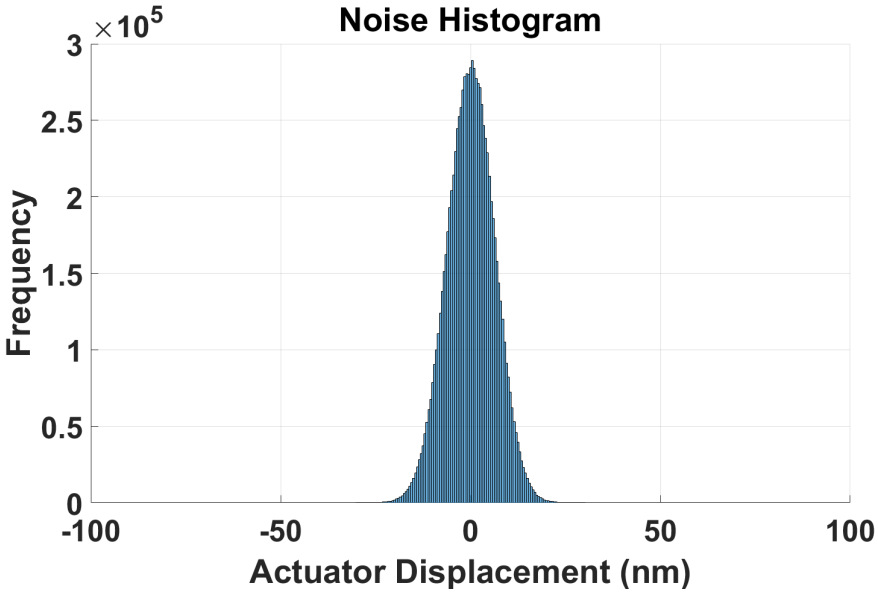

Figure 4.23: Noise histogram of experimental actuator displacement y_1 in closed loop with the H-infinity controller with bandwidth 70 Hz. The 3σ positioning resolution is 18.7 nm. The drift signal is not fed back to the controller in this case. The feedback to the H_∞ controller in this case is y_1

heat sources. The noise histogram is Gaussian, centered to zero and not skewed. The $3\,\sigma$ positioning resolution achieved when in this case is 18.7 nm. This is better than open loop. This case is the current state-of-the-art at APS, ANL. All results in shown in chapter 3 corresponds to this case. The closed loop positioning resolution is better than open loop with an improvement of 147%. But with respect to the global reference frame the stages have drifted away by couple 100 nm with the sensor. So, the effect on the X-ray image, if the actuator were one of the scanning stages, would be detrimental.

4.3.2.3 Case - III: Closed loop positioning resolution with measured sensor drift is as part of the feedback

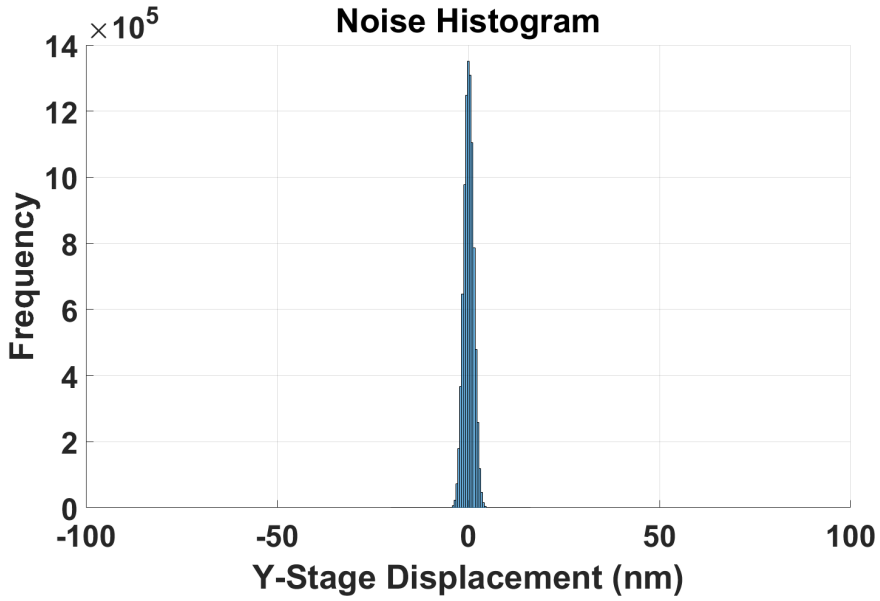

Figure 4.24: Noise histogram of experimental actuator displacement with measured sensor drift added to it (i.e. $y_1 + d_1$) in closed loop with the H-infinity controller with bandwidth 70 Hz. The 3σ positioning resolution is 3.8 nm. The feedback to the H_∞ controller in this case is $y_1 + d_1$

Figure 4.24 shows the noise histogram of the closed loop experiments for the cases where the feedback signal to the H_∞ controller is $y_1 + d_1$, i.e. measured drift of the sensor is given to the controller as part of the feedback. The noise histogram is Gaussian, centered to zero and not skewed. The $3\,\sigma$ positioning resolution achieved when the measured drift is fed back to the controller is 3.8 nm. We achieve better positioning resolution when the sensor drift is fed back to the controllers, in addition to better tracking with respect to the global reference frame. This case gives positioning resolution improvement of 179% over closed loop with no knowledge of sensor drift and 189% over open loop also with no knowledge of sensor drift.

4.4 Impact on X-ray Microscopy

Countering the sensor drift through measurement and fast and robust optimal control will have significant impact on the X-ray imaging. Some case are as follows:

- In an imaging experiment where a target area of $1\,mm \times 1\,mm$ of a 10 nm technology Intel chip is being scanned in 2D with 100 nm diameter X-ray probe and 50 nm step size along both axes in the scanning plane, the total time required to do the scan would be 38.88 hours. This ptychogrphic flyscan would be done at 3 kHz detector trigger rate with $4.2e8$ number of exposures along a square snake scan pattern. The sensors in the XY optics scanning stages and sample stages can drift by couple hundred nanometers by this time frame. The erroneous position information would corrupt the diffraction patterns recorded at the area detector. This will make the solution of the "phase retrieval algorithm" harder and adversely affect the image spatial resolution.

- If we are interested in doing a X-ray tomography of the same 10 nm technology Intel chip with 180 projections to cover 180 degrees, the time required for the whole experiment will be much more. The 3D reconstructed image of the processor would be adversely affected by the sensor drift during scanning.

- Image reconstruction errors like image feature ambiguity, stitching error would decrease significantly.

- Sensor drift might be one the factor that is limiting the best image spatial resolution achievable in X-ray microscopy.

CHAPTER 5

DISCUSSION AND FUTURE DIRECTIONS

Discussion

This thesis presents the design and implementation of PID and $1DOF\ H_\infty$ controllers for Velociprobe X-ray microscope at APS. For the STXM technique, X-rays are focused as a spot and it is required to cover an area on the sample at a certain rate and high precision along a predefined trajectory. The obstacles to high precision scanning are open loop drift, unmodeled stage dynamics, nonlinear behavior of the nanopositioning stages, environmental disturbance (mechanical vibration and other irregular disturbances) and measurement noise (sensor noise and other electrical noise). The more conventional PID controllers helped achieve moderate -3 dB bandwidths of 149 Hz, 134 Hz and 151 Hz for the X, Y, and Z stages, respectively. The prime target of this thesis although was to introduce the H_∞-controller algorithm that is capable of accommodating the performance specifications such as tracking bandwidth, positioning resolution, disturbance rejection, measurement noise and robustness to unmodeled stage dynamics in a customizable manner. Another significant step-up in controller implementation was using the Biquad structure to represent the discrete controllers in the FPGA of NI cRIO control hardware. The H_∞ control laws resulting from $S\backslash T\backslash KS$ mixed-sensitivity minimization when implemented showcases a $-3\,dB$ bandwidth improvement of 134% (200 Hz), 150% (200 Hz), and 132% (200 Hz) in case of X, Y, and Z stages, respectively, over baseline PID controllers. The presence of RHP zeros in the identified models of optics X, Y, and Z stages limited the achievable bandwidth through H_∞ control design. The step scans (for raster scan pattern) and flyscans (for custom square snake scan pattern) require high -3 dB bandwidth controllers for the proper scanning. The high bandwidth controllers (PID and H_∞) presented in this work both had approximately similar positioning resolutions for all the scanning stages. The fundamental limitations and design trade-offs were addressed in this thesis. The step scan imaging technique utilizing the optimal control algorithm and NI control hardware resulted in a 8 fold improvement in X-ray imaging bandwidth. The flyscan imaging technique resulted in over 10^4 times improvement compared to the step scan technique with our control design and over 10^6 times improvement

compared to the previous step scan performance at the APS beamline. The highest spatial resolution of the X-ray images with the above imaging techniques were in the order of 14 nm. The improvement in the imaging bandwidth is not limited by our control algorithm or imaging technique, but rather by the limited number of photons available in APS X-rays (APS-U: 100 times improvement in X-ray flux) and the detector trigger rate (3 kHz).

In the second part of the thesis, we identified a key limitation of the conventional X-ray imaging technique, the sensor drift, and incorporated it into our optimal control architecture to practically remove it. The high resolution sensors, that were used to do high bandwidth high precision scanning, themselves drift with respect to the global reference frame. To counter this, sensor drift was measured in real time and incorporated this into the H_∞ control architecture. The experimental tracking results presented here clearly shows that even with the sensor drifting by couple $100\,nm$ the closed loop tracking, in absolute sense with respect to the global reference frame, was not affected by the drift. This, when implemented to the Velociprobe X-ray microscope at APS beamline, will result in a significant improvement in X-ray imaging spatial resolution and overall image quality.

Future Directions

- Scan trajectories containing less frequency components (spiral, circular, Lissajous, and so on) would produce better X-ray images due to better tracking with the existing high bandwidth controllers. Low bandwidth and high resolution controllers would be better suited to tracking these low frequency trajectories, while improving X-ray image quality.

- We observed that due to presence of RHP zeros in the identified stage models the achievable tracking bandwidth is limited. It would be beneficial to invest resources on the optics scanning stage codesign with the controller architecture in mind. Optics scanning stages with higher stiffness and RHP zeros pushed towards higher frequency region and beyond the resonant frequency would significantly increase the achievable tracking bandwidth in closed-loop.

- In the drift rejection experiment we used an additional Laser interferometer sensor head to measure drift. A better option that we studied but did not implement in experiment would be the use of strain gauge sensors. This sensors are compact (couple of mm across thin strip) and can be glued to the sensor fixtures to the measure thermal drift.

APPENDIX A

APPENDIX FOR CHAPTER 2

1. Coherent X-Ray Diffraction Imaging (CXDI or CDI)

   In coherent x-ray diffraction imaging (CXDI) the sample is illuminated by highly coherent beam of x-ray. The beam scattered by the object produces a diffraction pattern downstream. This diffraction pattern is measured by an area detector. The recorded diffraction pattern is used to reconstruct an image of the object. The data collected by the area detector is the absolute count of photons that are hitting the detector surface at any given time (in case of CXDI). This is basically the intensity information , $|\psi(u)|^2$. Where, $|\psi(u)|$ is the amplitude of the diffracted photons at the detector plane. Notice that the phase information is not recorded by the detector.

2. Phase Problem

   In case of CXDI, the detector placed downstream of the sample only registers the intensity of the impinging photons. So the phase information of the object is apparently lost. Now, the object can treated as a complex function having both amplitude and phase components. So clearly if we intend to reverse engineer details of the object from the diffraction image detected, the phase needs to be somehow retrieved. This is known as the "phase problem".

3. Ptychographic Iterative Engine (PIE)

   It is a combination of ptychography and phase retrieval algorithm.

APPENDIX B

APPENDIX FOR CHAPTER 3

1. Welch's Method:

The non-parametric system identification method that was applied here utilizes the Welch's method. Welch's method provides an estimator of the power spectral density (PSD) detailed in the paper by Welch [35]. This method divides a given time series data into segments (possibly overlapping), calculates the estimated PSD for each segmented data, and then averages this PSD estimates. The *pwelch* function in MATLAB conveniently gives PSD estimates using this method. The PSD estimate on each segment is nothing but calculating the discrete-time Fourier transform (DTFT) of the samples in the data and then scaling the magnitude squared of the DTFT.

Suppose, the optics scanning X-stage G_x is a linear, time invariant system and $i(n)$ and $j(n)$ are the input and output time-domain data of the X-stage, respectively. The power spectrum of $i(n)$ and cross spectral density (CPSD) of $i(n)$ and $j(n)$ are related as follows:

$$P_{ji}(\omega) \;=\; G_x(\omega)\, P_{ii}(\omega), \tag{B.1}$$

Where, P_{ii} = power spectral density of the input signal i,
P_{ji} = cross power spectral density of the input signal i and output signal j

$$G_x(\omega) \;=\; \frac{P_{ji}(\omega)}{P_{ii}(\omega)} \tag{B.2}$$

Here, G_x is the non-parametric transfer function estimate of the actual X-stage dynamics by Welch's method. MATLAB function *tfestimate* calculates this transfer function

estimate, utilizing the Welch's method of estimating PSD from a given input and output time domain data. Moreover, *tfestimate* estimates both magnitude and phase information of the actual system.

2. Transfer function of the 13^{th} order model G_{yy} for the Velociprobe optics scanning YY-stage,

$$
\begin{aligned}
G_{yy} &= \frac{num\ G_{yy}}{den\ G_{yy}} \\
num\ G_{yy} &= -7.5078e13(s-2.337e5)(s-2.538e4)(s+2.153e4)(s^2+1713s+7.592e7) \\
&\quad (s^2+1321s+1.314e8)(s^2-2.385e4s+5.944e8)(s^2-2436s+7.146e8) \\
den\ G_{yy} &= (s+1.562e13)(s^2+7024s+1.311e7)(s^2+105s+6.151e7) \\
&\quad (s^2+4615s+7.008e7)(s^2+157.7s+1.087e8)(s^2+391s+6.581e8) \\
&\quad (s^2+350.8s+9.855e8)
\end{aligned}
$$

3. Transfer function of the 33^{rd} order model G_{zz} for the Velociprobe optics scanning ZZ-stage,

$$
\begin{aligned}
G_{zz} &= \frac{num\ G_{zz}}{den\ G_{zz}} \\
num\ G_{zz} &= 4.2907e7(s+1.425e4)(s-1.854e4)(s+0.003757)(s^2+67.11s+6.346e7) \\
&\quad (s^2+506.9s+8.582e7)(s^2+119.7s+1.375e8)(s^2+184s+1.968e8) \\
&\quad (s^2+6.053e4s+1.17e9)(s^2+271.7s+3.318e8)(s^2+464.2s+5.125e8) \\
&\quad (s^2-1.068e4s+6.469e8)(s^2-1668s+6.442e8)(s^2+1267s+6.703e8) \\
&\quad (s^2-48.81s+9.464e8)(s^2-44.92s+9.647e8)(s^2-11.85s+9.815e8) \\
&\quad (s^2-1.022e5s+4.573e9) \\
den\ G_{zz} &= (s+1.287e4)(s+3359)(s+5.032e-5)(s^2+5.096e4s+7.035e8) \\
&\quad (s^2+121.8s+6.14e7)(s^2+6082s+7.142e7)(s^2+58.21s+8.485e7) \\
&\quad (s^2+203.7s+1.439e8)(s^2+128s+2.006e8)(s^2+290s+3.188e8) \\
&\quad (s^2+4162s+5.18e8)(s^2+707.3s+5.836e8)(s^2+270.8s+6.565e8) \\
&\quad (s^2+370.2s+6.811e8)(s^2+16.3s+9.465e8)(s^2+293.5s+9.717e8) \\
&\quad (s^2+67.44s+9.809e8)(s^2+4.624e4s+1.544e10)
\end{aligned}
$$

4. Transfer function of the 12^{th} order model rG_{yy} for the Velociprobe optics scanning YY-stage,

$$
\begin{aligned}
rG_{yy} &= \frac{num\ rG_{yy}}{den\ rG_{yy}} \\
num\ rG_{yy} &= 1.124e6(s-2.538e4)(s+2.153e4)(s^2+1713s+7.592e7) \\
&\quad (s^2+1321s+1.314e8)(s^2-2.385e04s+5.944e8) \\
&\quad (s^2-2436s+7.146e8) \\
den\ rG_{yy} &= (s^2+7024s+1.311e7)(s^2+105s+6.151e7)(s^2+4615s+7.008e7) \\
&\quad (s^2+157.7s+1.087e8)(s^2+391s+6.581e8)(s^2+350.8s+9.855e8)
\end{aligned}
$$

5. Transfer function of the 28^{th} order model rG_{zz} for the Velociprobe optics scanning ZZ-stage,

$$
\begin{aligned}
rG_{zz} &= \frac{num\ rG_{zz}}{den\ rG_{zz}} \\
num\ rG_{zz} &= 6.0047(s+1.965e6)(s+3.426e4)(s-1.854e4)(s^2+67.08s+6.346e7) \\
&\quad (s^2+506.8s+8.582e7)(s^2+119.9s+1.375e8)(s^2+184.2s+1.968e8) \\
&\quad (s^2+270.5s+3.318e8)(s^2+467.5s+5.124e8)(s^2-1.068e4s+6.469e8) \\
&\quad (s^2-1668s+6.442e8)(s^2+1267s+6.705e8)(s^2-48.79s+9.464e8) \\
&\quad (s^2-44.88s+9.647e8)(s^2-11.78s+9.815e8) \\
den\ rG_{zz} &= (s+1.729e4)(s+3358)(s^2+121.8s+6.14e7)(s^2+6083s+7.149e7) \\
&\quad (s^2+58.21s+8.485e7)(s^2+203.7s+1.439e8)(s^2+128s+2.006e8) \\
&\quad (s^2+290.3s+3.188e8)(s^2+4191s+5.172e8)(s^2+705.7s+5.836e8) \\
&\quad (s^2+271s+6.566e8)(s^2+369.7s+6.811e8)(s^2+16.34s+9.465e8) \\
&\quad (s^2+299.5s+9.717e8)(s^2+67.11s+9.809e8)
\end{aligned}
$$

6. Transfer function of the 16^{th} order H_∞ controller K_{xx} for the Velociprobe optics scanning X-stage,

$$K_{xx} = \frac{num\ K_{xx}}{den\ K_{xx}}$$

$$\begin{aligned} num\ K_{xx} = &-17802(s+1.182e4)(s^2+6718s+1.494e7)(s^2+6137s+6.755e7) \\ &(s^2+183.7s+7.373e7)(s^2+1116s+6.033e8)(s^2+71.85s+6.796e8) \\ &(s^2+1252s+7.745e8)(s^2+2.24s+9.706e8) \\ den\ K_{xx} = &(s+8.153e4)(s+3.14)(s^2+1.026e4s+2.961e7)(s^2+614.4s+7.652e7) \\ &(s^2+6031s+8.688e7)(s^2+1276s+6.063e8)(s^2+448.2s+6.793e8) \\ &(s^2+1327s+7.733e8)(s^2+2.607s+9.706e8) \end{aligned}$$

7. Transfer function of the 13^{th} order H_∞ controller K_{yy} for the Velociprobe optics scanning Y-stage,

$$K_{yy} = \frac{num\ K_{yy}}{den\ K_{yy}}$$

$$\begin{aligned} num\ K_{yy} = &-99437(s+5510)(s+3194)(s^2+118.9s+6.147e7)(s^2+3025s+7.972e7) \\ &(s^2+151.9s+1.087e8)(s^2+404.9s+6.585e8)(s^2+402.8s+9.855e8) \\ den\ K_{yy} = &(s+2.998e04)(s+1.57e4)(s+0.9332)(s^2+1444s+7.422e7) \\ &(s^2+4025s+8.967e7)(s^2+1233s+1.166e8)(s^2+2619s+6.958e8) \\ &(s^2+1.437e4s+9.063e8) \end{aligned}$$

8. Transfer function of the 29^{th} order H_∞ controller K_{zz} for the Velociprobe optics scanning Z-stage,

$$K_{zz} = \frac{num\ K_{zz}}{den\ K_{zz}}$$

$$\begin{aligned} num\ K_{zz} = &-76544(s+3983)(s+2452)(s^2+121.5s+6.138e7) \\ &(s^2+6094s+7.443e7)(s^2+56.92s+8.487e7)(s^2+202.6s+1.439e8) \\ &(s^2+126.1s+2.006e8)(s^2+294s+3.188e8)(s^2+4077s+5.269e8) \\ &(s^2+692.9s+5.843e8)(s^2+290.9s+6.572e8)(s^2+360.6s+6.822e8) \\ &(s^2+16.29s+9.465e8)(s^2+290.1s+9.719e8)(s^2+68.15s+9.81e8) \end{aligned}$$

$$
\begin{aligned}
den\ K_{zz} = {} & (s + 1.174e5)(s + 2669)(s + 1.563)(s^2 + 85.48s + 6.339e7) \\
& (s^2 + 488.3s + 8.585e7)(s^2 + 1.795e4s + 1.934e8)(s^2 + 216.9s + 1.378e8) \\
& (s^2 + 206.4s + 1.971e8)(s^2 + 434.9s + 3.289e8)(s^2 + 1205s + 5.207e8) \\
& (s^2 + 7598s + 6.404e8)(s^2 + 1727s + 6.401e8)(s^2 + 1116s + 6.782e8) \\
& (s^2 + 51.23s + 9.465e8)(s^2 + 283.1s + 9.685e8)(s^2 + 56.33s + 9.813e8)
\end{aligned}
$$

APPENDIX C

APPENDIX FOR CHAPTER 4

1. Transfer function model of 23^{rd} order model G_1 for the actuator,

$$
\begin{aligned}
G_1 &= \frac{num\, G_1}{den\, G_1} \\
num\, G_1 &= 2.0563e9(s+1561)(s^2+106.3s+3.113e6)(s^2+183.5s+2.128e7) \\
&\quad (s^2-64.87s+2.677e7)(s^2+310s+2.915e8)(s^2+1429s+3.428e8) \\
&\quad (s^2-7.949e4s+2.023e9)(s^2+1.311e4s+5.261e8) \\
&\quad (s^2-5.698e4s+5.264e9)(s^2-126.9s+6.09e9)(s^2-7594s+6.875e9) \\
den\, G_1 &= (s+8.587e7)(s+4158)(s+1413)(s^2+92.02s+3.038e6) \\
&\quad (s^2+174.3s+2.103e7)(s^2+160.8s+2.565e7)(s^2+1.874e4s+1.837e8) \\
&\quad (s^2+387.2s+2.917e8)(s^2+432.1s+2.978e8)(s^2+8686s+3.767e8) \\
&\quad (s^2+1.534e4s+8.205e8)(s^2+6.914s+6.062e9)(s^2+46.74s+6.138e9)
\end{aligned}
$$

2. Transfer function model of 18^{th} order reduced model rG_1 for the actuator,

$$
\begin{aligned}
rG_1 &= \frac{num\, rG_1}{den\, rG_1} \\
num\, rG_1 &= 27(s+1561)(s^2+106.3s+3.113e6)(s^2+183.5s+2.128e7) \\
&\quad (s^2-64.87s+2.677e7)(s^2+310s+2.915e8)(s^2+1429s+3.428e8) \\
&\quad (s^2-7.949e4s+2.023e9)(s^2+1.31e4s+5.261e8)(s^2-5.698e4s+5.264e9) \\
den\, rG_1 &= (s+4158)(s+1413)(s^2+92.02s+3.038e6)(s^2+174.3s+2.103e7) \\
&\quad (s^2+160.8s+2.565e7)(s^2+1.874e4s+1.837e8) \\
&\quad (s^2+387.2s+2.917e8)(s^2+432.1s+2.978e8) \\
&\quad (s^2+8686s+3.767e8)(s^2+1.534e4s+8.205e8)
\end{aligned}
$$

REFERENCES

[1] Sheikh T. Mashrafi, Curt Preissner, Srinivasa M. Salapaka, *Countering Sensor Drift in X-ray Microscopy with Fast and Robust Optimal Control*. ACC, 2018.

[2] Junjing Deng, Curt Preissner, Christian Roehrig, Michael Wojcik, Shane Sullivan, David Vine, Barry Lai, Stefan Vogt, *The Velociprobe: A Fast Hard X-ray Nanoprobe for Ptychographic Imaging*. X-Ray Nanoimaging: Instruments and Methods, Volume 10389 2017.

[3] Curt Preissner, Junjing Deng, Chris Jacobsen, Barry Lai, Fabricio Marin, Jorg Maser, Sheikh Mashrafi, Christian Roehrig, Shane Sullivan, Stefan Vogt, *Earth, Wind, and Fire: The New Fast Scanning Velociprobe*. 9^{th} Mechanical Engineering Design of Synchrotron Radiation Equipment and Instrumentation, 2017.

[4] Sheikh T. Mashrafi, Curt Preissner, Srinivasa M. Salapaka, *The Velociprobe: Pushing the Limits with Fast and Robust Control*. ASPE 32nd Annual Meeting, 2017.

[5] Sheikh T. Mashrafi, Curt Preissner, Srinivasa M. Salapaka, *Fast Scanning of X-ray Optics: An Optimal Control Approach*. ASPE 31st Annual Meeting, 2016.

[6] Chibum Lee, Srinivasa M. Salapaka, *Model Based Control of Dynamic Atomic Force Microscope*. Review of Scientific Instruments, Volume 86, Issue 4, 2015.

[7] Junjing Deng, Youssef S. G. Nashed, Si Chen, Nicholas W. Phillips, Tom Peterka, Rob Ross, Stefan Vogt, Chris Jacobsen, David J. Vine, *Continuous Motion Scan Ptychography: Characterization for Increased Speed in Coherent X-ray Imaging*. Optics Express, Volume 23, No. 5, 2015.

[8] J. Maser, B. Lai, T. Buonassisi, Z. Cai, S. Chen, L. Finney, S. C. Gleber, C. Jacobsen, C. Preissner, C. Roehrig, V. Rose, D. Shu, D. Vine, S. Vogt, *A next-generation hard X-ray Nanoprobe beamline for in situ studies of energy materials and devices*. Metallurgical and Materials Transaction A, volume 45, issue 1, pp 85-97, 2014.

[9] Nazaretski E., Huang X., Yan H., Lauer K., Conley R., Bouet N., Zhou J., Xu W., Eom D., Legnini D., Harder R., Lin C.-H., Chen Y.-S., Hwu Y. and Chu Y. S., *Design and Performance of Scanning Ptychography microscope*. Review of Scientific Instruments, Volume 85, Issue 3, 2014.

[10] Gofron K. J., Lauer K., Nazaretski E., Yan H., Kalbfleisch S., Greer A., Dalesio B. and Chu Y. S., *Piezo Control for 1 nm Spatial Resolution Synchrotron X-ray Microscopy.* 17th Pan-American Synchrotron Radiation Instrumentation Conference (SRI2013), IOP Publishing, Volume 493, 2014.

[11] M. Borland, *Ultra-low-emittance light sources.* Synchrotron Radiation News, 27(6), 2-2, 2014.

[12] Sheikh T. Mashrafi, Curt Preissner, Srinivasa M. Salapaka, Huyue Zhao, *Something for (Almost) Nothing: X-ray Microscope Performance Enhancement Through Control Architecture Change.* ASPE 28th Annual Meeting, 2013.

[13] J. Maser, B. Lai, T. Buonassisi, Z. Cai, S. Chen, L. Finney, C. Gleber, C. Jacobsen, C. Preissner, C. Roehrig, V. Rose, D. Shu, D. Vine, and S. Vogt, *A Next-Generation Hard X-Ray Nanoprobe Beamline for In Situ Studies of Energy Materials and Devices.* Synchrotron Radiation Instrumentation, Volume 879, pp. 1321-1324, 2013.

[14] Maser J., Lai B., Buonassisi T., Cai Z. H., Chen S., Finney L., Gleber S-C., Harder R., Jacobsen C., Liu W., Murray C., Preissner C., Roehrig C., Rose V., Shu D., Vine D., Vogt S, *A Next-Generation In-Situ Nanoprobe Beamline for the Advanced Photon Source.* Proceedings of SPIE, Volume 8851, 2013.

[15] Nazaretski E., Kim J., Yan H., Lauer K., Eom D., Shu D., Maser J., Pešić Z., Wagner U., Rau C. and Chu Y. S., *Performance and Characterization of the Prototype nm-Scale Spatial Resolution Scanning Multilayer Laue Lenses Microscope.* Review of Scientific Instruments, Volume 84, Issue 3, 2013.

[16] Mike Beckers, Tobias Senkbeil, Thomas Gorniak, Klaus Giewekemeyer, Tim Salditt, Axel Rosenhahn, *Drift Correction in Ptychographic Diffractive Imaging.* Ultramicroscopy, 126, 44–47, 2013.

[17] Robert P. Winarski, Martin P. Holt, Volker Rose, Peter Fuesz, Dean Carbaugh, Christa Benson, Deming Shu, David Kline, G. Brian Stephenson, Ian McNulty, and Jorg Maser, *A Hard X-ray Nanoprobe Beamline for Nanoscale Microscopy.* Journal of Synchrotron Radiation, Volume 19, pp. 1056-1060, 2012.

[18] Nelson J., Misra S., Yang Y., Jackson A., Liu Y. J., Wang H. L., Dai H. J., Andrews J. C., Cui Y. and Toney M. F., *In Operando X-ray Diffraction and Transmission X-ray Microscopy of Lithium Sulfur Batteries.* Journal of American Chemical Society, 134 (14), 6337-6343, 2012.

[19] A. M. Maiden, M. J. Humphry, M. C. Sarahan, B. Kraus, and J. M. Rodenburg, *An Annealing Algorithm to Correct Positioning Errors in Ptychography.* Ultramicroscopy, 120, 64–72, 2012.

[20] Yan H. F., Rose V., Shu D., Lima E., Kang H. C., Conley R., Liu C. A., Jahedi N., Macrander A. T., Stephenson G. B., Holt M., Chu Y. S., Lu M. and Maser J., *Two Dimensional Hard X-ray Nanofocusing with Crossed Multilayer Laue Lenses.* Optics Express, Volume 19, Issue 16, 15069-15076, 2011.

[21] Yukio Takahashi, Akihiro Suzuki, Nobuyuki Zettsu, Yoshiki Kohmura, Yasunori Senba, Haruhiko Ohashi, Kazuto Yamauchi, Tetsuya Ishikawa, *Towards High-Resolution Ptychographic X-ray Diffraction Microscopy*. American Physical Society, Physical Review B 83, 214109, 2011.

[22] F. Hue, J. M. Rodednburg, A. M. Maiden, P. A. Midgley, *Extended Ptychography in the Transmission Electron Microscope: Possibilities and Limitations*. Ultramicroscopy, 111, 1117-1123, 2011.

[23] Chibum Lee, Srinivasa M. Salapaka, *Robust Broadband Nanopositioning: Fundamental Trade-offs, Analysis, and Design in a Two-Degree-of-Freedom Control Framework*. Nanotechnology, Volume 20, No 3, 2009.

[24] D. Vine, G. Williams, B. Abbey, M. Pfeifer, J. Clark, M. de Jonge, I. McNulty, A. Peele, and K. Nugent, *Ptychographic Fresnel Coherent Diffractive Imaging*. Physical Review A, Volume 80, 063823, 2009.

[25] Srinivasa M. Salapaka, Murti V. Salapaka, *Scanning Probe Microscopy*. IEEE Control Systems Magazine, 2008.

[26] Martin Dierolf, Oliver Bunk, Soren Knyde, Pierre Thibault, Ian Jonhson, Andreas Menzel, Konstantins Jefimovs, Christian David, Othmar Marti, Franz Pfieffer, *Ptychography and Lenseless X-ray Imaging*. Europhysicsnews, volume 39, number 1, 2008.

[27] D. Shu, J. Maser, M. Holt, R. Winarski, C. Preissner, A. Smolyanitsky, B. Lai, S. Vogt, and G. B. Stephenson, *Optomechanical Design of a Hard X-ray Nanoprobe Instrument with Nanometer Scale Active Vibration Control*. Synchrotron Radiation Instrumentation, Volume 879, pp. 1321-1324, 2007.

[28] Devasia S., Eleftheriou E., Moheimani S. O. R., *A Survey of Control Issues in Nanopositioning*. IEEE Transactions on Control Systems Technology, Volume 15, Issue 5, 2007.

[29] D. Shu, J. Maser, B. Lai, S. Vogt, M. Holt, C. Preissner, A. Smolyanitsky, B. Tieman, R. Winarski, and G. B. Stephenson, *Precision Mechanical Design for Hard X-ray Nanoprobe Instrument with Active Vibration Control in Nanometer Scale*. Proceedings of the 8th International Conference on X-ray Microscopy, IPAP Conference Series 7, 2006.

[30] Abu Sebastian, Srinivasa M. Salapaka, *Design Methodologies for Robust Nanopositioning*. IEEE Transactions on Control Systems Technology, Volume 13, No 6, 2005.

[31] D. Shu, J. Maser, M. Holt, B. Lai, S. Vogt, Y. Wang, C. Preissner, Y. Han, B. Tieman, R. Winarski, A. Smolyanitsky, and G. B. Stephenson, *Design and Test of a Differential Scanning Stage System for an X-ray Nanoprobe Instrument*. Optomechanics, Proceedings of SPIE, Volume 5877, 2005.

[32] Srinivasa M. Salapaka, Abu Sebastian, Jason P. Cleaveland, Murti V. Salapaka, *High Bandwidth Nano-Positioner: A Robust Control Approach*. Review of Scientific Instruments, Volume 73, No 9, 2002.

[33] Keith Glover, Duncan McFarlane, *A Loop Shaping Design Procedure Using $H_\infty-$ Synthesis*. IEEE Transactions on Automatic Control, Volume 34, No 8, 1992.

[34] Keith Glover, Duncan McFarlane, *Robust Stabilization of Normalized Coprime Factor Plant Descriptions with $H_\infty-$ Bounded Uncertainty*. IEEE Transactions on Automatic Control, Volume 37, No 6, 1989.

[35] Peter D. Welch, *The Use of Fast Fourier Transform for the Estimation of Power Spectra: a Method based on time Averaging Over short, Modified Periodograms*. IEEE Transactions on Audio and Electroacoustics, Volume AU-15, No 2, 1967.

[36] M. Green, D. Limebeer, *Linear Robust Control*. Dover Publications INC., Mineola, NY, 2012.

[37] Karl Astrom, Tore Hagglund, *Advanced PID Control*. Instrumentation, Systems, and Automation Society, 2006.

[38] Geir Dullerud, Fernando Paganini, *A Course in Robust Control Theory: A Convex Approach*. Springer, Text In Applied Mathematics 36, 2005.

[39] Sigurd Skogestad, Ian Postlethwaite, *Multivariable Feedback Control, Analysis and Design*, John Wiley & Sons, 2nd Edition, 2001.

[40] Sanjit K. Mitra, *Digital Signal Processing - A Computer Based Approach*, McGraw-Hill Series in Electrical and Computer Engineering, 2nd Edition, 2001.

[41] Ashok Ambardar, *Analog and Digital Signal Processing*. McGraw-Hill, 2nd Edition, 1999.

[42] M. Rivers, S. Sutton, K. Jones, *X-ray Fluorescence Microscopy*. X-ray Microscopy III, 1992.

[43] Torsten Soderstrom, Petre Stoica, *System Identification*, Prentice-Hall, 1989.

[44] Lennart Ljung, *System Identification: Theory for the User*, Prentice-Hall, 1987.